REPORT DOCUMENTATION PAGE

Form Approved
OMB NO. 0704-0188

1. AGENCY USE ONLY (Leave Blank)	2. REPORT DATE 9/21/2005	3. REPORT TYPE AND DATES COVERED Final Report 6/20/2002 – 6/19/2005

4. TITLE AND SUBTITLE	5. FUNDING NUMBERS
Single Spin Magnetic Resonance Force Microscopy	DAAD19-02-C-0055

6. AUTHOR(S)

Daniel Rugar

7. PERFORMING ORGANIZATION NAME(S) AND ADDRESS(ES) IBM Almaden Research Center 650 Harry Rd. San Jose, CA 95120	8. PERFORMING ORGANIZATION REPORT NUMBER

9. SPONSORING / MONITORING AGENCY NAME(S) AND ADDRESS(ES) U. S. Army Research Office P.O. Box 12211 Research Triangle Park, NC 27709-2211	10. SPONSORING / MONITORING AGENCY REPORT NUMBER 43705.6-MS-DRP

11. SUPPLEMENTARY NOTES
The views, opinions and/or findings contained in this report are those of the author(s) and should not be construed as an official Department of the Army position, policy or decision, unless so designated by other documentation.

12 a. DISTRIBUTION / AVAILABILITY STATEMENT Approved for public release; distribution unlimited.	12 b. DISTRIBUTION CODE

13. ABSTRACT (Maximum 200 words)

IBM and its subcontractors achieved the major goal of this contract: the detection of individual electron spins by magnetic resonance force microscopy (MRFM). To achieve this result, a number of key elements were developed, including a low temperature apparatus capable of detecting ultrasmall (attonewton) forces, specialized cantilever force sensors, methods for manipulating and detecting electron spins with random initial polarization, etc. In addition, both theoretical and experimental work has been performed to study MRFM detection of nuclear spins.

14. SUBJECT TERMS Magnetic resonance force microscopy, MRFM, spin detection			15. NUMBER OF PAGES 5 2
			16. PRICE CODE

17. SECURITY CLASSIFICATION OR REPORT **UNCLASSIFIED**	18. SECURITY CLASSIFICATION ON THIS PAGE **UNCLASSIFIED**	19. SECURITY CLASSIFICATION OF ABSTRACT **UNCLASSIFIED**	20. LIMITATION OF ABSTRACT **UL**

NSN 7540-01-280-5500

Standard Form 298 (Rev.2-89)
Prescribed by ANSI Std. 239-18
298-102

Single-spin magnetic resonance force microscopy

Final report

DARPA / ARO contract DAAD19-02-C-0055

Funded by the DARPA program on

Three-Dimensional Atomic-Scale Imaging

Daniel Rugar, Principal Investigator

IBM Research Division

Almaden Research Center

San Jose, CA 95120

e-mail: rugar@almaden.ibm.com

Subcontractors:

Prof. John Sidles, University of Washington

Prof. Alfred Hero, University of Michigan

Dr. James Tropp, GE Medical

31 August 2005

Table of Contents

List of Illustrations

Statement of Problem Studied

This contract investigated the detection of electron and nuclear spins using the technique of magnetic resonance force microscopy (MRFM). MRFM is of great interest because of its potential for atomic-resolution magnetic resonance imaging of molecules and materials. The primary goal of the contract was to extend the sensitivity of MRFM to detect individual electron spins. The goal was accomplished. An additional goal of the contract was the development of the technical infrastructure (cantilevers, magnetic tips, signal processing, theory, etc.) to support single electron spin detection and extension of MRFM to nuclear spin detection.

Scientific Accomplishments

1. Single-spin magnetic resonance force microscopy (IBM)

The primary goal of this contract was successfully achieved: the demonstration of single electron spin detection by magnetic resonance force microscopy (MRFM). In the key experiment, a low temperature MRFM apparatus detected the weak (attonewton) magnetic force from an individual electron spin associated with a dangling bond on a silicon atom buried beneath the surface of a silicon dioxide sample. This demonstration represents a watershed event in the development of MRFM since it conclusively demonstrated that MRFM is indeed capable of single spin detection, as previously proposed by John Sidles (University of Washington).

For a full description of the single spin experiment, please see the paper published in the journal Nature (paper #1 in the appendix).

The single spin demonstration was built upon a base of science and technology developed during the course of the contract. Some of the key elements were:

1. Ultrasensitive cantilevers that were engineered to minimize spin relaxation by reducing the thermal motion in high order modes. See Appendiix paper #2.
2. Methods to manipulate and detect small, randomly polarized spin ensembles. See Appendix papers #3 and #4.
3. Detailed understanding of spin relaxation in the context of MRFM. See Appendix paper #5.
4. Signal processing techniques optimized for detecting stochastic spin signals. See Appendix paper #6.
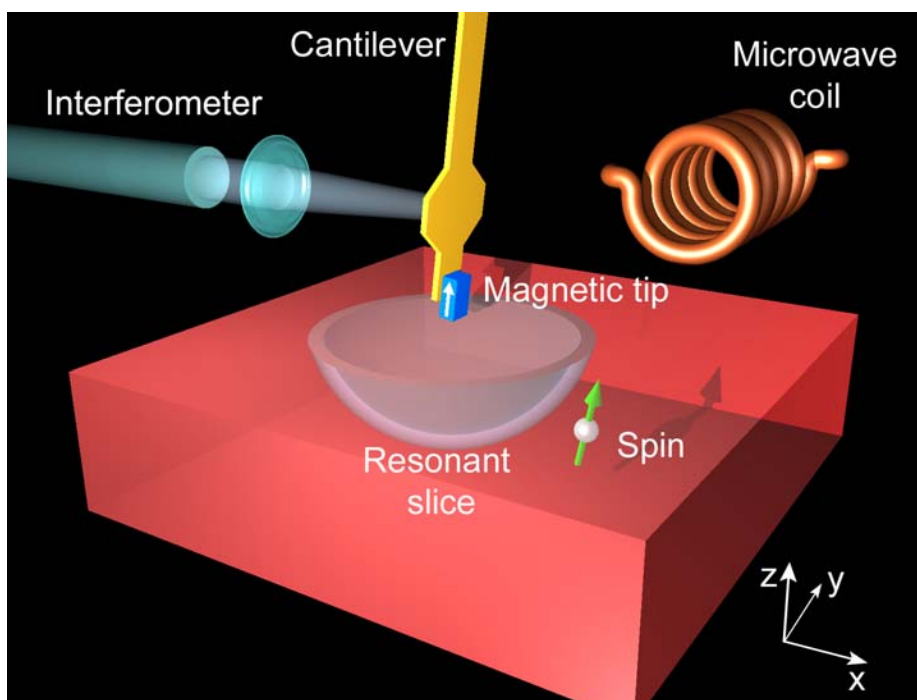
Figure 1.1 - Diagram of the MRFM single spin experiment. See paper #1 in Appendix for details.

The single spin accomplishment was met with considerable acclaim in both the mainstream and the scientific press. The American Institute of Physics called the single spin detection work the top physics story of 2004 (see the AIP web site: http://www.aip.org/pnu/2004/split/711-1.html). The single spin paper was ranked #7 of the most frequently downloaded articles on the Nature web site during July 2004 and was the only physical science article to make the top ten list.

News of the single spin result was widely disseminated. Articles appeared in the following media: New York Times, Dallas Morning News (full length feature), San Jose Mercury News, Kansas City Star, Daily Telegraph (London), Il Sole 24 Ore (Italy), Science, Physics Today, New Scientist, Discover magazine, Science News, Chemical and Engineering News, and Analytical Chemistry (feature article). This is only a partial list.

2. Detection of statistical polarization of nuclear spins in a protein (IBM)

In addition to our extensive work on electron spin detection, we also investigated nuclear spin detection. In particular, a key experiment was performed that demonstrates that the MRFM measurement protocols perfected for electron spin detection also work well with nuclear spins.

In an initial experiment, the statistical polarization of fluorine nuclear spins in calcium fluoride was measured using the interrupted OSCAR protocol, where OSCAR stands for oscillating cantilever-driven adiabatic reversal. In a second experiment, signals were obtained from a biomolecule: the protein collagen. This result is significant since a key long term goal of MRFM research is to image the structure of biomolecules.

This work has been published in Physical Review (see paper #7 in the appendix for technical details).

3. Image reconstruction algorithms for atomic resolution MRFM (U. Michigan)

A major motivation for magnetic resonance force microscopy (MRFM) is the possibility that three-dimensional atomic resolution of molecules can be obtained. To recover atomic positions from two- and three-dimensional MRFM data, an image reconstruction procedure must be used since the MRFM data is a convolution between the atomic positions and the paraboloidal point spread function given by the shape of the resonant slice.

The image reconstruction problem has been investigated during the course of this contract by the University of Michigan (UM) team, led by Prof. Al Hero. The UM team has developed a sophisticated algorithm that is effective at atomic-scale reconstructions even when the signal-to-noise ratio is low.

Some examples of the reconstructions are shown below in Figs. 3.1 - 3.3.

Proton Imaging of Molecules - Simulation
A simple example: Benzene - 12 atoms, 6 protons

2.5 Å

Proton positions

MRFM x-y scan simulation

r_{tip}= 3 nm
tip spacing ~ 3 nm
tip vibration ~ 0.5 Å
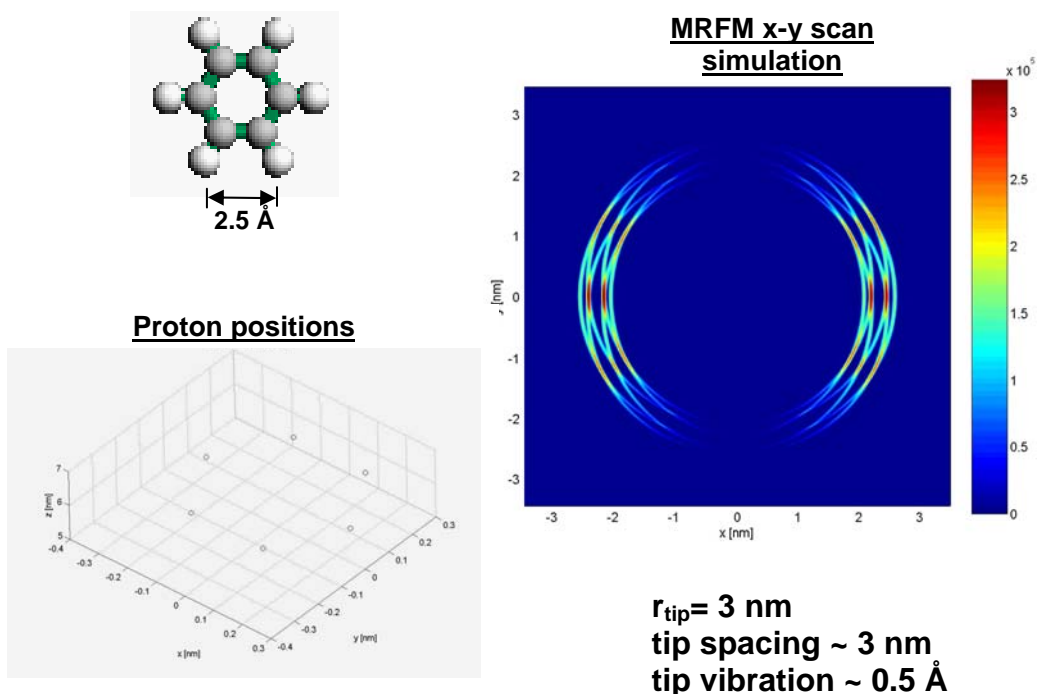
Figure 3.1 - Simulation of MRFM x-y scan of protons in a benzene molecule. The six rings originate from the six protons in the molecule.

Reconstruction of proton positions
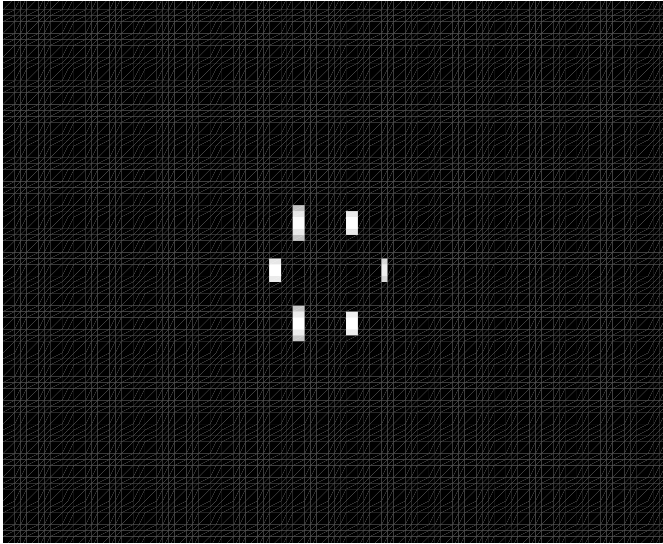
Advanced reconstruction algorithm based on expectation maximization with empirical Baysian denoising (EM-EB)

M. Ting, R. Raich and A. Hero, Univ. of Michigan

Figure 3.2 – Reconstruction of proton positions from simulated MRFM data for a benzene molecule.

Molecular Imaging – Simulation & Reconstruction
DNA example: 772 atoms, one C^{13} per nucleotide

M. Ting, R. Raich & A. Hero
Univ. of Michigan

Reconstruction of C^{13} positions
for SNR = 0 dB

Advanced reconstruction algorithm based on expectation maximization with empirical Baysian denoising (EM-EB)
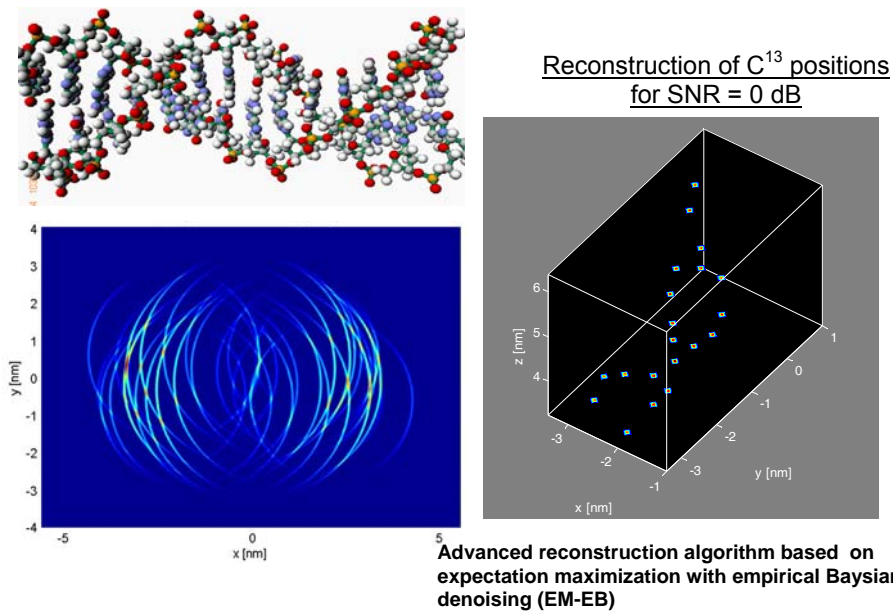
Figure 3.3 - Reconstruction of C-13 position in simulation of DNA molecule. The molecule is assumed to have been tagged with one C-13 atom per nucleotide.

4. MRFM Signal Detection Studies (University of Michigan)

The detection of the single electron spin signal was studied under the oscillating cantilever-driven adiabatic reversal (OSCAR) and interrupted OSCAR protocol. The main results are contained in paper #6 attached to the Appendix.

Initially, two continuous-time (CT) models were studied: firstly, the CT model obtained by using a classical dynamic treatment of the cantilever-single spin interaction; secondly, the CT model obtained assuming that the cyclic adiabatic inversion condition holds, and modeling the electron spin decoherence by a random telegraph process. Throughout the work on detection, an additive white Gaussian noise (AWGN) source was assumed. The first CT model resulted in two approaches, which will be briefly summarized here. Firstly, a parametric approach to the detection was explored [11]. A variant of the extended Kalman filter (EKF) was derived; together with a normal Kalman filter (KF), these two filters formed the spin detector. This detector was based on comparing the residual prediction errors of the Kalman non-linear state predictors generated by the classical non-linear dynamical equations of motion of the cantilever under spin and no spin conditions, respectively. This detector depended on knowing the exact values of all the parameters in the model. The second approach was a non-parametric "pattern recognition" method applied directly to the phase space generated by the dynamical equations. This detector relied on the fact that under spin coupling the cantilever position oscillates in a different part of phase space than under no spin coupling [12]. This phase space was estimated using correlation dimension and Taken's embedding technique to perform pattern recognition on the phase trajectories. None of the above techniques were tested on experimental data. The parametric approach was computationally expensive. Moreover, not all of the model parameters were exactly known in the experiment. The non-parametric approach seemed to work well for only high signal to noise ratios (SNRs). In contrast, the experiment was conducted in a relatively low SNR environment.

We next considered optimal detection for the random telegraph model. The first result obtained was the design of a hybrid Bayes/generalized likelihood ratio (GLR) detector for the standard CT random telegraph model [13]. A Gibbs sampler was used to approximate the integration and maximization dictated by the hybrid Bayes/GLR principle. The major difficulty with this implementation was high computational complexity. This led us to study an analogous random telegraph detection problem in discrete-time (DT), i.e., a two state Markov chain derived from discretization of the random telegraph signal in AWGN. A representation for the optimal Bayes detector was obtained and it was shown in [6,14] that this detector reduced to simple low complexity detectors under various relevant limiting conditions. In particular, we proved that the filtered energy (FE) detector is approximately optimal under the following four conditions: symmetric transition probabilities, low SNR, long observation time, and a small probability of transition between two consecutive time samples. When only the last three conditions hold, the hybrid FE detector, an extension of the FE detector, was shown to be approximately optimal. An alternative model that was proposed for the single electron spin-cantilever interaction is the DT random walk model. Simulations were presented in [6] showing that, for

certain random walks, the FE detector is approximately optimal. Theoretical analysis is presented in a paper under preparation.

Under the conditions of low SNR and assuming an AWGN noise source, it was shown that the optimal detector test statistic for a finite-state Markov signal is approximately the matched filter statistic with the minimum mean squared error (MMSE) predictor values used in place of the known signal values [6]. This result provides a general means of obtaining a suboptimal detector under low SNR for any finite-state Markov signal. When applied to the DT random telegraph model, one obtained an estimator-correlator detector. By using a suboptimal linear predictor instead of the MMSE predictor, the hybrid FE detector was recovered. The FE detector was successfully used in the detection of the single electron spin.

5. Digital signal processing and control (University of Washington)

Work at the UW focused on system control and end-to-end simulation in MRFM. This work was completed as planned, culminating in a PhD defense by UW graduate student Tom Kriewal titled "Heterodyne Digital Control and Frequency Estimation in Magnetic Resonance Force Microscopy". This thesis documents the main UW deliverables, which are two Pentek VME crates, each capable of simultaneous control of a Larmor cantilever, and emulation of that cantilever.

Both program tasks - - emulation and control - - are running in closed-loop mode. The performance of the system is in good accord with the original performance goals. This design allowed the investigators to test a novel method of heterodyne control for 25, 50, and 100 MHz signals. Heterodyne control is a method for reducing computational load and noise outside the passband and generating lock-in (synchronous detection) signals for online diagnostics, system identification, and adaptive control. Using one crate to generate the signal, and the other to control it, is the final deliverable of a control system that will work with cantilever signals at these frequencies.

6. Quantum measurement theory and simulation (Univ. of Washington)

Work performed at Univ. of Washington has established a reasonably satisfactory theoretical understanding of the IBM single-spin iOSCAR experiments. Both quantum measurement theory and IBM's experimental data agree that these experiments can be accurately described as random telegraph signals embedded in white noise (RTS+WN). This description is valid for all signal-to-noise ratios, and there are reasonable theoretical grounds to expect that this RTS+WN property will characterize future single-spin Larmor experiments.

Note also that RTS+WN processes have mathematical properties that are very desirable from an engineering and signal processing point of view. In particular,

numerical models of such process are highly efficient and straightforward to implement, and theoretical understanding of the informatic content of such processes is well advanced. The significance of this theoretical finding is that real-time quantum simulation has now been shown to be feasible for MRFM experiments.

The results show that using a semi-classical formalism to analyze iOSCAR experiments can be rigorously justified via orthodox POVM theory, and that Carlton Cave's amplifier noise bounds can be applied to MRFM experiments. We have also shown that spin-spin interactions are possible for Larmor experiments in a biological spin environment, provided the spin-lock field exceeds 20-30 Gauss or so, possibly less.

7. Quantum simulations of dipolar coupled spins in a field gradient (GE Medical)

Magnetic Resonance Force Microscopy (MRFM), as first conceived by Sidles, involves the coupling of a spin and a cantilever, both resonant at the Larmor frequency of the spin. In subsequent work, it has proven practical to resonate the cantilever at a frequency small compared to that of the spin, and to effect a coupling between the two by means of a modulation scheme, such as adiabatic passage, which causes the spin to cyclically reverse at some low frequency, matching that of the cantilever. Such a strategy is also convenient for calculations, since it obviates (to some approximation) the necessity of transforming the cantilever spatial coordinates to an interaction frame at the Larmor frequency.

That is, the oscillatory field of the cantilever, in any direction transverse to the quantization axis, will produce no transitions of the spin system, while that along the axis will produce at most a frequency or phase modulation. We have performed calculations of the spin dynamics – focusing particularly on dipole-mediated spin exchange in the presence of the static gradient from the cantilever tip-- for simple some models in this regime, and with an eye towards the following question: What is the likelihood of quenching spin diffusion with a realizable gradient?

The Two-Spin Problem

For a pair of dipolar-coupled protons in a static B field, consisting of a uniform component, plus a strong linear gradient, the Hamiltonian (in units of radian/sec) is:

$$H_t = \delta I_{z1} + k[I_{z1} I_{z2} - 1/4(I_{+1} I_{-2} + I_{+2} I_{-1})] ,$$

where δ is gradient strength times the internuclear distance, k is the dipolar constant, $\mu_0/(4\pi) \gamma^2 h \, r_{12}^{-3}(3\cos^2\theta - 1)$, with θ the angle between the inter-proton vector and the quantization axis, and we have chosen an interaction representation in which the static field vanishes at one of the protons.

The Multi-Spin Problem

The Hamiltonian for a homonuclear spin cluster is given by:

$$H = \Sigma \omega_i(r_i)I_{zi} + \Sigma k_{ij}[I_{zi}I_{zj} - 1/4(I_{+i}I_j + I_{+j}I_{-i})]$$

with $\omega_i(r_i)$ as the field of the cantilever tip at the ith spin, and k_{ij} equal to $\mu_0/(4\pi)\,\gamma^2 h\, r_{ij}^{-3}(3cos^2\theta_{ij} - 1)$. This admits of no simple solution in closed form, although it is straightforwardly simulated. We have employed the following models: four spins in a straight line, of arbitrary direction, with internuclear separation of 2.5 Å, and seven spins in a cubic lattice, comprising a central spin surrounded by all six of its nearest neighbors, also with internuclear separation of 2.5 Å. The cantilever tip is modelled as a sphere of 50 Å radius, with $\mu_0 M = 1.7$ T.

The computation consists of numerical diagonalization of the Hamiltonian, followed by evolution of the I_z operators, for given initial conditions, which are chosen, given the small number of spins, for illustrative purposes, rather than on physical grounds.

Note that we follow the usual practice for high field NMR in solids, and use only the z component of the dipole field produced by the magnetic tip; this is easily justifiable for gradient fields (in frequency units) ≤ 1% of the Larmor frequency.

The results of the calculations are given in the figures below. The main conclusion of the work is that the strong field gradients needed for atomic resolution imaging will suppress the flip-flop interactions between dipolar-coupled spin, except along the iso-field lines of the magnetic tip. In general, the suppression of dipolar coupling effects is believed to be beneficial for atomic resolution imaging. Further work will be required to gauge the impact of the iso-field regions where there is inefficient suppression. This may not be a serious issue since, during imaging, the tip is mechanically scanned with respect to the sample, which implies that dipolar non-suppression is only a temporary, localized condition.
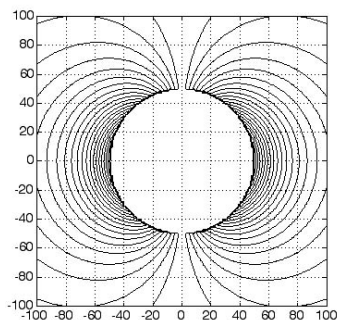
Exemplary calculation of flux lines for the magnetic tip; axes in Å
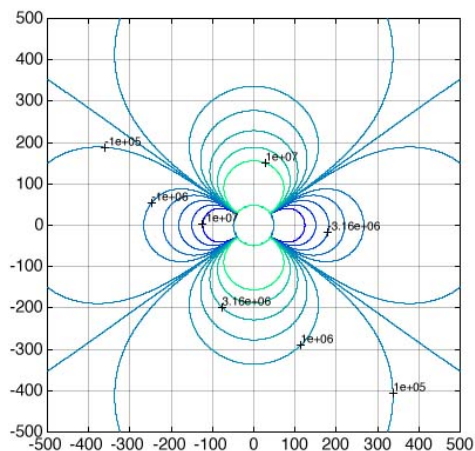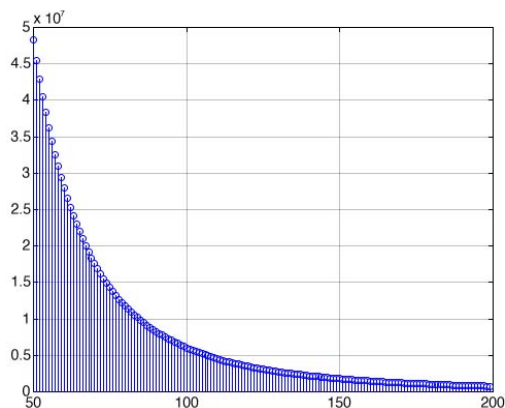
Iso-contours of z-directed dipole field of the magnetic tip, in units of Hz (proton larmor frequency/2π). Note the characteristic "d orbital" shape, and the nodal lines along the magic angle (direction cosines [1 1 1]). The vertical and horizontal axes are z and y; axes in Å

Dipole z-field strength along z axis, in Hz (as above) axes in Å

Figure 7.1: Characteristics of the model magnetic tip.

Figure 7.2: Dynamics of linear spin arrays parallel and perpendicular to maximum gradient direction

Position of four- spin array on the dipole field iso-contour map.
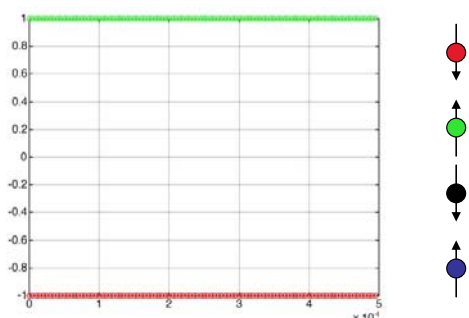
Time course of spin evolution (over 0.5 ms) for four spins aligned in direction of maximum gradient (~35 G/Å). The initial condition is color-coded in the transpierced circles at right; note total suppression of spin exchange/diffusion.

Time course of spin evolution (over 0.5 ms) for four spins aligned approximately on tip-field iso-contour (minimum gradient). The initial condition is per color-coded circles below; spin exchange/diffusion proceeds virtually unhindered.

Figure 7.3: Dynamics of spin array parallel and maximum gradient, at varying distances from tip.

450 Å from tip (significant coupling)

350 Å from tip (partially decoupled)

250 Å from tip (fully decoupled)

300 Å from tip; only axial members are decoupled.

420 Å from tip, no decoupling.

Time course ΣI_{zi} shows conservation of net moment

300 Å from tip, no decoupling.

Figure 7.4: Dynamics of cubic spin array at various locations.

Publications

Papers published with full or partial support of this contract

Peer reviewed journal articles

1. "Single spin detection by magnetic resonance force microscopy", D. Rugar, R. Budakian, H. J. Mamin and B. W. Chui, Nature 430, 329-332 (2004).

2. "Detection and manipulation of statistical polarization in small spin ensembles", H. J. Mamin, R. Budakian, B. Chui, D. Rugar, Phys. Rev. Lett. **91**, 207604 (2003)

3. "Creating order from random fluctuations in small spin ensembles", R. Budakian, H. J. Mamin, B. Chui and D. Rugar, Science **307**, 408-411 (2005).

4. "Suppression of spin diffusion near a micron-size ferromagnet", R. Budakian, H. J. Mamin and D. Rugar, Phys. Rev. Lett. **92**, 037205 (2004).

5. "Near optimal signal detection for finite state markov signals with application to magnetic resonance force microscopy", M. Ting, A. O. Hero, D. Rugar, C.-Y. Yip, J. A. Fessler, IEEE Trans. Signal Processing (in press).

6. "The Classical and Quantum Theory of Thermal Magnetic Noise, with Applications in Spintronics and Quantum Microscopy", J. A. Sidles, J. L. Garbini, W. M. Dougherty and S. H. Chao, Proceedings of the IEEE, **91**(5):799-816, 2003.

7. "Nanometer-scale Magnetic Resonance Imaging", S. H. Chao, W. M. Dougherty, J. L. Garbini and J. A. Sidles, Rev. Sci. Instrum. **75**, 2004.

8. "Superconducting resonator for millikelvin magnetic resonance force microscopy", H. J. Mamin, R. Budakian and D. Rugar, Rev. Sci. Instrum. **74**, 2749 (2003)

9. "Manipulating and detecting statistical polarization of nuclear spins by magnetic resonance force microscopy", H. J. Mamin, R. Budakian, B. W. Chui and D. Rugar, Phys. Rev. B **72,** 024413 (2005)

Papers published in conference proceedings

1. "Mass-loaded cantilever with suppressed higher-order modes for magnetic resonance force microscopy", B. W. Chui, Y. Hishinuma, R. Budakian, H. J. Mamin, T. W. Kenny and D. Rugar, Technical Digest of the 12th International Conference on Solid State Sensors and Actuators (Transducers'03), Boston, MA, June 8-12, 2003, pp. 1120-3.

2. "Feeling the noise in nanoscale systems: studies based on ultrasensitive force detection", D. Rugar, R. Budakian, B. W. Chui and H. J. Mamin, in Proceedings of SPIE Vol. 5115 Noise and Information in Nanoelectronics, Sensors and Standards, edited by Laszio B. Kish, Frederick Green, Giuseppe Iannaccone, John R. Vig (SPIE, Bellingham, WA, 2003), pp. xi - xix.

3. "Nanoribbed torsional oscillators optimized for high frequency force sensing", B. W. Chui, C. T. Rettner, H. J. Mamin, R. Budakian and D. Rugar, Proceedings of Hilton Head Conference on Microelectromechanical Systems (2004).

4. "Detection of an electron spin in a MRFM cantilever experiment", M. Ting and A. O. Hero, Proc. of the 2003 IEEE Workshop on Stat. Sig. Proc, 2003, pp. 633-636.

5. "Frequency estimation derived from a dynamical system analysis", C. Hory, M. Ting, A. O. Hero, Proc. of the 2003 IEEE Workshop on Stat. Sig. Proc, 2003, pp. 198-201.

6. "Baseband detection of bistatic electron spin signals in magnetic resonance force microscopy", C.-Y. Yip, A. O. Hero, D. Rugar, J. A. Fessler, Conf. record of the 37th Asilomar Conference on Signals, Systems, and Computers, 2003, pp. 1309-1313.

7. "Two state Markov modeling and detection of single electron spin signals", A. O. Hero, M. Ting, J. A. Fessler, Proc. of the XII European Signal Processing Conference, 2004.

Participating Scientific Personnel

IBM

Daniel Rugar, Ph.D.
H. Jonathan Mamin, Ph.D.
Benjamin Chui, Ph.D. – Visiting Scientist
Raffi Budakian, Ph.D. – Post-doc
Dean Pearson
Bruce Melior

University of Washington

John Sidles, Ph.D.
Joseph Garbini, Ph.D.
Jonathan Jacky, Ph.D.
Thomas E. Kriewall – earned Ph.D. while on project

University of Michigan

Al Hero, Ph.D.
Jeff Fessler, Ph.D.
Cyril Hory, Ph.D. - Post-doc
Pei-Jung Chung, Ph.D. – Post-doc
Michael Ting – earned Masters degree, Ph.D. expected December 2005
Chun-yu Yip – earned Masters degree

GE Medical

James Tropp, Ph.D.

Appendix

In this appendix we include reprints of some of our most significant published papers. These represent key results of the contract and contain technical details of the contract results.

1. "Single spin detection by magnetic resonance force microscopy", D. Rugar, R. Budakian, H. J. Mamin and B. W. Chui, Nature 430, 329-332 (2004).

2. "Mass-loaded cantilever with suppressed higher-order modes for magnetic resonance force microscopy", B. W. Chui, Y. Hishinuma, R. Budakian, H. J. Mamin, T. W. Kenny and D. Rugar, Technical Digest of the 12th International Conference on Solid State Sensors and Actuators (Transducers'03), Boston, MA, June 8-12, 2003, pp. 1120-3.

3. "Detection and manipulation of statistical polarization in small spin ensembles", H. J. Mamin, R. Budakian, B. Chui, D. Rugar, Phys. Rev. Lett. **91**, 207604 (2003)

4. "Creating order from random fluctuations in small spin ensembles", R. Budakian, H. J. Mamin, B. Chui and D. Rugar, Science **307**, 408-411 (2005).

5. "Suppression of spin diffusion near a micron-size ferromagnet", R. Budakian, H. J. Mamin and D. Rugar, Phys. Rev. Lett. **92**, 037205 (2004).

6. "Near optimal signal detection for finite state markov signals with application to magnetic resonance force microscopy", M. Ting, A. O. Hero, D. Rugar, C.-Y. Yip, J. A. Fessler, IEEE Trans. Signal Processing (in press).

7. "Manipulating and detecting statistical polarization of nuclear spins by magnetic resonance force microscopy", H. J. Mamin, R. Budakian, B. W. Chui and D. Rugar, Phys. Rev. B **72,** 024413 (2005)

letters to nature

9. Trujillo Bueno, J., Collados, M., Paletou, F. & Molodij, G. in *Advanced Solar Polarimetry: Theory, Observations and Instrumentation* (ed. Sigwarth, M.) 141–149 (ASP Conf. Ser. Vol. 236, Astronomical Society of the Pacific, San Francisco, 2001).
10. Bommier, V. & Molodij, G. Some THEMIS-MTR observations of the second solar spectrum (2000 campaign). *Astron. Astrophys.* **381**, 241–252 (2002).
11. Gandorfer, A. *The Second Solar Spectrum* Vol. 1, *4625 Å to 6995 Å* (vdf, Zurich, 2000).
12. Faurobert-Scholl, M., Feautrier, N., Machefert, F., Petrovay, K. & Spielfiedel, A. Turbulent magnetic fields in the solar photosphere: diagnostics and interpretation. *Astron. Astrophys.* **298**, 289–302 (1995).
13. Faurobert, M., Arnaud, J., Vigneau, J. & Frisch, H. Investigation of weak solar magnetic fields. New observational results for the Sr I 460.7 nm linear polarization and radiative transfer modeling. *Astron. Astrophys.* **378**, 627–634 (2001).
14. Hanle, W. Über magnetische Beeinflussung der Polarisation der Resonanzfluoreszenz. *Z. Phys.* **30**, 93–105 (1924).
15. Trujillo Bueno, J. in *Advanced Solar Polarimetry: Theory, Observations and Instrumentation* (ed. Sigwarth, M.) 161–195 (ASP Conf. Ser. Vol. 236, Astronomical Society of the Pacific, San Francisco, 2001).
16. Stenflo, J. O. The Hanle effect and the diagnostics of turbulent magnetic fields in the solar atmosphere. *Sol. Phys* **80**, 209–226 (1982).
17. Shchukina, N. & Trujillo Bueno, J. in *Solar Polarization 3* (eds Trujillo Bueno, J. & Sánchez Almeida, J.) 336–343 (ASP Conf. Ser. Vol. 307, Astronomical Society of the Pacific, San Francisco, 2003).
18. Asplund, M., Nordlund, Å., Trampedach, R., Allende Prieto, C. & Stein, R. F. Line formation in solar granulation. I. Fe line shapes, shifts and asymmetries. *Astron. Astrophys.* **359**, 729–742 (2000).
19. Cattaneo, F. On the origin of magnetic fields in the quiet photosphere. *Astrophys. J.* **515**, L39–L42 (1999).
20. Stein, R. F. & Nordlund, Å. in *Modelling of Stellar Atmospheres* (eds Piskunov, N. E., Weiss, W. W. & Gray, D. F.), 169–180 (ASP Conf. Ser. Vol. IAU 210, Astronomical Society of the Pacific, San Francisco, 2003).
21. Socas-Navarro, H. & Sánchez Almeida, J. Magnetic fields in the quiet Sun: observational discrepancies and unresolved structure. *Astrophys. J.* **593**, 581–586 (2003).
22. Sánchez Almeida, J., Emonet, T. & Cattaneo, F. Polarization of photospheric lines from turbulent dynamo simulations. *Astrophys J.* **585**, 536–552 (2003).
23. Trujillo Bueno, J., Casini, R., Landolfi, M. & Landi Degl'Innocenti, E. The physical origin of the scattering polarization of the Na I D lines in the presence of weak magnetic fields. *Astrophys J.* **566**, L53–L57 (2002).
24. Landi Degl'Innocenti, E. Evidence against turbulent and canopy-like magnetic fields in the solar chromosphere. *Nature* **392**, 256–258 (1998).
25. Stenflo, J. O. in *Solar Polarization 3* (eds Trujillo Bueno, J. & Sánchez Almeida, J.) 385–398 (ASP Conf. Ser. Vol. 307, Astronomical Society of the Pacific, San Francisco, 2003).
26. Anderson, L. S. & Athay, R. G. Model solar chromosphere with prescribed heating. *Astrophys. J.* **346**, 1010–1018 (1989).
27. Priest, E. & Forbes, T. *Magnetic Reconnection: MHD Theory and Applications* (Cambridge Univ. Press, New York, 2000).
28. Landi Degl'Innocenti, E. Polarization in spectral lines: I. A unifying theoretical approach. *Sol. Phys.* **85**, 3–31 (1983).
29. Trujillo Bueno, J. in *Stellar Atmosphere Modeling* (eds Hubeny, I., Mihalas, D. & Werner, K.) 551–582 (Asp Conf. Ser. Vol. 288, Astronomical Society of the Pacific, San Francisco, 2003).
30. Trujillo Bueno, J. in *Solar Polarization 3* (eds Trujillo Bueno, J. & Sánchez Almeida, J.) 407–424 (ASP Conf. Ser. Vol. 307, Astronomical Society of the Pacific, San Francisco, 2003).

Competing interests statement The authors declare that they have no competing financial interests.

Correspondence and requests for materials should be addressed to J.T.B. (jtb@iac.es).

....

Single spin detection by magnetic resonance force microscopy

D. Rugar, R. Budakian, H. J. Mamin & B. W. Chui

IBM Research Division, Almaden Research Center, 650 Harry Rd, San Jose, California 95120, USA

Magnetic resonance imaging (MRI) is well known as a powerful technique for visualizing subsurface structures with three-dimensional spatial resolution. Pushing the resolution below 1 μm remains a major challenge, however, owing to the sensitivity limitations of conventional inductive detection techniques. Currently, the smallest volume elements in an image must contain at least 10^{12} nuclear spins for MRI-based microscopy[1], or 10^{7} electron spins for electron spin resonance microscopy[2]. **Magnetic resonance force microscopy (MRFM) was proposed as a means to improve detection sensitivity to the single-spin level, and thus enable three-dimensional imaging of macromolecules (for example, proteins) with atomic resolution[3,4]. MRFM has also been proposed as a qubit readout device for spin-based quantum computers[5,6]. Here we report the detection of an individual electron spin by MRFM. A spatial resolution of 25 nm in one dimension was obtained for an unpaired spin in silicon dioxide. The measured signal is consistent with a model in which the spin is aligned parallel or anti-parallel to the effective field, with a rotating-frame relaxation time of 760 ms. The long relaxation time suggests that the state of an individual spin can be monitored for extended periods of time, even while subjected to a complex set of manipulations that are part of the MRFM measurement protocol.**

MRFM is based on the detection of the magnetic force between a ferromagnetic tip and spins in a sample. The fundamental challenge in achieving single-spin sensitivity is that the force from a single spin is exceedingly small. Even with tip field gradients in the gauss per nanometre range, the force from an electron spin is only a few attonewtons. This force is roughly a million times smaller than is typically detected by atomic force microscopy (AFM). Recently, major strides towards single-spin detection have been made with the development of ultrasensitive cantilever-based force sensors[7,8], better understanding of relevant spin relaxation processes[9–12] and the successful detection of statistical polarization in small spin ensembles[13].

The basic elements of our MRFM apparatus are shown in Fig. 1 and have been described in detail in ref. 13. Briefly, a custom-fabricated mass-loaded silicon cantilever[8,13] with an attached 150-nm-wide SmCo magnetic tip is used to sense the force from the electron spin. The sample consists of vitreous silica (Suprasil W2) that was irradiated with a 2-Gy dose of Co^{60} gamma rays. The gamma irradiation produces a low concentration of silicon dangling bonds containing unpaired electron spins known as E′ centres[14].
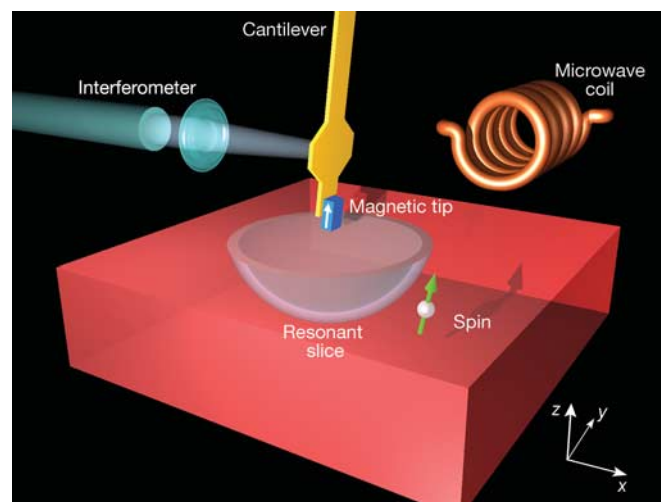
Figure 1 Configuration of the single-spin MRFM experiment. The magnetic tip at the end of an ultrasensitive silicon cantilever is positioned approximately 125 nm above a polished SiO_2 sample containing a low density of unpaired electron spins. The resonant slice represents those points in the sample where the field from the magnetic tip (plus an external field) matches the condition for magnetic resonance. As the cantilever vibrates, the resonant slice swings back and forth through the sample causing cyclic adiabatic inversion of the spin. The cyclic spin inversion causes a slight shift of the cantilever frequency owing to the magnetic force exerted by the spin on the tip. Spins as deep as 100 nm below the sample surface can be probed.

©2004 **Nature Publishing Group**

letters to nature

Estimated spin concentration was between 10^{13} and $10^{14}\,\text{cm}^{-3}$. The experiments were performed at 1.6 K in a small vacuum chamber that fits within the bore of a superconducting magnet. The low operating temperature minimizes the force noise and reduces the relaxation rate of the spins.

A microwave magnetic field ($B_1 \approx 0.3\,\text{mT}$), in combination with the inhomogeneous field from the magnetic tip, sets up a 'resonant slice' within the sample. The resonant slice corresponds to those points in the sample where the tip field $\mathbf{B}_{\text{tip}}(x, y, z)$, plus a static external field $\hat{\mathbf{z}}\,B_{\text{ext}}$, satisfies the condition for electron spin resonance: $B_0(x,y,z) \equiv |\mathbf{B}_{\text{tip}}(x,y,z) + \hat{\mathbf{z}}\,B_{\text{ext}}| = \omega_{\text{rf}}/\gamma$. Here, ω_{rf} is the frequency of the microwave field and γ is the gyromagnetic ratio ($\gamma/2\pi = 2.8 \times 10^{10}\,\text{Hz}\,\text{T}^{-1}$). In the present experiment, where $\omega_{\text{rf}}/2\pi = 2.96\,\text{GHz}$, the resonant slice corresponds to $B_0(x, y, z) = 106\,\text{mT}$. For typical conditions (for example, $B_{\text{ext}} = 30\,\text{mT}$), the slice is a bowl-shaped surface that extends roughly 250 nm below the tip. Note that with the perpendicular cantilever orientation shown in Fig. 1, the cantilever is responsive only to the x component of force. Thus the spin must be located either slightly in front of or slightly behind the cantilever in the x direction to produce a substantial response.

To generate a force signal that can be distinguished from the much larger background force fluctuations, we use the recently developed spin manipulation protocol known as 'interrupted OSCAR' or iOSCAR, where OSCAR stands for oscillating cantilever-driven adiabatic reversals[13]. In the iOSCAR protocol, the cantilever is part of a gain-controlled positive-feedback loop that drives the cantilever to oscillate at a set amplitude (for example, 16 nm) at the fundamental frequency of the cantilever ($f_c = 5.5\,\text{kHz}$). Because the cantilever is the frequency-determining element in the feedback loop, the vibration frequency will automatically vary in response to tip–sample interactions[15].

The vibration of the cantilever tip causes the resonant slice to sweep back and forth rapidly through the sample. If the slice happens to sweep through the location of a spin, the spin will be cyclically inverted in synchrony with the cantilever motion owing to the phenomenon of adiabatic rapid passage[13,16]. This synchronous inversion of the spin creates an alternating magnetic force on the cantilever that mimics a change in cantilever stiffness. The resulting shift in cantilever frequency is given by[13,17]:

$$\delta f_c = \pm \frac{2 f_c G \mu_B}{\pi k x_{\text{peak}}}, \qquad (1)$$

where k is the cantilever spring constant, x_{peak} is the peak vibration amplitude of the cantilever, $G \equiv \partial B_0/\partial x$ is the lateral field gradient, and μ_B is the magnetic moment of the electron ($9.3 \times 10^{-24}\,\text{J}\,\text{T}^{-1}$). The sign of the frequency shift depends on the relative phase of the spin inversions with respect to the cantilever motion. Using the terminology of magnetic resonance, the two polarities correspond to adiabatic rapid passages with the spin either aligned or anti-aligned with respect to the effective field in the rotating frame[13,16]. This parallel or anti-parallel alignment is expected to be enforced by the quantum-mechanical measurement process, resulting in the collapse of the initial spin wavefunction onto an eigenstate of the effective field[18,19]. For the parameters of the current experiment ($G = 2 \times 10^5\,\text{T}\,\text{m}^{-1}$; $k = 0.11\,\text{mN}\,\text{m}^{-1}$; $x_{\text{peak}} = 16\,\text{nm}$), the expected frequency shift is $|\delta f_c| = 3.7 \pm 1.3\,\text{mHz}$. The estimated uncertainty in $|\delta f_c|$ reflects 20% uncertainties in the calibration of G, k and x_{peak}.

In the 'interrupted' version of the protocol (iOSCAR), the microwave field B_1 is turned off for one-half of a cantilever cycle every 64 cycles ($f_{\text{int}} = f_c/64 \approx 86\,\text{Hz}$). As shown in Fig. 2, each time B_1 is interrupted, the relative phase of the spin and cantilever is reversed, causing the frequency shift to reverse polarity. (See Supplementary Information for an animation.) The net result of the interruptions is that the frequency shift will alternate between positive and negative values in a square-wave-like fashion with a frequency given by $f_{\text{sig}} = f_{\text{int}}/2$, or approximately 43 Hz. The resulting frequency shift signal can be written as the Fourier series:

$$\Delta f(t) = \frac{4}{\pi}|\delta f_c| A(t)\sin(2\pi f_{\text{sig}} t) + \text{higher harmonics} \qquad (2)$$

where the $4/\pi$ comes from the first harmonic Fourier amplitude of a square wave.

We have included the function $A(t)$ to take into account the fact that the signal will not be perfectly periodic owing to extra random spin flips induced by the environment. Assuming that this 'quantum jump' model is correct, $A(t)$ is a random telegraph function that takes on values of ± 1. For Poisson distributed jumps, $A(t)$ is expected to have a lorentzian power spectrum[20] and the statistical properties $\langle A(t) \rangle = 0$ and $\langle [A(t)]^2 \rangle = 1$, where $\langle \cdots \rangle$ denotes time average. We detect the first harmonic of the signal only, so we will
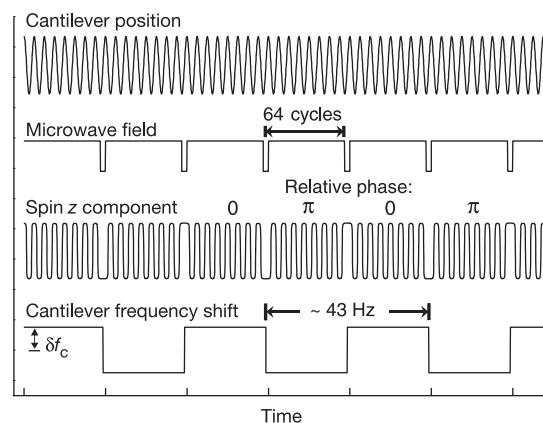

Figure 2 Timing diagram for the iOSCAR spin manipulation protocol. The z component of spin follows the motion of the cantilever except during the interruption of the microwave field. The interruptions last for one-half of a cantilever period and are precisely timed to start and stop at vibration extrema. The interruptions, which occur every 64 cantilever cycles, reverse the phase of the spin with respect to the cantilever, resulting in a square-wave oscillation of the cantilever frequency.

Figure 3 Plots showing the spin signal as the sample was scanned laterally in the x direction for two values of external field: **a**, $B_{\text{ext}} = 34\,\text{mT}$, and **b**, $B_{\text{ext}} = 30\,\text{mT}$. The smooth curves are gaussian fits that serve as guides to the eye. The 19-nm shift in peak position reflects the movement of the resonant slice induced by the 4-mT change in external field. The difference in absolute peak height is primarily due to different lock-in amplifier detection bandwidths: 0.18 Hz and 0.59 Hz for **a** and **b**, respectively. Power spectra for the points marked 1 and 2 are shown in Fig. 4.

refer to the quantity $\Delta f_1(t) \equiv (4/\pi)|\delta f_c|A(t)$ as the spin signal amplitude.

Because the frequency modulation due to the spin is only a few millihertz and the frequency noise of the cantilever due to thermal motion and tip–sample interactions is relatively large (~ 25 mHz in a 1-Hz bandwidth), we must use signal averaging to detect the spin signal. However, because $\langle \Delta f_1(t) \rangle = 0$, we average the square of the signal (the signal 'energy'), rather than the signal amplitude. Specifically, the frequency modulation of the cantilever is detected using an analogue frequency discriminator[15] followed by a digital lock-in amplifier that has been implemented in software. The lock-in amplifier uses a bank of low-pass filters and, as a function of detection bandwidth, determines the energy (that is, variance) of the in-phase and quadrature components of the frequency-shift signal $\Delta f(t)$. The spin signal and the measurement noise are uncorrelated, so we can write the in-phase variance as $\sigma_I^2 = \sigma_{spin}^2 + \sigma_{noise}^2$, where σ_{spin}^2 is the variance due to the spin signal and σ_{noise}^2 represents the measurement noise. This in-phase variance is then compared to the quadrature variance σ_Q^2, which contains only the measurement noise. The signal energy from the spin can then be estimated as $\sigma_{spin}^2 = \sigma_I^2 - \sigma_Q^2$. This energy detection scheme

is believed to have performance close to the theoretically optimal detector[21].

Figure 3a shows a lateral scan where we plot σ_{spin}^2 as a function of sample position. The scan shows a prominent peak that we believe is due to a single spin. The peak width is 25 nm, or roughly 1.6 times the cantilever oscillation amplitude. Note that the baseline of the data on either side of the peak is essentially zero (within the uncertainty of the measurement), thus demonstrating that the iOSCAR protocol generates no systematic feedthrough artefacts. Because the signal-to-noise ratio was so low ($\sigma_{spin}^2/\sigma_I^2 \sim 0.06$), considerable averaging was required. In Fig. 3a, the averaging time was 13 h per point, yielding a signal peak that is five standard deviations above the baseline noise.

To confirm that the observed signal is truly due to magnetic resonance, a number of basic tests were performed. As expected for an iOSCAR magnetic resonance signal, the signal disappeared if the microwaves were absent or turned on continuously. The timing of the microwave interruptions was also varied. The signal disappeared, as expected, when the starting time of the interruption was shifted from the vibration peak to the zero-crossing of the vibration (that is, shifted by one-quarter of a cantilever cycle) and when the interruption duration was a full cantilever cycle instead of one-half cycle.

One key test for magnetic resonance is to observe the field dependence of the spin signal. If the external field is reduced, the resonant slice will shrink in radius, thus shifting the scan position of the signal peak. When B_{ext} was reduced from 34 to 30 mT, the expected peak shift was indeed observed and found to be $\Delta x = 19$ nm, as can be seen by comparing the scans in Figs 3a and b. The ratio $\Delta B_{ext}/\Delta x$ suggests that the field gradient G is approximately 2×10^5 T m^{-1} (2 G nm^{-1}).

The conclusion that the signal is due to only one spin is based primarily on the spatial isolation of the spin signal. By design, the spin density of the sample was very low, in the range of 10^{13} to 10^{14} cm^{-3}, giving a mean spacing between spins in the range of 200 to 500 nm. The sparseness of spins implies that, for most sample locations, there is no spin interacting with the resonant slice. This is why the data in Fig. 3 has a zero baseline. To locate a spin signal, the sample was scanned through many independent locations, of the order of 30, before a strong signal from a well-positioned spin was found.

By measuring σ_{spin}^2 as a function of detection bandwidth, the power spectral density of the spin signal amplitude $\Delta f_1(t)$ can be determined (Fig. 4a). Consistent with a random telegraph model of $\Delta f_1(t)$, the spectrum is well fitted by the lorentzian function $S(f) = 4\tau_m\langle[\Delta f_1(t)]^2\rangle/[1 + 4\pi^2\tau_m^2 f^2]$. The spectral width at half-maximum is 0.21 Hz, corresponding to an impressively long τ_m correlation time of 760 ms. This is essentially the rotating frame relaxation time, but also includes possible effects of the iOSCAR spin manipulation. The long correlation time implies that the cantilever-driven spin inversions are coherent for thousands of cycles. The false-colour image in Fig. 4b shows that the spin signal is highly localized both spatially and spectrally.

The total magnitude of the spin signal, obtained by integrating the spectrum in Fig. 4a, was found to be $\langle[\Delta f_1(t)]^2\rangle = 28$ mHz^2. Using this experimental value and the relationship $\langle[\Delta f_1(t)]^2\rangle = (4/\pi)^2|\delta f_c|^2\langle[A(t)]^2\rangle$, we solve for $|\delta f_c|$ using the assumption that $\langle[A(t)]^2\rangle = 1$. We find $|\delta f_c| = 4.2$ mHz, in excellent agreement with the value of 3.7 mHz expected from equation (1).

In conclusion, we have presented evidence that MRFM is now capable of detecting individual electron spins. Although several other single-spin detection methods have been previously demonstrated[22–28], MRFM has some attributes that set it apart. Perhaps the most important of these is the ability to image spins below the surface with nanometre spatial resolution. Spins as deep as 100 nm should be accessible under present operating conditions. Although extensive signal averaging is currently required, even a modest
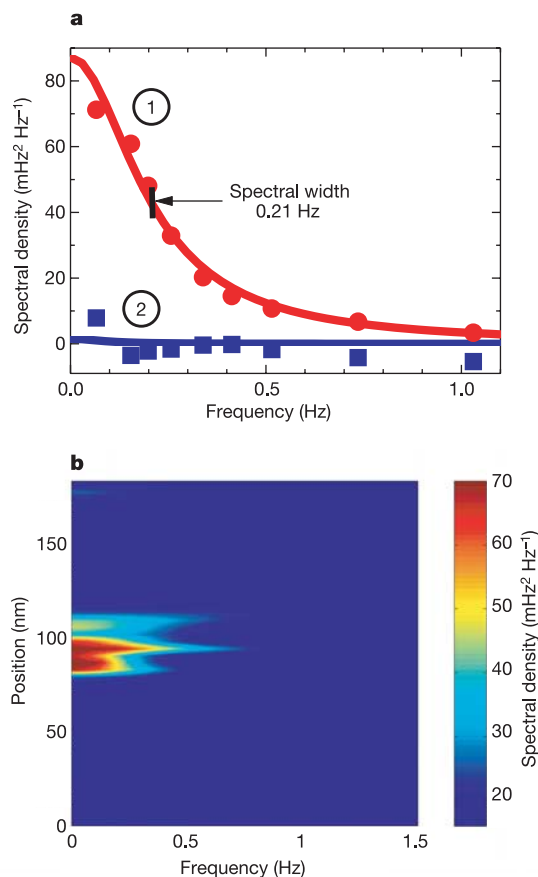
Figure 4 By measuring the spin signal energy as a function of detection bandwidth, the power spectral density of the spin signal amplitude $\Delta f_1(t)$ can be determined. **a**, Spectral density for the two positions indicated in Fig. 3. The strong spin signal at position 1 has a narrow spectral width (0.21 Hz), reflecting the long (760 ms) correlation time obtained using iOSCAR spin manipulation. The data are well fitted by a lorentzian function (solid curve). At position 2, approximately 70 nm away from the position of the spin signal, the spectral density is negligible. **b**, False-colour plot showing power spectral density as a function of position. The spin signal is localized both spatially and spectrally. The data were interpolated between discrete measurement positions to create a smooth image. The apparent fine structure in the signal region is probably an artefact of the limited signal-to-noise ratio of the original data.

letters to nature

increase in field gradient (for example, five times larger) will dramatically speed up the acquisition time and thereby enable two- and three-dimensional imaging applications. (Because we average signal energy, rather than amplitude, the averaging time will decrease as the inverse fourth power of the gradient in the limit of low signal-to-noise ratio.) If the measurement time can be reduced below τ_m, real-time readout of the spin quantum state will become possible, enabling a wide variety of quantum measurement experiments. For molecular imaging applications, extension to single nuclear spin detection is necessary, but this will require a roughly 1,000-fold improvement in magnetic moment sensitivity. Considering that the present experiment represents a sensitivity improvement of 10^7 times over the original MRFM experiment[29], the remaining required improvement does not seem out of the question, especially since there is still considerable leeway for increasing the field gradient and lowering the operating temperature. □

1. Ciobanu, L., Seeber, D. A. & Pennington, C. H. 3D MR microscopy with resolution 3.7 µm by 3.3 µm by 3.3 µm. *J. Magn. Reson.* **158**, 178–182 (2002).
2. Blank, A., Dunnam, C. R., Borbat, P. P. & Freed, J. H. High resolution electron spin resonance microscopy. *J. Magn. Reson.* **165**, 116–127 (2003).
3. Sidles, J. A. Folded Stern-Gerlach experiment as a means for detecting nuclear magnetic resonance in individual nuclei. *Phys. Rev. Lett.* **68**, 1124–1127 (1992).
4. Sidles, J. A. *et al.* Magnetic resonance force microscopy. *Rev. Mod. Phys.* **67**, 249–265 (1995).
5. DiVincenzo, D. P. Two-bit gates are universal for quantum computation. *Phys. Rev. A.* **51**, 1015–1022 (1995).
6. Berman, G. P., Doolen, G. D., Hammel, P. C. & Tsifrinovich, V. I. Solid-state nuclear-spin quantum computer based on magnetic resonance force microscopy. *Phys. Rev. B* **61**, 14694–14699 (2000).
7. Stowe, T. D. *et al.* Attonewton force detection using ultrathin silicon cantilevers. *Appl. Phys. Lett.* **71**, 288–290 (1997).
8. Chui, B.W. *et al.* Mass-loaded cantilevers with suppressed higher-order modes for magnetic resonance force microscopy. *Technical Digest 12th Int. Conf. on Solid-State Sensors and Actuators (Transducers'03)* 1120–1123 (IEEE, Piscataway, 2003).
9. Stipe, B. C. *et al.* Electron spin relaxation near a micron-size ferromagnet. *Phys. Rev. Lett.* **87**, 277602 (2001).
10. Mozyrsky, D., Martin, I., Pelekhov, D. & Hammel, P. C. Theory of spin relaxation in magnetic resonance force microscopy. *Appl. Phys. Lett.* **82**, 1278–1280 (2003).
11. Berman, G. P., Gorshkov, V. N., Rugar, D. & Tsifrinovich, V. I. Spin relaxation caused by thermal excitations of high-frequency modes of cantilever vibration. *Phys. Rev. B* **68**, 094402 (2003).
12. Hannay, J. D., Chantrell, R. W. & Rugar, D. Thermal field fluctuations in a magnetic tip—implications for magnetic resonance force microscopy. *J. Appl. Phys.* **87**, 6827–6829 (2000).
13. Mamin, H. J., Budakian, R., Chui, B. W. & Rugar, D. Detection and manipulation of statistical polarization in small spin ensembles. *Phys. Rev. Lett.* **91**, 207604 (2003).
14. Castle, J. G., Feldman, D. W., Klemens, P. G. & Weeks, R. A. Electron spin-lattice relaxation at defect sites: E' centers in synthetic quartz at 3 kilo-Oersteds. *Phys. Rev.* **130**, 577–588 (1963).
15. Albrecht, T. R., Grütter, P., Horne, D. & Rugar, D. Frequency modulation detection using high-Q cantilevers for enhanced force microscope sensitivity. *J. Appl. Phys.* **69**, 668–673 (1991).
16. Slichter, C. P. *Principles of Magnetic Resonance*, 3rd edn, 20–24 (Springer, Berlin, 1990).
17. Berman, G. P., Kamenev, D. I. & Tsifrinovich, V. I. Stationary cantilever vibrations in oscillating-cantilever-driven adiabatic reversals: Magnetic-resonance-force-microscopy technique. *Phys. Rev. A.* **66**, 023405 (2002).
18. Berman, G. P., Borgonovi, F., Goan, H.-S., Gurvitz, S. A. & Tsifrinovich, V. I. Single-spin measurement and decoherence in magnetic-resonance-force microscopy. *Phys. Rev. B* **67**, 094425 (2003).
19. Brun, T. A. & Goan, H.-S. Realistic simulations of single-spin nondemolition measurement by magnetic resonance force microscopy. *Phys. Rev. A.* **68**, 032301 (2003).
20. Davenport, W. B. & Root, W. L. *An Introduction to the Theory of Random Signals and Noise* 104 (McGraw-Hill, New York, 1958).
21. Ting, M., Hero, A.O., Rugar, D., Yip, C.-Y. & Fessler, J.A. Electron spin detection in the frequency domain under the interrupted oscillating cantilever-driven adiabatic reversal (iOSCAR) protocol. Preprint at http://xxx.lanl.gov/abs/quant-ph/0312139 (2003).
22. Manassen, Y., Hamers, R. J., Demuth, J. E. & Castellano, A. J. Direct observation of the precession of individual paramagnetic spins on oxidized silicon surfaces. *Phys. Rev. Lett.* **62**, 2531–2534 (1989).
23. Durkan, C. & Welland, M. E. Electronic spin detection in molecules using scanning-tunneling-microscopy-assisted electron-spin resonance. *Appl. Phys. Lett.* **80**, 458–460 (2002).
24. Wrachtrup, J., von Borczyskowski, C., Bernard, J., Orritt, M. & Brown, R. Optical-detection of magnetic resonance in a single molecule. *Nature* **363**, 244–245 (1993).
25. Köhler, J. *et al.* Magnetic resonance of a single molecular spin. *Nature* **363**, 242–244 (1993).
26. Jelezko, F. *et al.* Single spin states in a defect center resolved by optical spectroscopy. *Appl. Phys. Lett.* **81**, 2160–2162 (2002).
27. Elzerman, J. M. *et al.* Single shot read-out of an individual electron spin in a quantum dot. *Nature* (in the press).
28. Jiang, H.-W., Xiao, M., Martin, I. & Yablonovitch, E. Electrical detection of electron spin resonance of a single spin in the SiO_2 of a Si field effect transistor. *Nature* (in the press).
29. Rugar, D., Yannoni, C. S. & Sidles, J. A. Mechanical detection of magnetic resonance. *Nature* **360**, 563–566 (1992).

Supplementary Information accompanies the paper on **www.nature.com/nature**.

....

Formation of zirconium metallic glass

Jianzhong Zhang & Yusheng Zhao

LANSCE Division, Los Alamos National Laboratory, Los Alamos, New Mexico 87545, USA

....

Bulk metallic glasses are commonly produced by the rapid cooling of liquid alloys[1]. They have emerged over the past decade as a novel class of materials, with attractive properties and technological promise[1,2]. The bulk metallic glasses so far produced contain three or more component elements[3,4]. These complex compositions are necessary to frustrate the crystallization of the liquid melt on cooling, but can also lead to phase separation, which is detrimental to the thermal and mechanical properties of metallic glasses[5–8]. Here we report, using X-ray diffraction measurements, the formation of a bulk metallic glass from elemental zirconium at high static pressures and low temperatures (relative to its melting temperature at atmospheric pressure). Amorphous zirconium can be recovered at ambient conditions and demonstrates a superior thermal stability compared to amorphous alloys[3,9], which could lead to new high-temperature applications of amorphous metals.

In multi-component systems, glass-forming ability (GFA) is viewed as the resistance to precipitation of crystalline phases from supercooled liquid metals[10], and alloys with high GFA all have three common features[3,4]: (1) they consist of at least three components; (2) there is significant mismatch of the atomic size of the constituent elements; and (3) there are negative heats of mixing among the major alloying elements. Addition of elements that are chemically and topologically different from the other species not only creates an energy barrier for nuclei to form but also effectively increases melt viscosity or fragility, which results in a reduced rate of both nucleation and growth and an increase in GFA. The production of bulk glassy materials in pure metals, however, remains a long-standing scientific curiosity and technological interest. The difficulties arise from the facts that the equilibrium melt viscosity of pure metals is three orders of magnitude smaller than that of amorphous alloys[11] and that current technology has yet to reach a cooling rate in excess of the $10^{10}\,°C\,s^{-1}$ that is needed to make pure metals amorphous[12].

We studied zirconium metal at pressures and temperatures up to 17 GPa and 1,000 °C, using energy-dispersive synchrotron X-ray diffraction and time-of-flight neutron scattering. In X-ray diffraction experiments, we used both DIA-type[13] and T-cup[14] large-volume high-pressure apparatus installed at Brookhaven and Argonne National Laboratories. Neutron scattering experiments were performed using a high-pressure/high-temperature (high P–T) cell assembly[15] in a TAP-98 toroidal-anvil press at Los Alamos Neutron Scattering Center. The starting sample of zirconium has a close-packed hexagonal structure (α-phase) and is of extremely high purity, with 35 p.p.m. Hf, less than 25 p.p.m. of C, N and Al,

MASS-LOADED CANTILEVERS WITH SUPPRESSED HIGHER-ORDER MODES FOR MAGNETIC RESONANCE FORCE MICROSCOPY

Benjamin W. Chui, Yoshikazu Hishinuma*, Raffi Budakian, H. Jonathon Mamin,
Thomas W. Kenny* and Daniel Rugar

IBM Research Division, Almaden Research Center, San Jose, CA 95120, USA
*Departments of Applied Physics and Mechanical Engineering, Stanford University, Stanford, CA 94305, USA
benchui@us.ibm.com, kenny@cdr.stanford.edu, rugar@almaden.ibm.com

ABSTRACT

We describe the design, fabrication and testing of mass-loaded cantilevers for electron-spin magnetic resonance force microscopy. These single-crystal silicon cantilevers are designed to have large gaps in their thermal mode spectra so as to reduce thermal noise near the electron-spin Rabi frequency. Each cantilever typically consists of a 2 μm thick mass suspended at the end of a 0.1 μm thick hinge. The fabrication process starts with an SOI wafer followed by selective silicon epitaxy, cantilever patterning, and backside release. The focus of the process is on precise thickness control and material homogeneity.

We will present characterization results for these cantilevers at room and low temperatures and discuss the impact of these devices on magnetic resonance force microscopy measurements.
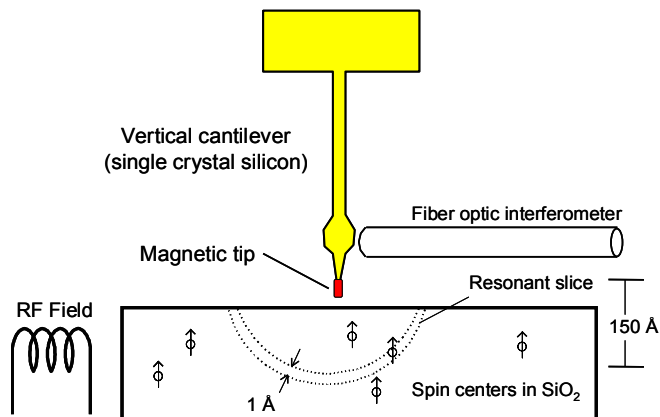
INTRODUCTION

Magnetic resonance force microscopy (MRFM) [1] uses an ultra-sensitive cantilever to detect magnetic resonance in small ensembles of spins (either nuclear spins or electron spins). The technique requires the detection of a very small (attonewton) oscillating magnetic force exerted on a magnetic tip by the spins in the sample [2, 3]. An RF magnetic field is used to manipulate the spin orientation at a rate that matches the kHz resonance frequency of the lever (Fig. 1).

To extend this technique to single-spin sensitivity, the magnetic tip must generate a very large magnetic gradient (e.g., several gauss per angstrom) in order to create a measurable force. Previous experimental and theoretical studies have shown, however, that sub-angstrom thermal vibration noise in the upper modes of the cantilever, in combination with the large gradient, creates enough magnetic noise to destabilize the spin [4–6].

To overcome this problem, the MHz-frequency thermo-mechanical noise of the cantilever must be suppressed. For detection of electron spins, the frequency range that is most important is in the range of 10 to 20 MHz, corresponding to the Rabi frequency of the spin. In this range, vibration noise of only a few milli-angstroms can be detrimental.

We have explored several approaches for suppressing the high-order mode noise [7]. This work focuses on mass-loaded cantilevers in particular (Fig. 2). Finite-element analysis shows these devices to have much lower noise spectral densities at MHz frequencies. This design can be engineered to have large gaps in the mode spectrum (Fig. 3).

Figure 1: One possible configuration for a magnetic resonance force microscopy measurement (MRFM) setup. The magnetized tip of an ultra-sensitive cantilever is brought in close proximity to the surface of a spin sample in the presence of an RF field. Vibration of the cantilever in combination with the RF field causes the spins within the resonant slice to undergo cyclic adiabatic reversals. The motion of the spins causes a slight shift in the cantilever's natural frequency. The coherence of the derived spin signal is affected by, amongst other factors, thermal noise in the cantilever itself.
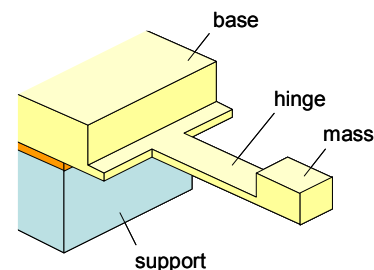

Figure 2: Schematic of a mass-loaded cantilever (not to scale). In this design, a large mass is suspended at the end of thin hinge which is connected to a stiff, thick base.
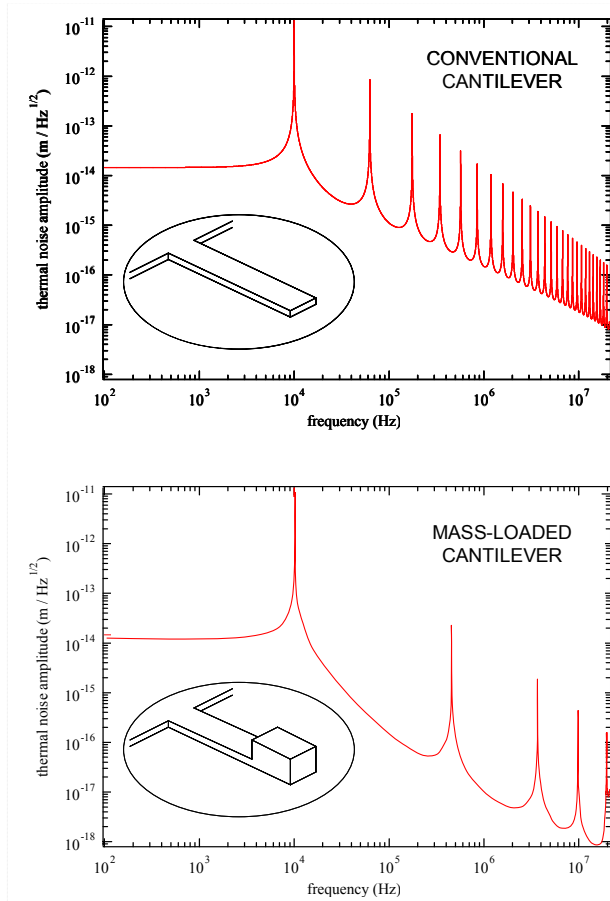
Presented at 12th International Conference on Solid-State Sensors, Actuators and Microsystems (Transducers'03), Boston, June 2003

Figure 3: Predicted thermal noise spectra based on finite element analysis for (a) conventional "flat" cantilever, and (b) mass-loaded cantilever. Note the large frequency gaps in graph (b).

DEVICE FABRICATION

Fabricating cantilevers for the present application poses special challenges. Unlike previous "flat" cantilevers [2], the present design calls for a dual-thickness structure, with a very thin (0.1 μm) "hinge" section coupled to a considerably thicker (2 μm) "mass". To minimize dissipation, the cantilever has to be made of single-crystal silicon, with surfaces that are as clean and defect-free as possible. The thickness of each section needs to be highly uniform as well. To minimize RF-induced and laser-induced self-heating, the silicon material must have very low electrical conductivity, i.e. it must be undoped or very lightly doped. Finally, to reduce clamping losses, the overhang at the base of the cantilever (due to backside misalignment) must be minimized, while the base itself should preferably be thickened and stiffened.

To address these requirements, we have chosen to make the cantilever hinge out of the undoped top silicon layer of a custom-made silicon-on-insulator (SOI) wafer, followed by selective undoped silicon epitaxy to form the mass.

The starting material is an SOI wafer with a 0.1 μm thick top silicon layer. A low-temperature oxide (LTO) layer is deposited and patterned to form a mask. This dark-field mask defines the thin part of the cantilever—the hinge (Fig. 4a). A 2 μm thick undoped single-crystal silicon epitaxy is grown. The epitaxy is selective, i.e. it does not grow over oxide. The oxide mask is then removed with HF (Fig. 4b).

Another LTO layer is subsequently deposited and patterned to form a second mask. This mask exposes mainly the base of the cantilever (Fig. 4c). A 3 μm thick single-crystal selective silicon epitaxy is then grown, and the LTO is removed with HF (Fig. 4d). At this point the thickness of the base is effectively 5 μm, providing the structural rigidity required for reducing clamping losses in the cantilever. A lithographic step is used to pattern the cantilever and its base, and a silicon plasma etch is used to define the lever (Fig. 4e). Note that this etch has to be very selective against oxide, since the thin regions of the top silicon layer (where there is no epitaxy) etches through early on during the etch and exposes the buried oxide to the plasma.

Finally, backside lithography followed by deep reactive ion etch (DRIE) is used to create through holes in the wafer. An HF etch is used to remove the buried oxide, and the cantilevers are released (Fig. 4f). In order to improve yield, a temporary nitride-LTO protective layer may be deposited on the front side of the wafer before the backside etch, and the nitride removed by plasma etching before the HF release.
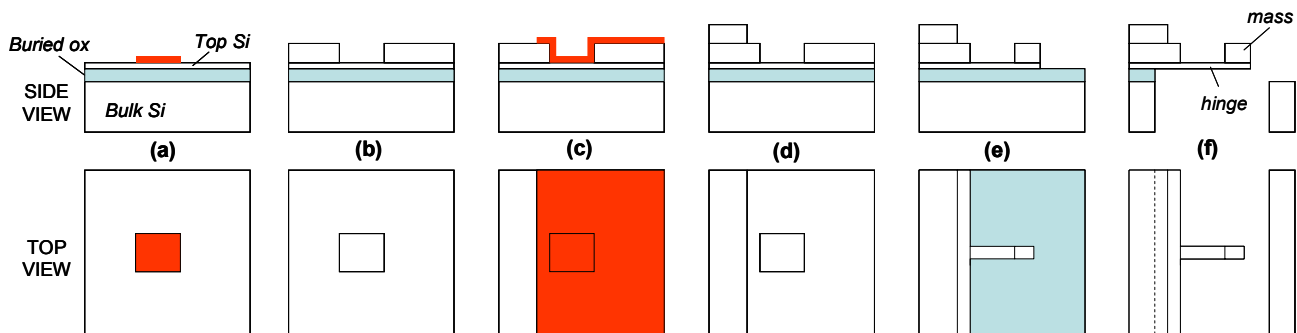

Figure 3: Fabrication process for mass-loaded cantilevers

Figure 6: Thermal mode spectrum of long-hinge cantilever measured at 77 K in vacuum. Numbers in parentheses are theoretical values obtained from finite element analysis.

Two types of cantilevers were fabricated—"long-hinge" ones (Fig. 5a) and "short-hinge" ones (Fig. 5b). Both types of cantilevers have large gaps in their mode spectra, but in practice the "long-hinge" design was used for all subsequent experiments because the "short-hinge" design proved to be extremely fragile even during normal handling. While both types of devices are sensitive to environmental shock, the high stress concentration in the hinge region of the "short-hinge" cantilever makes it much more likely to break.

In an alternate fabrication approach (not illustrated here), an SOI wafer with a *thick* top silicon layer is used. The hinge regions are thinned down using nitride-masked *loc*al *ox*idation of *si*licon much like the VLSI LOCOS process. This is a viable option if silicon epitaxy capability is not available. Possible drawbacks include potentially large variations in the final hinge thickness (corresponding to thickness variations in the initial top silicon layer), and the need for a long, precisely timed thermal oxidation step. Note the gradual transition in thickness between the hinge and the mass (Fig. 5c), characteristic of the LOCOS process.
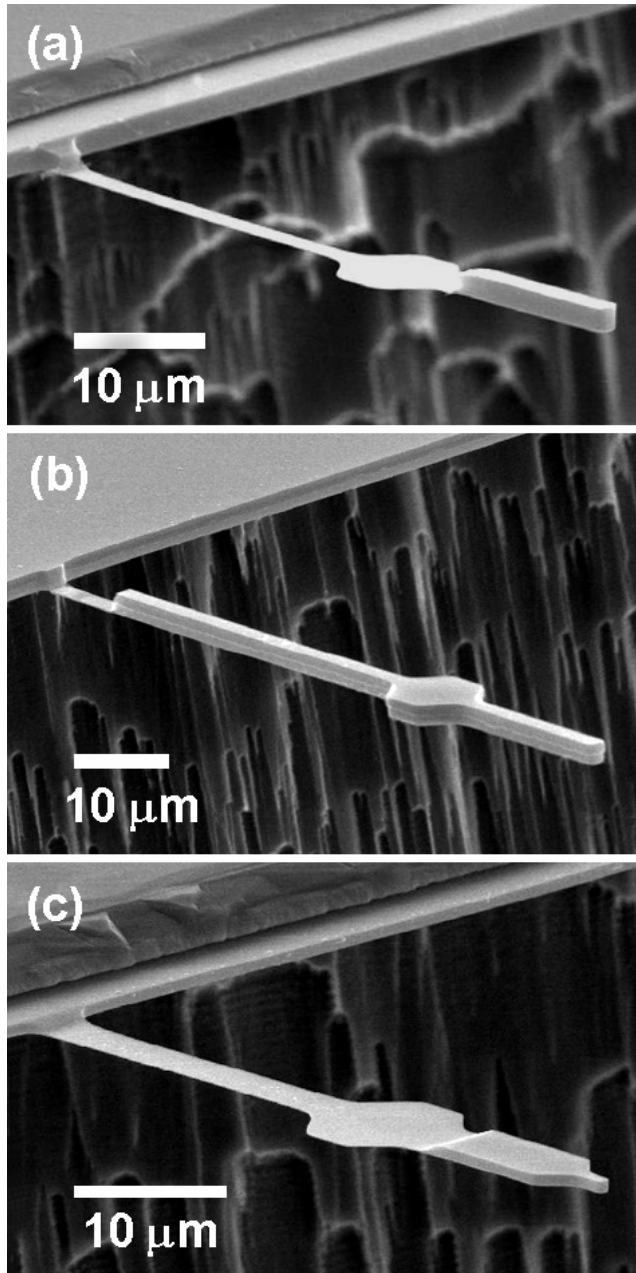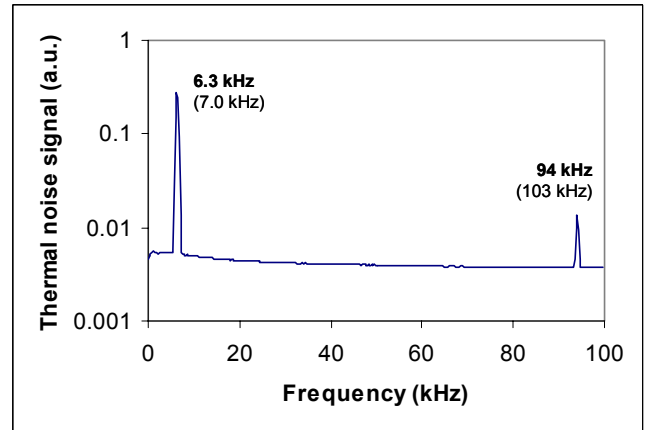

Figure 5: Mass-loaded cantilevers: (a) long-hinge design, (b) short-hinge design, and (c) alternate design fabricated using a LOCOS-like process. Devices similar to design (a) were used in the majority of measurements here.

Table 1: Predicted and measured modes for long-hinge cantilever (hinge dimensions 72 x 3 x 0.1 μm; mass dimensions 15 x 3 x 2.0 μm). Calculated stiffness: 0.3 mN/m. [*torsional modes not readily detectable]

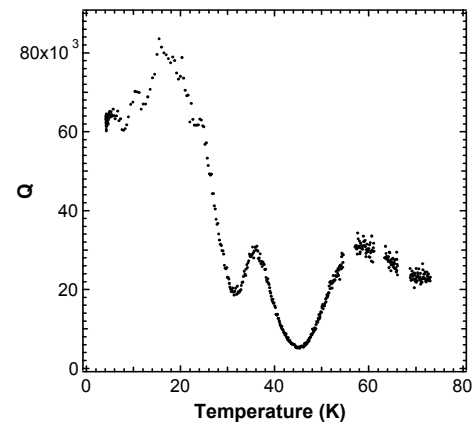|	**Measured**	Predicted	Type
Fund. mode (kHz)	**6.3**	7.0	Flexural
2nd mode (kHz)	**94**	103	Flexural
3rd mode (kHz)	*	186	Torsional
4th mode (kHz)	**265**	323	Flexural
5th mode (kHz)	*	343	Torsional

Figure 7: Quality factor Q of a long-hinge mass-loaded cantilever versus temperature, measured in vacuum. The cantilever has a magnetic particle glued to its tip. Q at room temperature is approximately 15000.

DEVICE CHARACTERIZATION

For characterization purposes, a long-hinge cantilever was mounted in a setup that includes a fiber-based laser interferometer. The thermal mode spectrum of the cantilever was measured and plotted in Fig. 6 (see also Table 1). It can be seen that, as expected, there is a large gap between the fundamental mode and the higher modes. Theoretically obtained modal frequencies (calculated through finite element analysis) are seen to be in good agreement with the measured values.

The quality factor Q of a long-hinge cantilever was measured in vacuum as a function of temperature. Results are shown in Figure 7. It can be seen that Q can reach 80000, and that it varies with temperature. In general, at low temperatures the effect of surface contaminants are "frozen out" and their contribution to surface losses decreases, leading to higher Q.

In the experimental configuration used for our MRFM measurements (see Fig. 1), a small magnetic particle is attached to the tip of the cantilever which is placed in close proximity (approximately 0.1 μm) to an electron-spin sample. A modulated RF field is applied to manipulate the electron spins, and the motion of the cantilever resulting from the tip-sample interaction is detected. Because the cantilever is very soft (0.3 mN/m), attonewton-scale forces can be detected using this setup with the help of a high-performance laser interferometer.

As an illustration of how cantilever modes can influence spin-detection sensitivity, MRFM measurements were taken at various RF power levels (Fig. 8). Varying the RF power changes the associated magnetic field strength, which in turn changes the spin's Rabi frequency. The suppression of the spin signal at 3 dBm may be due to thermal noise in a cantilever mode that coincides with the Rabi frequency at that point.

Very promising results have been obtained so far with the mass-loaded cantilevers in our MRFM measurements. At the time of writing, spin signals with a noise floor of 10 spins have been obtained. Latest results will be reported in detail separately [8].

REFERENCES

[1] "Magnetic resonance force microscopy," J.A. Sidles, J.L. Garbini, K.J. Bruland, D. Rugar, O. Zuger, S. Hoen, and C.S. Yannoni, *Rev. Mod. Phys.,* 67 (1), pp. 249-65, 1995.
[2] "Attonewton force detection using ultrathin silicon cantilevers," T.D. Stowe, K. Yasumura, T.W. Kenny, D. Botkin, K. Wago, and D. Rugar, *Appl. Phys. Lett.,* 71 (2), pp. 288-90, 1997.
[3] "Sub-attonewton force detection at milliKelvin temperatures," H.J. Mamin, D. Rugar, *Appl. Phys. Lett.,* 79 (20), pp. 3358-60, 2001.
[4] J.A. Sidles, personal communication.
[5] "Spin relaxation in MRFM experiments," D. Mozyrsky, I. Martin, D. Pelekhov, and P.C. Hammel, to be published.
[6] "Spin relaxation caused by thermal excitations of high-frequency modes of cantilever vibrations," G.P. Berman, V.N. Gorshkov, D. Rugar, and V.I. Tsifrinovich, to be published.
[7] "Torsional force probes optimized for higher order mode suppression," T.D. Stowe, K. Yasumura, T. Pfafman, T.W. Kenny, D. Botkin, and D. Rugar, Transducers '97 Tech. Digest, pp. 141-4.
[8] Paper in preparation, H.J. Mamin, R. Budakian, B.W. Chui, and D. Rugar, to be submitted to *Phys. Rev. Lett.*
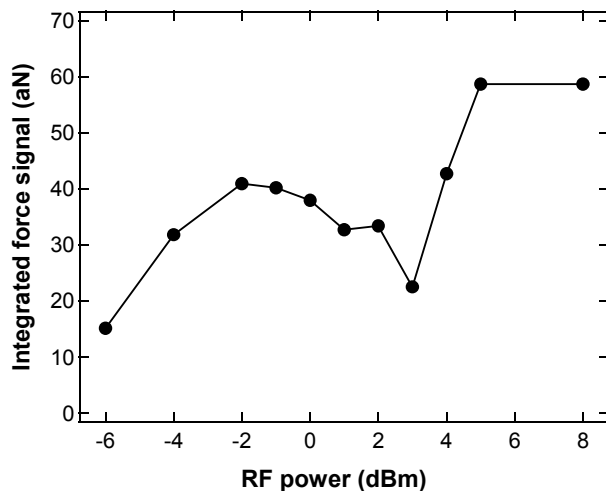

Figure 8: Spin signal vs. RF power. Varying the RF power changes the associated magnetic field strength, which in turn changes the spin's Rabi frequency. The suppression of the signal at 3 dBm may be due to thermal noise in a cantilever mode that coincides with the Rabi frequency at that point (around 6 MHz).

Detection and Manipulation of Statistical Polarization in Small Spin Ensembles

H. J. Mamin,* R. Budakian, B.W. Chui, and D. Rugar

IBM Research Division, Almaden Research Center, 650 Harry Road, San Jose, California 95120-6099, USA
(Received 14 July 2003; published 13 November 2003)

We report the detection of the $\sqrt{N}$ statistical polarization in a small ensemble of electron spin centers in SiO_2 by magnetic resonance force microscopy. A novel detection technique was employed that captures the statistical polarization and cycles it between states that are either locked or antilocked to the effective field in the rotating frame. Using field gradients as high as 5 G/nm, we achieved a detection sensitivity equivalent to roughly two electron spins, and observed ultralong spin-lock lifetimes, as long as 20 s. Given a sufficient signal-to-noise ratio, this scheme should be extendable to single electron spin detection.

In his classic paper on nuclear induction, Bloch pointed out that a system of N magnetic moments μ will give rise to a statistical polarization of order $\sqrt{N}\mu$ [1]. For the large spin ensembles typically used in conventional magnetic resonance experiments, this statistical polarization is negligible compared to the thermal equilibrium (Boltzmann) polarization. However, for sufficiently small spin ensembles (especially as N approaches unity), the statistical polarization can exceed the Boltzmann polarization and even dominate. Given a sufficiently sensitive means to detect magnetic resonance, it should be possible to make use of the self-polarizing nature of small spin ensembles to perform magnetic resonance experiments, just as one manipulates and measures conventionally polarized ensembles [2,3]. This approach offers one route for performing magnetic resonance experiments on small numbers of spins, perhaps even a single spin.

In the present work, we exploit the exquisite sensitivity of magnetic resonance force microscopy (MRFM) [4–8] and demonstrate a detection sensitivity equivalent to two spins in a 0.1 Hz measurement bandwidth. This represents nearly 2 orders of magnitude improvement over previous MRFM results [8]. We apply the technique to spin ensembles consisting of fewer than 10^2 electron spins and study statistical polarizations of order 10 spins. Rather than detecting the free precession of the transverse magnetization, which was demonstrated previously for very large ($N \sim 10^{23}$) ensembles of nuclear spins [9–13], we detect the *longitudinal* component in the "rotating frame" using the technique of adiabatic rapid passage. By applying a microwave field that is initially off-resonance, and then bringing the spins into resonance, the spins stay "spin-locked" to the effective field for times of order $T_{1\rho}$, the spin-lattice relaxation time in the rotating frame [14,15]. Since $T_{1\rho}$ is orders of magnitude longer than the usual spin decoherence time T_2, the statistical spin signals we detect exhibit much greater coherence than signals from the free precession of the transverse spin component.

As shown in Fig. 1, our MRFM experiment is based on an ultrasensitive cantilever mounted perpendicular to the sample. At the end of the cantilever is a micron-size SmCo magnetic particle that generates a strong magnetic field gradient ($\gtrsim 2$ G/nm). A microwave field $B_1 \sim 3$ G from a superconducting resonator [16] is applied to excite electron spin resonance. The inhomogeneity of the tip field confines the magnetic resonance to the region that satisfies the condition $B_0(x, y, z) = \omega/\gamma$, where ω is the frequency of the microwave field, γ is the gyromagnetic ratio ($\gamma/2\pi = 2.8 \times 10^6$ Hz/G), and B_0 is the tip field
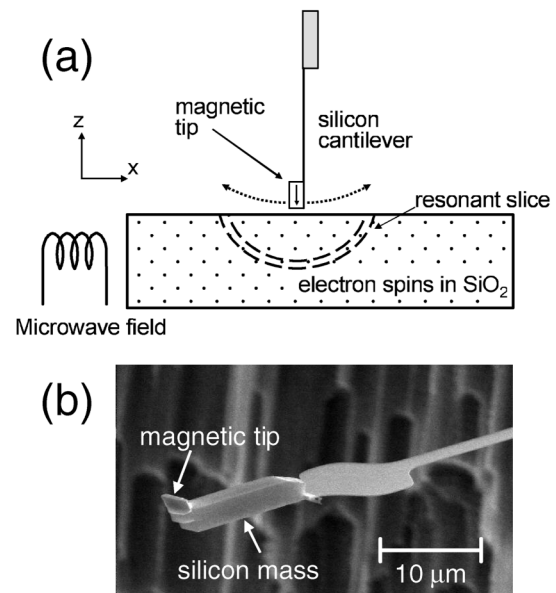
FIG. 1. (a) Schematic of the MRFM experiment. As the cantilever oscillates, the spins near the resonant slice are cyclically inverted, resulting in a small cantilever frequency shift. Cantilever position is detected using an optical fiber interferometer (not shown). (b) Scanning electron micrograph of the single-crystal silicon cantilever with the larger (micron-size) magnetic tip. The cantilever had a mass-loaded geometry in order to suppress motion of the tip for higher order flexural modes.

plus an optional external field. In our case, microwaves were applied at 2.96 GHz, so the resonance condition was $B_0(x, y, z) = 1060$ G. The entire microscope was operated at 200 mK in a small vacuum chamber attached to the bottom of the mixing chamber of a dilution refrigerator.

The two single-crystal silicon cantilevers used for this study had a mass-loaded design, consisting of a roughly 100 nm thick, 70 μm long shaft, with a 2 μm $\times$ 15 μm silicon mass at the end [Fig. 1(b)]. The purpose of the mass loading was to suppress the thermal motion at the end for the higher order cantilever modes [17]. These modes can cause unwanted spin relaxation due to vibrationally induced magnetic noise near the Rabi frequency ($\omega_{\text{Rabi}} = \gamma B_1$) [18–20]. One cantilever had a ~ 1 μm magnetic tip attached to its end to generate the field gradient. In order to increase the field gradient, the second cantilever had a magnetic particle that was shaped using a focused ion beam so that the tip tapered down to a 250 nm wide apex. The cantilevers had spring constants k of about 6×10^{-4} N/m, frequencies f_c of 6600 and 8600 Hz, respectively, and Q's of order 50 000 for temperatures below 4 K.

Two samples of optically polished vitreous silica were studied. Both samples were irradiated by ^{60}Co gamma rays to produce silicon dangling bonds known as E' centers [15,21]. The high spin density sample (Corning 7943) had a spin density of $\sim 10^{18}$ cm^{-3} and was studied with the larger tip. The sample with lower spin density (Suprasil W2) had a spin density of $\sim 10^{15}$ cm^{-3} and was studied with the smaller tip.

To detect the electron spins, we look for a shift in cantilever resonance frequency using the OSCAR (oscillating cantilever-driven adiabatic reversal) protocol [8]. The cantilever is self-oscillated at its resonance frequency through the use of a gain-controlled positive feedback loop [22]. As the cantilever position oscillates sinusoidally according to $x_c(t) = x_{\text{pk}} \cos(\omega t)$, the field B_0 at a given sample location is modulated because of the field gradient from the tip $G = \partial B_0 / \partial x$. In the rotating frame, the effective field $\mathbf{B}_{\text{eff}}$ can be written as [14] $\mathbf{B}_{\text{eff}}(t) = B_1 \hat{\mathbf{x}} + [B_0(t) - \omega/\gamma]\hat{\mathbf{z}} = B_1 \hat{\mathbf{x}} + Gx_c(t)\hat{\mathbf{z}}$, where we have assumed that the resonance condition is fulfilled for $x_c = 0$. If $\mathbf{B}_{\text{eff}}$ changes sufficiently slowly, the spins will be "spin locked" (or antilocked) to $\mathbf{B}_{\text{eff}}$. Under these circumstances, the $\hat{\mathbf{z}}$ component of magnetization will therefore oscillate synchronously with the cantilever position as

$$m_z(t) = \pm \frac{Gx_c(t)}{\sqrt{B_1^2 + (Gx_c(t))^2}} m_{\text{eff}}, \qquad (1)$$

where m_{eff} is the component of the magnetization along $\mathbf{B}_{\text{eff}}$ and the sign depends on whether m_{eff} is aligned or antialigned with $\mathbf{B}_{\text{eff}}$ (i.e., locked or antilocked).

Because of the back-action force on the magnetic tip from the spins, the oscillating $m_z(t)$ results in a frequency shift of the cantilever, which is detected by an analog

frequency demodulator [22]. In the limit $Gx_{\text{pk}} \gg B_1$, the frequency shift δf_c is calculated to be [23]

$$\delta f_c = \pm (2f_c G / \pi k x_{\text{pk}}) m_{\text{eff}}. \qquad (2)$$

Note that δf_c is directly proportional to m_{eff}, the spin moment aligned with the effective field in the rotating frame. In the present experiment, m_{eff} is the result of statistical polarization and, over time, will fluctuate and even reverse sign with correlation time on the order of $T_{1\rho}$ [24].

The above description applies to a localized region of the resonant slice. The total frequency shift will be a sum of contributions from the entire slice. Since the spins that are in different regions of the slice experience various values of G, they will contribute with differing weights to the overall frequency shift. In particular, because of the perpendicular cantilever geometry, spins near the surface, off to either side of the cantilever, contribute with the strongest weight, while spins directly below the tip, where $G = 0$, contribute minimally. Because of symmetry, the measurement responds only to the left-right statistical imbalance of m_{eff}.

To improve detectability in the presence of low frequency noise, and to endow the spin signal with a distinctive signature, we cycle the spins between locked and antilocked using a variation of the protocol we refer to as "interrupted OSCAR." The microwave field B_1 is normally on, but it is then interrupted periodically for one-half of a cantilever cycle, starting at a cantilever extremum, as shown in Fig. 2 (curve B). During the time the microwaves are off, m_z remains essentially static. Since the cantilever continues to oscillate, when
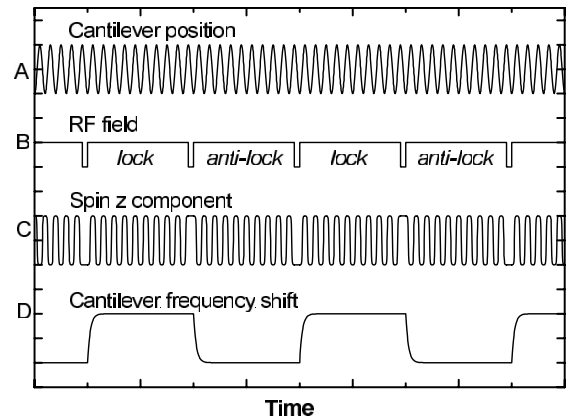
FIG. 2.   Timing diagram for the interrupted OSCAR protocol. The cantilever is oscillated continuously. The microwave field (curve B) is normally on, but is periodically interrupted for one-half cantilever cycle. The $\mathbf{z}$ component of the magnetization (C) oscillates in response to the cantilever motion due to adiabatic rapid passage when the microwaves are on, but is left static when they are off. The oscillating magnetization reverses phase with respect to the cantilever for each microwave interruption, giving a cantilever frequency shift (D) that oscillates at one-half the microwave interrupt frequency.

the microwaves are turned back on after the half-cycle gap, $\mathbf{B}_{\mathrm{eff}}$ will have reversed orientation, and the magnetization will have changed from locked to antilocked. This change from locked to antilocked and vice versa occurs every interrupt cycle, resulting in a cantilever frequency shift (curve D) that oscillates at one-half the microwave interrupt frequency f_{int}. The fact that the signal is at a subharmonic of f_{int} gives it a very distinctive signature that is free of spurious feedthrough artifacts.

Although somewhat subtle in concept, the interrupted OSCAR scheme is actually quite simple in practice. Once the cantilever is self-oscillating and pulses with correct timing are used to gate the microwaves, one can simply look for a peak at $f_{\mathrm{int}}/2$ in the power spectrum of the frequency demodulated signal D. Alternatively, phase sensitive detection via a lock-in amplifier can be employed to detect both the magnitude and the sense of the net polarization m_{eff}. In either case, this scheme has the appealing feature that there is no need to wait a spin-lattice relaxation time T_1 between measurements for the sample to repolarize, since we do not rely on the Boltzmann polarization. This aspect is potentially quite useful in increasing the efficiency of taking data in systems with long T_1 times [3,10].

Figure 3(a) shows a power spectrum of the frequency demodulated cantilever signal obtained for the case of the low density sample. When the microwaves were inter-

rupted at 99 Hz, a prominent peak was seen at 49.5 Hz, as expected. The peak disappeared when the microwave power was turned off, when the microwaves were applied cw, when the sample was retracted, or when the external field was adjusted so that the resonant slice was no longer in the sample.

The sharpness of this spectral feature ($\Delta f_{\mathrm{sig}} = 0.12$ Hz FWHM) implies that the statistical polarization has an extraordinarily long correlation time τ_m, nearly 3 s, as given by $\tau_m = 1/\pi\Delta f_{\mathrm{sig}}$. The time τ_m depended on the cantilever oscillation amplitude, among other parameters, and was observed to be as long as 20 s for the case of 60 nm amplitude. [The larger the amplitude, the more complete the adiabatic passages, as seen by Eq. (1), and the more time the spins are off-resonance.] The time τ_m is related to $T_{1\rho}$ and is ultimately limited by spin relaxation caused by magnetic noise produced by the tip [8,18,20].

Figure 3(b) shows a sequence of power spectra taken with the high spin density sample as the tip was retracted using a piezoelectric actuator. Each curve was taken with the spacing increased by 25 nm. The signal decreased, corresponding to the smaller volume of the resonant slice within the sample, until finally the slice was pulled out of the sample completely.

By using synchronous detection to detect the interrupted OSCAR signal, we could monitor fluctuations of the statistical polarization in real time. Figure 4(a) shows the spin fluctuations for the low density sample. Note that significant deviations from the mean can persist for several or even tens of seconds. When the microwaves were applied cw, only the background noise remained, giving the background signal shown in Fig. 4(b).
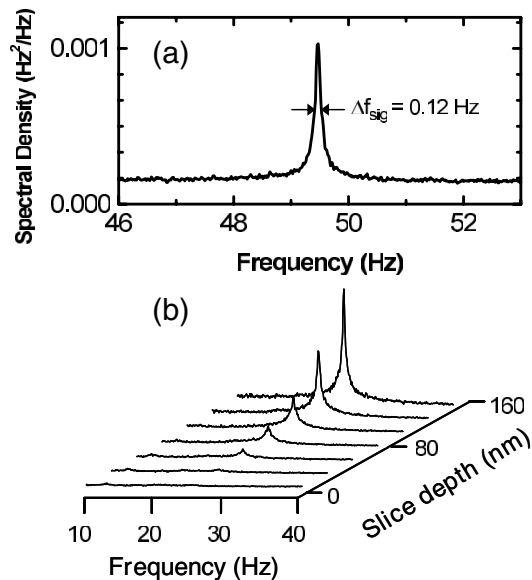
FIG. 3. (a) Power spectral density of the frequency demodulated signal for the low spin density sample. The peak at 49.5 Hz is the statistical spin signal. The integrated signal in the peak is equivalent to that from about 6 spins, and the baseline noise is 1.8 spins in the 0.12 Hz natural bandwidth. The cantilever oscillation amplitude was 10 nm, and the resonant slice extended roughly 100 nm below the surface. (b) Similar spectra from the high spin density sample at various tip-sample spacings. As the resonant slice was pulled out of the sample, the spin signal decreased monotonically.
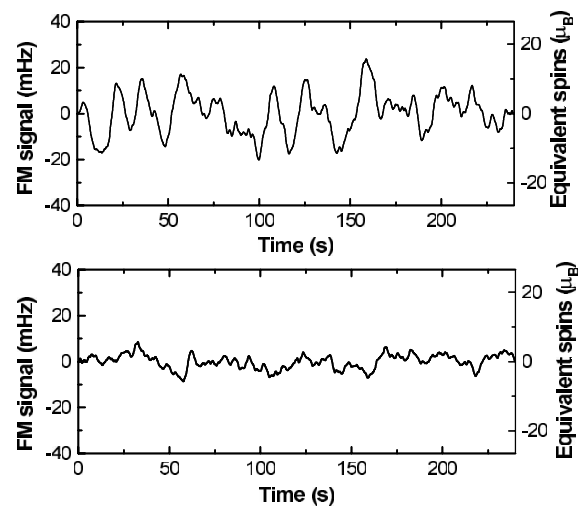
FIG. 4. (a) Output of lock-in amplifier showing real-time spin fluctuations for the low spin density sample. The net polarization wanders between being in-phase or antiphase with the lock-antilock cycling. The correlation time is on the order 10 s. The lock-in filter time constant was 3 s. (b) Lock-in amplifier output showing the baseline noise level equivalent to 2.1 spins rms.

If we know the field gradient, we can deduce the number of spins responsible for the signal using Eq. (2). We do not have the ability to measure $G = \partial B_0/\partial x$ directly, but we have measured the related derivative $\partial B_z/\partial z$, which can be used to estimate G given a model for the tip. To determine $\partial B_z/\partial z$, we measured the lock-in signal as a function of external field, for two different values of tip-to-sample spacing [8,25]. For the smaller tip, we found that retracting the tip by 55 nm was equivalent to offsetting the field by 300 G. Thus, the axial field gradient $\partial B_z/\partial z$ in the center of that field range is given by $\Delta B/\Delta z = 5.5$ G/nm. The tip was then modeled simply as a uniformly magnetized spherical tip 0.4 μm in diameter, a value chosen to fit the measured $\partial B_z/\partial z$. The resulting value for G off to the side of the tip at the sample surface was then calculated to be 4.3 G/nm.

Assuming this field gradient, we can use Eq. (2) to assign units of Bohr magnetons (μ_B) to the curves in Fig. 3(a) and 4. The integrated peak in Fig. 3(a) corresponds to $5.5\mu_B$ rms. The baseline noise level in the signal bandwidth of 0.12 Hz corresponds to $1.8\mu_B$ rms. In Fig. 4(a), the spin signal fluctuations correspond to $6.3\mu_B$ rms, and the background noise level in Fig. 4(b) is $2.1\mu_B$ rms in the 0.1 Hz noise bandwidth of the lock-in amplifier.

The above numbers are not literally the number of net spins responsible for the signal. Many of the spins, such as those directly under the tip, are in regions where G is much lower than the assumed value. In addition, some are not optimally placed within the middle of the resonant slice, and therefore Eq. (2) overestimates their contribution. We simply point out that the signals observed are equivalent in strength to the given number of spins, provided that they were all optimally situated at the stated field gradient and undergoing full adiabatic reversals.

Unambiguous detection of a single, isolated spin will require a sample with a reduced density of spin centers (i.e., less than one spin on average within the resonant slice volume). Improved signal-to-noise ratio (SNR) will also be necessary in order to locate the spin in a reasonable amount of time. Because the sign of the spin signal will fluctuate, signal averaging must be performed on a positive definite quantity such as the signal *power*. Such averaging is very inefficient when the single-shot SNR is low, improving only as $n^{1/4}$, where n is the number of averages [26,27]. To reduce the rms noise from 2 spins to 0.2 spin, for example, would therefore require a 10^4 times increase in averaging time. Thus, for practical single-spin detection, more fundamental improvements are required, such as increasing the field gradient to increase the magnitude of the force signal, or reducing the noise, currently dominated by tip-surface interactions [28].

*Electronic address: mamin@almaden.ibm.com
[1] F. Bloch, Phys. Rev. **70**, 460 (1946).
[2] M. Bloom, in *Nuclear Magnetic Double Resonance*, Proceedings of the International School of Physics "Enrico Fermi," edited by B. Maraviglia (North-Holland, Amsterdam, 1993), pp. 473–484.
[3] P. L. Carson, L. A. Madsen, G. M. Leskowitz, and D. P. Weitekamp, U.S. Patents No. 6 078 082 and No. 6 081 119 (2000).
[4] J. A. Sidles, Phys. Rev. Lett. **68**, 1124 (1992).
[5] D. Rugar, C. S. Yannoni, and J. A. Sidles, Nature (London) **360**, 563 (1992).
[6] J. Sidles, J. Garbini, K. Bruland, D. Rugar, O. Zueger, S. Hoen, and C. Yannoni, Rev. Mod. Phys. **67**, 249 (1995).
[7] Z. Zhang, P. C. Hammel, and P. E. Wigen, Appl. Phys. Lett. **68**, 2005 (1996).
[8] B. Stipe, H. Mamin, C. Yannoni, T. Stowe, T. Kenny, and D. Rugar, Phys. Rev. Lett. **87**, 277602 (2001).
[9] T. Sleator, E. Hahn, C. Hilbert, and J. Clarke, Phys. Rev. Lett. **55**, 1742 (1985).
[10] T. Sleator, E. Hahn, C. Hilbert, and J. Clarke, Phys. Rev. B **36**, 1969 (1987).
[11] M. McCoy and R. Ernst, Chem. Phys. Lett. **159**, 587 (1989).
[12] M. Guéron and J. Leroy, J. Magn. Reson. **85**, 209 (1989).
[13] D. Hoult and N. Ginsberg, J. Magn. Reson. **148**, 182 (2001).
[14] C. P. Slichter, *Principles of Magnetic Resonance* (Springer-Verlag, New York, 1990), 3rd ed., Chaps. 2 and 6.
[15] K. Wago, D. Botkin, C. S. Yannoni, and D. Rugar, Phys. Rev. B **57**, 1108 (1998).
[16] H. J. Mamin, R. Budakian, and D. Rugar, Rev. Sci. Instrum. **74**, 2749 (2003).
[17] B. W. Chui, Y. Hishinuma, R. Budakian, H. J. Mamin, T. W. Kenny, and D. Rugar, in *Digest of Transducers '03, Boston, 2003* (IEEE, New York, 2003), p. 1120.
[18] D. Mozyrsky, I. Martin, D. Pelekhov, and P. C. Hammel, Appl. Phys. Lett. **82**, 1278 (2003).
[19] J. Sidles (private communication).
[20] G. P. Berman, V. N. Gorshkov, D. Rugar, and V. I. Tsifrinovich, Phys. Rev. B **68**, 094402 (2003).
[21] J. G. Castle, D. W. Feldman, P. G. Klemens, and R. A. Weeks, Phys. Rev. **130**, 577 (1963).
[22] T. R. Albrecht, P. Grütter, D. Horne, and D. Rugar, J. Appl. Phys. **69**, 668 (1991).
[23] G. P. Berman, D. I. Kamenev, and V. I. Tsifrinovich, Phys. Rev. A **66**, 023405 (2002).
[24] In previous MRFM measurements, the signal was due to the Boltzmann polarization achieved by waiting $\sim T_1$ with the microwave field off (see Ref. [8]). During the MRFM measurement, m_{eff} decays in time $\sim T_{1\rho}$, until only the statistical polarization remains.
[25] K. J. Bruland, W. M. Dougherty, J. L. Garbini, J. A. Sidles, and S. H. Chao, Appl. Phys. Lett. **73**, 3159 (1998).
[26] K. Wago, Ph.D. thesis, Stanford University, 1997.
[27] A. E. E. Rogers, S. S. Doeleman, and J. M. Moran, Astron. J. **109**, 1391 (1995).
[28] B. C. Stipe, H. J. Mamin, T. D. Stowe, T. W. Kenny, and D. Rugar, Phys. Rev. Lett. **87**, 096801 (2001).

Creating Order from Random Fluctuations in Small Spin Ensembles

R. Budakian,* H. J. Mamin, B. W. Chui, D. Rugar

We demonstrate the ability to create spin order by using a magnetic resonance force microscope to harness the naturally occurring statistical fluctuations in small ensembles of electron spins. In one method, we hyperpolarized the spin system by selectively capturing the transient spin order created by the statistical fluctuations. In a second method, we took a more active approach and rectified the spin fluctuations by applying real-time feedback to the entire spin ensemble. The created spin order can be stored in the laboratory frame for a period on the order of the longitudinal relaxation time of 30 seconds and then read out.

Creating order from random thermal fluctuations has been of interest to physicists since the development of statistical mechanics in the 19th century (1). In a more modern context, creating order in microscopic physical systems is an essential part of quantum information processing and quantum computation (2–4), where the ability to set the state of a collection of quantum objects to a desired configuration is required. The device used to perform this operation must be capable of controlling the microscopic degrees of freedom of the system while being subjected to environmental fluctuations.

Here, we take advantage of the outstanding sensitivity of magnetic resonance microscopy (MRFM) to follow statistical $\sqrt{N}$ fluctuations in small ensembles of electron spins (5, 6) with a real-time sensitivity corresponding to $1.3\mu_B$, where μ_B is the Bohr magneton. The spin manipulation protocols we have developed allow us to monitor and respond to the instantaneous spin imbalance in the rotating frame. By monitoring the spin system and selectively capturing the large positive fluctuations, we have created a mean polarization corresponding to $\sim6\mu_B$ in an ensemble of $N \approx 70$ spins. We also used real-time feedback to effectively cool the spin system and create a mean polarization corresponding to $\sim7\mu_B$. The spin order was then transferred to the laboratory frame, stored, and later read out.

In MRFM detection, spins are manipulated by using magnetic resonance, and the longitudinal component of the magnetization is detected mechanically by measuring the interaction between the spins and a small permanent magnet attached to the end of a sensitive silicon cantilever. Typically, the

force generated by a spin on the cantilever is quite small. An electron spin will produce a force of only 2×10^{-18} N when subjected to a magnetic field gradient from the tip as large as 2×10^5 T m^{-1}. Sensitivity to such small forces requires the ability to coherently manipulate spins for many cycles of the cantilever. Recently, through the use of specially engineered cantilevers that reduce disturbance to the spins (7–9), we observed longitudinal relaxation times in the rotating frame (i.e., during measurement) of up to several seconds. This has allowed us to realize a single-shot detection sensitivity approaching the single spin level (5) and the detection of an isolated electron spin by signal averaging (6).

In the experimental setup of the MRFM apparatus (Fig. 1A), a custom-fabricated mass-loaded silicon cantilever with a submicrometer SmCo magnetic particle attached to the tip is used as the force-sensing element (5, 6). The sample consists of vitreous silica (Suprasil W2, Heraeus Quarzglas GmbH and Company KG, Hanau, Germany) that has

been irradiated by gamma rays from a ^{60}Co source to produce spin-1/2 paramagnetic defects or E' centers (unpaired electron spins on Si) (10). Experiments were performed with two different cantilever and sample combinations. In setup 1, a cantilever having a fundamental resonance frequency $f_c = 8.7$ kHz and stiffness $k = 0.6$ mN m^{-1} with a 250-nm-wide SmCo tip was used with a sample that had a spin concentration of $\sim10^{15}$ cm^{-3}. In setup 2, a cantilever with $f_c = 5.5$ kHz, $k = 0.11$ mN m^{-1}, and a 150-nm-wide SmCo tip was used with a $\sim10^{14}$ cm^{-3} concentration sample. The MRFM apparatus was operated in vacuum and cooled to 300 mK to reduce the thermal vibrations of the cantilever.

Electron spin resonance was excited at $\omega_{rf}/2\pi = 2.96$ GHz with the use of a microwave field with amplitude $B_1 \approx 0.3$ mT. In the presence of the inhomogeneous field from the tip, only those spins within a thin resonant slice satisfying the resonance condition given by $B_0(x,y,z) \equiv |\mathbf{B}_{tip}(x,y,z) + B_{ext}\hat{\mathbf{z}}| = \omega_{rf}/\gamma$ will interact with the microwave field. Here, $B_0(x, y, z)$ is the sum of the tip field, $\mathbf{B}_{tip}(x, y, z)$, and a uniform external field, $B_{ext}\hat{\mathbf{z}}$, produced by a superconducting magnet, and γ is the gyromagnetic ratio ($\gamma/2\pi = 2.8 \times 10^{10}$ Hz T^{-1}). For the vertical orientation of the cantilever shown in Fig. 1A, only those spins that are slightly to the left or right of the tip contribute to the signal. Furthermore, because of symmetry, the cantilever will respond only to the left-right imbalance of spin polarization.

To detect spins, we use the recently developed spin manipulation protocol OSCAR (oscillating cantilever-driven adiabatic reversal), which measures the shift in the fundamental frequency of the cantilever in response to tip-spin interactions (5, 6, 11). The cantilever is self-oscillated at its fundamental resonance frequency by using a piezoelectric transducer that drives the cantilever to a fixed amplitude x_{pk} (11, 12). As the cantilever position oscillates according to $x_c(t) =$
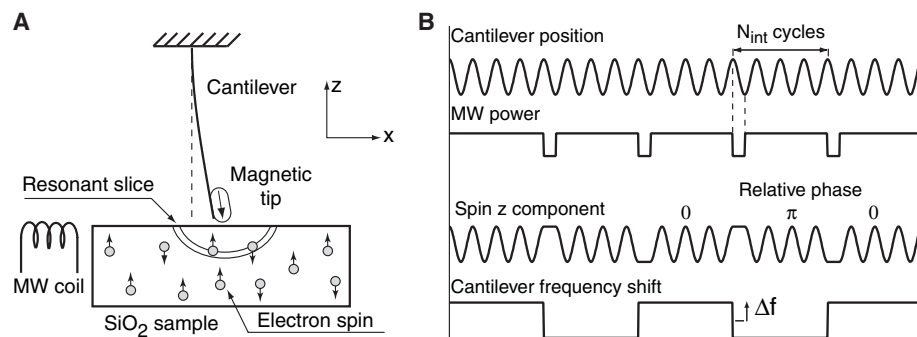
IBM Research Division, Almaden Research Center, 650 Harry Road, San Jose, CA 95120, USA.

*To whom correspondence should be addressed. E-mail: budakian@us.ibm.com

Fig. 1. (**A**) Schematic of the MRFM apparatus. The cantilever with the attached magnetic tip is oriented vertically about 140 nm away from the surface of a sample containing a low concentration of E' centers. A small coil placed near the sample generates microwaves at 2.96 GHz to excite electron spin resonance. At 2.96 GHz, the resonance condition for electrons is met for $B_0 = 106$ mT. For $B_{ext} = 30$ mT, the resonant slice is a paraboloidal shell that extends about 250 nm below the tip. (**B**) Timing diagram for the interrupted OSCAR protocol. For setups 1 and 2, the microwave (MW) power is interrupted every 88 cycles ($f_{sig} \approx 50$ Hz) and 64 cycles ($f_{sig} \approx 43$ Hz), respectively.

$x_{pk}\sin(2\pi f_c t)$, the field experienced by a spin near the tip is modulated sinusoidally at the cantilever frequency with peak amplitude $\Delta B = G x_{pk}$, where $G = \partial B_0 / \partial x$ is the lateral gradient from the tip. For typical experimental parameters of $x_{pk} \approx 20$ nm and $G \approx 2 \times 10^5$ T m^{-1}, the external field experienced by spins within the resonant slice is modulated by $\Delta B = 4$ mT. In the presence of the microwave field, the slow variation of the static field at the cantilever frequency causes each spin within the resonant slice to be adiabatically inverted synchronously with the cantilever motion. The back action of the spin on the cantilever in turn shifts the fundamental frequency of the cantilever by a small amount

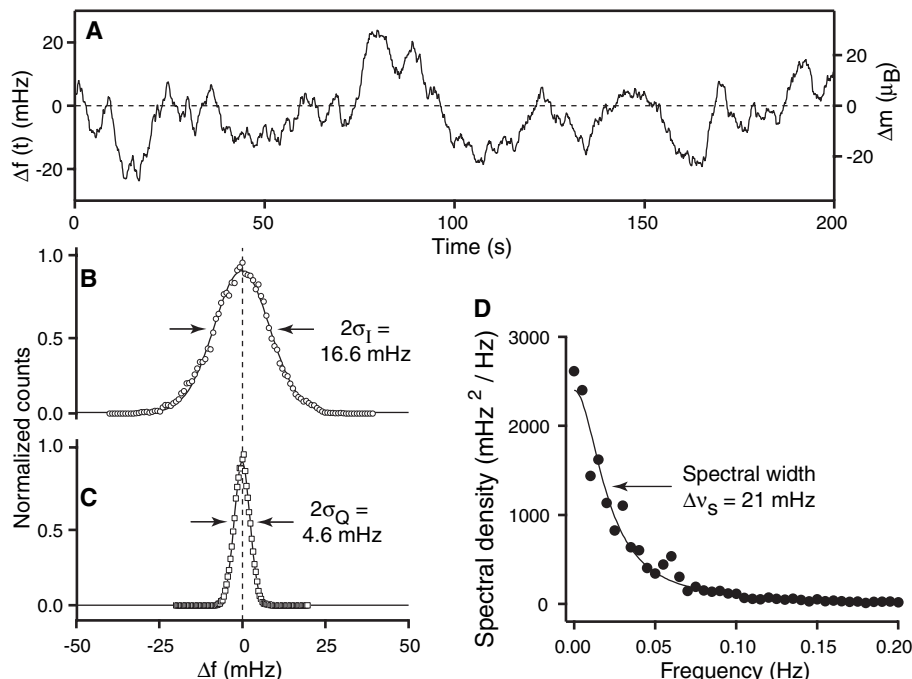$$\delta f_i = \frac{2 f_c G_i \mu_B}{\pi k x_{pk}} \alpha_i$$

Fig. 2. (A) Trace showing a time record of the statistical fluctuations recorded in a 83-mHz bandwidth with the use of setup 1. The frequency shift is converted to equivalent number of spins (right-hand axis) by dividing Δf by the average frequency shift per spin ($|\overline{\delta f}| = 0.8$ mHz/spin). (B) Histogram of a 1-hour continuous record of the in-phase lock-in output signal. The Gaussian distributed spin fluctuations have a zero mean, indicating that the time-averaged spin imbalance does not point in a preferred direction with respect to the effective field. This observation is consistent with the fact that the spin temperature in the rotating frame approaches $T_s = \infty$ for measurement times $t_{meas} \gg \tau_m$. (C) Histogram of the quadrature channel showing the detection noise. (D) Power spectrum of a 1-hour record of the fluctuations.

Fig. 3. (A) Trace showing the average of 2800 individual capture-store-readout sequences with a storage time of 1.0 s, taken with use of setup 2. The average frequency shift, $\overline{\Delta f}(t)$, and stored magnetization, $\overline{m}_{stored}$, are shown on the left- and right-hand axes, respectively. Equivalent spins are calculated by using $|\overline{\delta f}| =$ 1.7 mHz/spin. (B) Data taken under the same conditions as (A), except the storage time was increased to 5.0 s. The decaying magnetization observed during readout in (A) and (B) fits well to an exponential indicating a $\tau_m = 5.0$ s spin relaxation time during measurement.
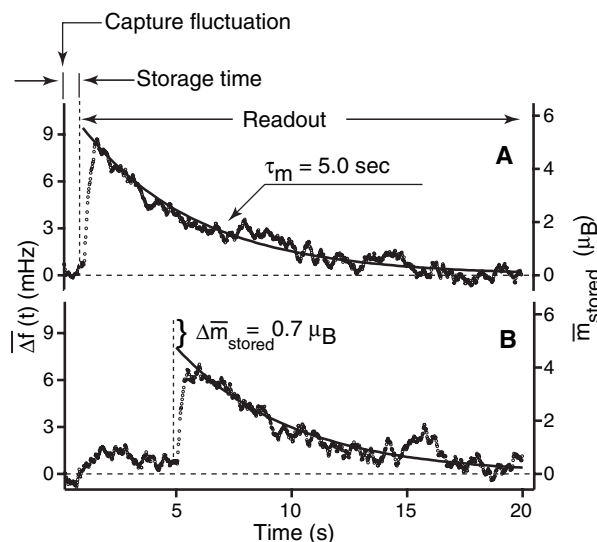
where G_i is the gradient at the position of the ith spin and α_i is a random variable that takes values $+1$ or -1, depending on whether the spin moment is aligned or anti-aligned with respect to the effective field in the rotating frame (5, 13, 14). The two-level nature of α_i reflects the quantum measurement characteristic of MRFM spin detection (i.e., a rotating frame Stern-Gerlach behavior) (15–17). For an ensemble of N spins, we define the instantaneous statistical spin imbalance in the rotating frame to be $\Delta N = \sum_{i=1}^{N} \alpha_i$ and the corresponding magnetic moment to be $\Delta m = \Delta N \mu_B$. The cantilever frequency shift for the ensemble is given by $\Delta f = \sum_{i=1}^{N} \delta f_i$.

Near the surface of the sample, the cantilever frequency is affected not only by the presence of the spins but also by the more dominant electrostatic and van der Waals forces. In order to make the spin component of the signal distinctive, we periodically reversed the sign of the frequency shift by interrupting the microwave power for 1/2 cycle of the cantilever vibration every N_{int} cycles (Fig. 1B). The periodic interruptions encode the spin signal with a characteristic frequency $f_{sig} = f_c / 2 N_{int}$. A lock-in amplifier referenced to f_{sig} is used to demodulate the frequency shift and determine Δf (5, 6).

A 200-s record of the cantilever frequency shift, recorded from the in-phase channel of the lock-in amplifier, is shown (Fig. 2A). A histogram of the frequency fluctuations (Fig. 2B) reveals a Gaussian shape with variance $\sigma_I^2 = 69$ mHz^2. We note that the distribution has a zero mean, indicating that the spin ensemble does not have a preferred direction with respect to the effective field. To show that the measured frequency shift is dominated by the spin signal rather than measurement noise, we show the histogram of the measurement noise recorded from the quadrature channel of the lock-in amplifier ($\sigma_Q^2 = 5$ mHz^2) (Fig. 2C). The variance of the spin signal without measurement noise is simply related to the in-phase and quadrature variances by $\sigma_{spin}^2 = \sigma_I^2 - \sigma_Q^2$ (6). From the measured variance σ_{spin}^2 and a model of the field produced by the tip (18), we estimate the total number of spins contained within the resonant slice to be $N \approx 70$.

The power spectrum of the frequency fluctuations (Fig. 2D) fits well to a Lorentzian with spectral width $\Delta v_s = 21$ mHz, corresponding to a correlation time $\tau_m = 1/2\pi\Delta v_s = 7.6$ s. This long correlation time, closely related to the rotating frame longitudinal relaxation time, allows us to measure real-time fluctuations of the spin ensemble with a lock-in time constant of up to 3 s.
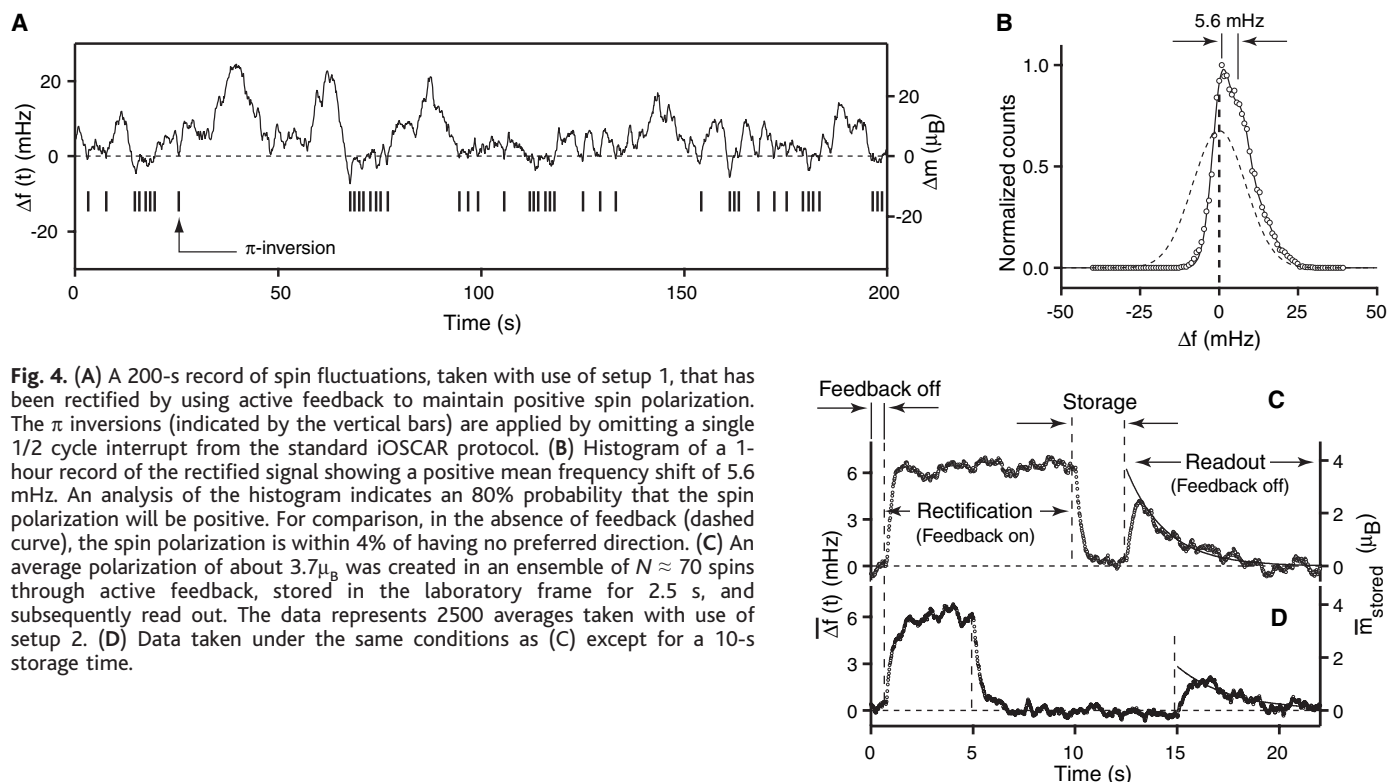
Fig. 4. (**A**) A 200-s record of spin fluctuations, taken with use of setup 1, that has been rectified by using active feedback to maintain positive spin polarization. The π inversions (indicated by the vertical bars) are applied by omitting a single 1/2 cycle interrupt from the standard iOSCAR protocol. (**B**) Histogram of a 1-hour record of the rectified signal showing a positive mean frequency shift of 5.6 mHz. An analysis of the histogram indicates an 80% probability that the spin polarization will be positive. For comparison, in the absence of feedback (dashed curve), the spin polarization is within 4% of having no preferred direction. (**C**) An average polarization of about $3.7\mu_B$ was created in an ensemble of $N \approx 70$ spins through active feedback, stored in the laboratory frame for 2.5 s, and subsequently read out. The data represents 2500 averages taken with use of setup 2. (**D**) Data taken under the same conditions as (C) except for a 10-s storage time.

As an initial demonstration of harnessing spin fluctuations, we created a hyperpolarized spin state by selectively capturing and storing the especially large statistical fluctuations. To do this, we continuously monitor the spin signal and wait until a fluctuation exceeds a predetermined threshold value $\Delta f_{\text{threshold}}$ (*19*). Upon registering a suitable fluctuation, the microwave power is turned off at a maximum of the cantilever motion, which leaves the instantaneous spin polarization pointing along $\mathbf{B}_0$. In the absence of the microwave field, the spins no longer respond to the cantilever motion, and the nonequilibrium state of the spin ensemble can be stored in the laboratory frame for as long as a spin-lattice relaxation time, T_1. The stored magnetization can then be read out by reapplying the microwave field at a maximum of the cantilever motion and using the standard interrupted OSCAR (iOSCAR) protocol.

The average of 2800 individual capture-store-readout sequences, taken with use of setup 2, is shown (Fig. 3). For the data in Fig. 3A, the captured magnetization was stored for 1 s in the laboratory frame (i.e., with the microwave field off) and then read out with use of the iOSCAR protocol. The readout signal had a peak amplitude of 9.4 mHz, which we estimate corresponds to an average magnetization of $\overline{m}_{\text{stored}} = 5.5\mu_B$. When the storage time was increased to 5 s (Fig. 3B), the peak stored magnetization decreased by 14% to $\overline{m}_{\text{stored}} = 4.8\mu_B$. This drop in $\overline{m}_{\text{stored}}$ is the result of depolarization due to longi-

tudinal relaxation, indicating $T_1 \sim 30$ s. The observed T_1 includes the contribution from the lattice as well as tip-induced relaxation (*11*).

In addition to simply selecting and capturing desired fluctuations, we can also take a more active approach by applying real-time feedback to the spin system in order to continuously guide its evolution. As a demonstration of feedback control, we have rectified the spin fluctuations by monitoring the spin signal and applying a π inversion to the entire spin ensemble whenever $\Delta f < 0$ (*19*). The π inversions, accomplished with the use of adiabatic inversion, flip the sign of the spin imbalance so as to always keep Δm positive in the iOSCAR reference frame. Figure 4A shows a 200-s record of the iOSCAR signal, taken with the use of setup 1, along with vertical bars indicating times when π inversions were applied. In contrast to Fig. 2B, the histogram of the signal with feedback control (Fig. 4B, solid curve) now shows a nonzero mean value of 5.6 mHz corresponding to $\sim 7.0\mu_B$. Thus, through the use of feedback, we have essentially hyperpolarized the spins in the rotating frame of the iOSCAR measurement. This spin order can once again be transferred to the laboratory frame, stored, and then read out (Fig. 4, C and D).

We have demonstrated real-time control of electron spins in small ensembles using two spin manipulation protocols: fluctuation capture and fluctuation rectification. Because the present single-shot detection

sensitivity is already approaching the single spin level, relatively modest improvements in detection signal-to-noise ratio should allow real-time quantum state detection and control of individual electron spins.

References and Notes

1. J. C. Maxwell, *Theory of Heat* (Longmans, London, ed. 6, 1880).
2. D. P. Divincenzo, *Science* **270**, 255 (1995).
3. B. E. Kane, *Nature* **393**, 133 (1998).
4. A. Steane, *Rep. Prog. Phys.* **61**, 117 (1998).
5. H. J. Mamin, R. Budakian, B. W. Chui, D. Rugar, *Phys. Rev. Lett.* **91**, 207604 (2003).
6. D. Rugar, R. Budakian, H. J. Mamin, B. W. Chui, *Nature* **430**, 329 (2004).
7. G. P. Berman, V. N. Gorshkov, D. Rugar, V. I. Tsifrinovich, *Phys. Rev. B* **68**, 094402 (2003).
8. B. W. Chui *et al.*, in *Technical Digest of the 12th International Conference on Solid-State Sensors and Actuators (Transducers '03)*, IEEE, Boston, MA, 8 to 12 June 2003 (IEEE, Piscataway, NJ, 2003), pp. 1120–1123.
9. D. Mozyrsky, I. Martin, D. Pelekhov, P. C. Hammel, *Appl. Phys. Lett.* **82**, 1278 (2003).
10. J. G. Castle, D. W. Feldman, P. G. Klemens, R. A. Weeks, *Phys. Rev.* **130**, 577 (1963).
11. B. C. Stipe *et al.*, *Phys. Rev. Lett.* **87**, 277602 (2001).
12. T. R. Albrecht, P. Grutter, D. Horne, D. Rugar, *J. Appl. Phys.* **69**, 668 (1991).
13. G. P. Berman, D. I. Kamenev, V. I. Tsifrinovich, *Phys. Rev. A* **66**, 023405 (2002).
14. C. P. Slichter, *Principles of Magnetic Resonance* (Springer-Verlag, Heidelberg, ed. 3, 1996).
15. G. P. Berman, F. Borgonovi, H. S. Goan, S. A. Gurvitz, V. I. Tsifrinovich, *Phys. Rev. B* **67**, 094425 (2003).
16. T. A. Brun, H. S. Goan, *Phys. Rev. A* **68**, 032301 (2003).
17. H. Gassmann, M. S. Choi, H. Yi, C. Bruder, *Phys. Rev. B* **69**, 115419 (2004).
18. For measurement setups 1 and 2, we estimate the average magnitude of the lateral gradient to be $\sim 1.7 \times 10^5$ T m^{-1}.

19. Materials and methods are available as supporting material on *Science* Online.
20. We thank J. Sidles, K. Holczer, and A. Hero for discussions and D. Pearson and M. Sherwood for technical assistance. This work was supported by the Defense Advanced Research Projects Agency Three-

Slip-Rate Measurements on the Karakorum Fault May Imply Secular Variations in Fault Motion

M.-L. Chevalier,[1,2] F. J. Ryerson,[2]* P. Tapponnier,[1] R. C. Finkel,[2] J. Van Der Woerd,[3] Li Haibing,[4] Liu Qing[5]

Beryllium-10 surface exposure dating of offset moraines on one branch of the Karakorum Fault west of the Gar basin yields a long-term (140- to 20-thousand-year) right-lateral slip rate of ~10.7 ± 0.7 millimeters per year. This rate is 10 times larger than that inferred from recent InSAR analyses (~1 ± 3 millimeters per year) that span ~8 years and sample all branches of the fault. The difference in slip-rate determinations suggests that large rate fluctuations may exist over centennial or millennial time scales. Such fluctuations would be consistent with mechanical coupling between the seismogenic, brittle-creep, and ductile shear sections of faults that reach deep into the crust.

The Karakorum Fault in Tibet is the main Quaternary right-lateral fault north of the Himalayas. Determining its past and present motion is critical to understanding the kinematics of Asian continental deformation and the rheology of the continental lithosphere (*1, 2*). The fault trends roughly parallel to the western Himalayan range, extending from at least Kailas to the Pamirs, a length of >1200 km (Fig. 1). Its Quaternary slip rate remains poorly constrained, compared to that of other large faults in Asia such as Kunlun, Haiyuan, and Altyn Tagh (*3–5*). Previous attempts to determine the rate have produced disparate values ranging from 1 to 30 mm/year (*2, 6–11*). Such disparities may result from the different techniques applied and time periods observed, the part of the fault investigated, or its complex geometry, which displays multiple splays with oblique slip (*12*). We present measurements of the Mid- to Late Pleistocene slip rate on the southern stretch of the fault, based on ^{10}Be surface exposure dating of two moraine crests displaced by the fault at the Manikala glacial valley terminus ($32°2.529'$N, $80°1.212'$E, 4365 to 4760 m above sea level) (Figs. 1 and 2).

[1]Laboratoire de Tectonique, Mécanique de la Lithosphère, Unité Mixte de Recherche (UMR) 7578, CNRS, Institut de Physique du Globe de Paris, 75252 Paris Cedex 05, France. [2]Insitute of Geophysics and Planetary Physics, Lawrence Livermore National Laboratory, Livermore, CA 94550, USA. [3]Institut de Physique du Globe de Strasbourg, UMR 7516, CNRS, Strasbourg, France. [4]Laboratory of Continental Dynamics, Institute of Geology, Chinese Academy of Geological Sciences, Beijing 100037, China. [5]Total Exploration China, Total-Fina-Elf, Beijing, 100004, China.

*To whom correspondence should be addressed. E-mail: ryerson@llnl.gov

The Manikala moraine complex lies at the base of the faulted Ayilari range front, which bounds the west side of the Gar valley, a large pull-apart basin floored by marshland that hides other strands of the Karakorum Fault system (*13*) (Fig. 1). The moraines, M1 and M2, lie southeast of the U-shaped Manikala Valley, a glacial trough deeply entrenched into the range's igneous basement (Fig. 2 and fig. S1). The range front is marked by triangular facets as high as 800 m that testify to a normal component of slip on the fault. The principal strand of the fault shows discrete right-lateral offsets (10 ± 2 m, 35 ± 5 m, and 75 ± 5 m) of young rills of different depths, incised into postglacial colluvium (fig. S1). Within the till complex, two main groups of moraines are recognized (Fig. 2 and fig. S2). All were emplaced by the Manikala Daer glacier, whose terminus is today ~7 km upstream. The morphology of the moraines indicates that they correspond to major advances of the glacier and were later abandoned when the glacier retreated upstream (fig. S3).

The relative ages of the moraine groups can be qualitatively assessed from their surface characteristics (Fig. 2 and fig. S2). The M1 surface is rough and composed of chaotically distributed, imbricate blocks (as large as 3 m in diameter) surrounded by coarse debris. The smoother surface of M2 appears older, with blocks (tens of centimeters to a meter in diameter) protruding above a mantle of smaller debris (Fig. 2 and fig. S2). The morainic ridges thus appear to become younger from east to west, consistent with right-lateral motion on the fault. The M2 moraine complex is divided into eastern and western sections (M2E and

M2W, respectively) by a deep, beheaded, flat-floored paleovalley that is truncated by the fault and flanked by well-defined lateral moraines (Fig. 2). The crest of the lateral moraine east of the paleovalley is well preserved, and its eastern edge extends to the base of the faceted range front. There is no catchment on the mountain slope facing this valley, indicating that it must correspond to a former channel of the Manikala glacier (Fig. 2 and fig. S3). The youngest moraine group, M1 (Fig. 2), is the only one present on both sides of the Manikala outwash valley and displays well-preserved terminal lobes and sharply defined ridge crests.

Upstream from the fault, the limits of glacial incision reach the base of the triangular facets that border the Manikala valley. Downstream, the M1 and M2E moraine ridge crests extend linearly to the fault and, when realigned with the sharp edge of glacial bedrock incision south of the fault, provide the only piercing points accurate enough to obtain offset estimates (*14*) (Fig. 2 and fig. S4). Once restored from satellite images, the M1 and M2E offsets are 220 ± 10 m and 1520 ± 50 m, respectively. Another moraine complex with morphologically similar surfaces and offsets is found at the terminus of the Tajiang Daer glacial valley ~10 km to the west (fig. S3), lending additional support to this reconstruction (fig. S4).

^{10}Be model ages for samples collected along the moraine ridge crests (Fig. 2B) define consistent age clusters that can be used to date their abandonment (*15*). Ages on the two M2 ridges (Fig. 3) fall mostly between 103 and 204 thousand years (ky) (15 samples; mean age, 152 ± 28 ky), with a subset of seven samples between 132 and 150 ky old (mean age, 140 ± 5.5 ky). Samples WG-3, WG-4, and WG-7, on the eastern moraine (M2E), are more than 55 ky older than the main M2E population (132 to 150 ky old). We consider these three samples to be outliers, probably originating from more ancient till upstream. Examination of the M2 population with the outliers excluded reveals two distinct subgroups: a younger cluster of nine samples with ages of 103 to 149 ky (mean age, 133 ± 15 ky) and an older group of six samples of 160 to 204 ky (mean age, 181 ± 14 ky). The nine samples from the M1 moraine yield a younger mean age of 35 ± 9 ky. Seven samples fall between 36 and 45 ky (mean age, 40 ± 3 ky), and two distinctly younger samples have ages of 21 ± 1.0 ky.

Suppression of Spin Diffusion near a Micron-Size Ferromagnet

R. Budakian, H. J. Mamin, and D. Rugar

IBM Research Division, Almaden Research Center, 650 Harry Road, San Jose, California 95120-6099, USA

We have used the large gradients generated near the ferromagnetic tip of a magnetic resonance force microscope to locally suppress spin diffusion in a silica sample containing paramagnetic electron spins. By controlling the slice location with respect to the tip, the magnetic field gradient was varied from 0.01 to 36 mT/μm, resulting in a fourfold decrease in T_1^{-1} and a similar decrease in $T_{1\rho}^{-1}$. The observed dependence of the relaxation rates on field gradient is consistent with the quenching of flip-flop interactions that mediate the transport of magnetization between slow and fast relaxing spins.

In recent years, numerous proposals have been made for solid-state devices that operate using the spin degree of freedom of electrons or nuclei [1–4]. The successful function of these spintronic and quantum computing devices depends critically on minimizing sources of spin relaxation and decoherence from the environment [5,6]. Long relaxation times are also essential for the detection and manipulation of single spins by magnetic resonance force microscopy (MRFM) [7].

Spin diffusion has long been recognized as a highly efficient mechanism for mediating spin relaxation. The concept was originally proposed by Bloembergen to account for the anomalously fast nuclear spin-lattice relaxation observed in CaF$_2$ and other ionic insulating crystals [8]. According to Bloembergen, fluctuating fields generated by paramagnetic impurities rapidly relax nearby nuclear spins. Dipolar coupling between adjacent nuclear spins gives rise to flip-flop interactions that mediate the transport of magnetization from the bulk to the paramagnetic sinks, greatly reducing the overall T_1. Waugh and his colleagues showed that the effect of spin diffusion could be reversed and the nonequilibrium state of slow relaxing spins could be recovered by a suitable sequence of strong rf pulses which reverse the sign of the dipolar Hamiltonian [9].

A more direct route to controlling spin diffusion is to prevent flip-flop processes from taking place. The dipolar Hamiltonian contains the term $H_{ss} = -\mu_0\gamma^2\hbar^2(1 - 3\cos^2\theta)(S_1^+ S_2^- + S_1^- S_2^+)/16\pi r^3$ which permits two like spins separated by **r** to exchange magnetization while conserving the total Zeeman energy. A sufficiently intense magnetic field gradient could be used to prevent simultaneous flips from occurring if the difference in Zeeman energies of two adjacent spins could be made larger than their dipolar coupling. If we consider a homogeneous solid like CaF$_2$, for example, we find that the gradient required to suppress flip-flops between two F nuclei is $G \sim \mu_0\gamma\hbar/4\pi r^4 \simeq 4 \times 10^2$ mT/μm, which is orders of magnitude larger than the largest gradients used in conventional magnetic resonance experiments [10].

While such large gradients are difficult to generate in the laboratory, there are instances where they occur naturally on the atomic scale [8,11]. For instance, the same paramagnetic impurities that drive macroscopic spin diffusion in solids are surrounded by microscopic regions or "frozen cores" where nuclear spin diffusion is quenched due to the large field gradient from the impurity [12,13].

Spin measurement using MRFM relies on large field gradients generated near a micron-size ferromagnet (the MRFM tip) in order to detect small ensembles of spins with high sensitivity and nanometer-scale spatial resolution [14–16]. In the present work, we exploit these intense gradients to investigate the spin-lattice relaxation of a dilute concentration of paramagnetic electron spins as a function of the field gradient near an MRFM probe tip. We show that by controlling the relative tip position, we can locally suppress spin diffusion and thereby affect spin-lattice relaxation rates.

The MRFM apparatus, shown schematically in Fig. 1, was placed in an evacuated vessel and cooled to 4.2 K. The custom designed single-crystal silicon cantilever with dimensions 210 μm $\times$ 3.3 μm $\times$ 0.86 μm had a fundamental flexural frequency $f_c = 5.8$ kHz, a spring constant $k = 0.02$ N/m, and a Q of 90 000. Displacement of the cantilever was detected using an optical fiber
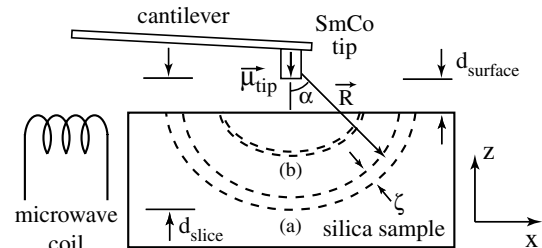

FIG. 1. Schematic of MRFM apparatus. Two slice locations are indicated for different values of the external field. Effective slice thickness (ζ) is calculated for $\Omega/2\pi = 20$ MHz. (a) $B_{ext} = 80$ mT, $d_{slice} = 4.3$ μm, $\zeta = 240$ nm. (b) $B_{ext} = 50$ mT, $d_{slice} = 2.5$ μm, $\zeta = 90$ nm.

interferometer coupled to a 1550 nm distributed feedback diode laser. The magnetic tip was fabricated by gluing a small, high anisotropy SmCo particle near the end of the cantilever in the presence of an external orienting field. After gluing, the bottom portion of the particle was milled flat using a focused ion beam. Magnetic characterization of the particle was carried out using cantilever magnetometry [17] which showed that the shaped ferromagnet with dimensions 6 μm $\times$ 7 μm $\times$ 11 μm had a total moment of $\mu_{tip} = 2.3 \times 10^{-10}$ J/T and was oriented to within 20° of the cantilever normal.

The sample consisted of optically polished vitreous silica (Corning 7943) that had been γ irradiated by a ^{60}Co source (150 Mrad) to produce paramagnetic defects or E' centers (unpaired electrons on Si) with a concentration of $n_S \sim 2 \times 10^{18}$ cm^{-3}. The spectrum of the E' centers was obtained at room temperature using a cw ESR spectrometer operating at 9.3 GHz. The spectrum, shown in Fig. 2, is inhomogeneously broadened and has the familiar powder line shape characteristic of a vitreous sample [18]. Prior to the MRFM measurements, the sample surface was coated with a 100 Å thick Ti/Au layer to minimize unwanted electrostatic tip-surface interactions.

Electron spins were excited at $\omega_{rf}/2\pi = 2.96$ GHz using a superconducting microstripline resonator coupled to a 200 μm diameter coil which generated a microwave field $B_1 = 0.16$ mT [19]. The spins contained within the resonant slice satisfy the magnetic resonance condition given by $\omega_{rf} = \gamma B_0(\mathbf{R})$, where γ is the gyromagnetic ratio ($\gamma/2\pi = 2.8 \times 10^{10}$ Hz/T) and $B_0(\mathbf{R})$ is the sum of the inhomogeneous field from the tip $B_{tip}(\mathbf{R})$ and a uniform external field B_{ext} produced by a superconducting magnet. At 2.96 GHz, the resonance condition for electrons is met when $B_0 = 106$ mT. By changing B_{ext}, both the location of the resonant slice with respect to the tip (d_{slice}) as well as the strength of the gradient within the slice can be varied. This makes it possible to study the dependence of T_1 on the strength of the field gradient.
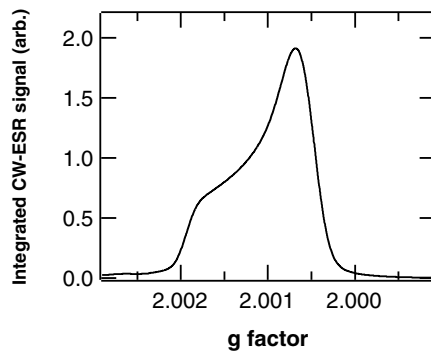

FIG. 2.   ESR spectrum of silica sample containing E' centers. The plot was obtained by integrating the derivative line shape measured using a cw ESR spectrometer.

We used a frequency modulated MRFM measurement protocol similar to that described by Wago *et al.* [20]. Prior to measurement, the microwave source was turned off and the spins were allowed to polarize in the static field $B_0(\mathbf{R})$ for a time long compared to T_1. To generate the MRFM signal, the microwave field was frequency modulated sinusoidally at the cantilever frequency with a peak frequency deviation of $\Omega/2\pi = 20$ MHz ($\Delta B_{mod} = \Omega/\gamma = 0.7$ mT), causing the spins within the slice of thickness $\zeta \simeq 2\Omega/\gamma G_{zz}$ to undergo cyclic adiabatic inversions, where $G_{zz} \equiv \partial B_z/\partial z$. In the presence of the axial field gradient of the magnetic particle G_{zz}, the oscillating magnetization creates a time dependent force that resonantly drives the cantilever from its equilibrium position. Hence, the peak vibration amplitude of the cantilever (the MRFM signal) is proportional to the number of polarized spins within the slice. For $B_{ext} = 50$ mT, where $G_{zz} = 15$ mT/μm and the slice is approximately 0.5 μm below the surface, the resonant slice contained roughly $N \sim 6 \times 10^3$ net polarized spins resulting in a peak detected force $F_{peak} = N\mu_B G_{zz} \simeq 8 \times 10^{-16}$ N.

To calibrate the gradient from the tip, the location of the resonant slice was measured as a function of external field [14]. For a given tip-to-surface distance $d_{surface}$ there is a corresponding external field $B_{ext} = B_{onset}$ below which the slice does not penetrate the surface and no signal is observed. The gradient is obtained by measuring the shift in the onset field B_{onset} at two different locations of the surface. We observed that when the surface was moved closer to the tip by $\Delta z = 340$ nm (from 2.50 to 2.16 μm) the onset field changed by $\Delta B_z = 4.9$ mT (from 45.8 to 40.9 mT). Thus, the average value of the axial gradient was $G_{zz} = \Delta B_z/\Delta z = 15$ mT/μm for $B_{ext} = 43.4$ mT. From the known geometry and the total moment of the magnetic particle, a model for $B_{tip}(\mathbf{R})$ was developed which was consistent with the measured gradient. This model was then used to calculate the gradient from the tip for an arbitrary value of B_{ext}.

The slice penetration depth $d = d_{slice} - d_{surface}$ was chosen so as to obtain a relatively uniform axial gradient within the slice volume, while having a detectable number of spins. If we assume a dipole distribution for the tip field, then the axial gradient is given by $G_{zz} = 3\mu_0\mu_{tip}(3\cos\alpha - 5\cos^3\alpha)/4\pi R^4$, where α is the angle made between the moment $\boldsymbol{\mu}_{tip}$ and the z axis and $\mathbf{R}$ is the distance from the center of the particle to the center of the slice (see Fig. 1). It is evident from this expression that the gradient within the slice is most uniform for small opening angles $\alpha_{max} \simeq \sqrt{d/R}$, hence small penetration depths. By making d small, however, both the slice volume as well as the signal decrease. For these measurements, we chose $d \simeq 0.5$ μm which gave a sufficiently high signal-to-noise ratio while maintaining reasonable gradient uniformity. For the largest gradients that were used, we estimate that the average gradient within the slice is within 15% of the peak value.

To obtain T_1, the spins were first allowed to polarize, then adiabatically inverted by briefly turning on the microwave field 20 MHz above resonance and sweeping the frequency to 20 MHz below resonance. The spins were then allowed to recover for a variable period of time and the polarization state was measured using the frequency modulated MRFM protocol. T_1 was determined by numerically fitting the data to the exponential recovery curves shown in Fig. 3. As can be seen in Fig. 4, T_1^{-1} has a roughly constant value of $T_1^{-1} = 0.16 \text{ s}^{-1}$ for gradients ranging between $0.01 < G_{zz} < 1 \text{ mT}/\mu\text{m}$. For $G_{zz} > 1 \text{ mT}/\mu\text{m}$, T_1^{-1} decreases monotonically with increasing gradient, reaching $T_1^{-1} = 0.04 \text{ s}^{-1}$ for $G_{zz} = 36 \text{ mT}/\mu\text{m}$.

In order to explain the observed dependence of T_1 on field gradient, we propose the following model. In a disordered sample, there can be a distribution of relaxation times resulting from local inhomogeneities in spin concentration (e.g., clusters [21]) or from variations in coupling strength between a paramagnetic electron and the host defect site [22]. If the spin temperature of the system is perturbed, as is the case when we adiabatically invert the spin population, faster relaxing spins rapidly relax to the lattice while the slower relaxing spins remain inverted. Thermal equilibrium within the inhomogeneously broadened spectrum is established via spin diffusion which carries Zeeman energy from slower to faster relaxing spins, thus reducing the overall T_1 of the entire ensemble [23–25]. If the field gradient from the magnetic particle is of sufficient strength to quench flip-flop interactions, spin diffusion will be suppressed and the overall relaxation rate will become slower.

If spin diffusion is the operative mechanism by which thermal equilibrium is established within the spin ensemble, then as the gradient is increased T_1^{-1} should begin to decrease when the difference in field between adjacent spins exceeds the homogeneous linewidth, i.e., $\overline{z}G_{zz} >$ ΔB_h, where $\overline{z} = \overline{r}/2$ is the average spacing between spins in the z direction. In our case, $\overline{r} = n_S^{-1/3} \simeq 8 \text{ nm}$ and $\Delta B_h \simeq 3.8\mu_0\gamma\hbar/4\pi\overline{r}^3 \simeq 1.4 \times 10^{-2} \text{ mT}$ is an estimate for the homogeneous linewidth for a dilute concentration of spins [26]. For our sample, the minimum gradient required to spectrally separate two overlapping spin packets is approximately $G_{zz} \approx 2.8 \text{ mT}/\mu\text{m}$, which is consistent with the observed onset gradient in Fig. 4.

For the case of an inhomogeneously broadened spectrum, the probability for two spins with different g values to exchange magnetization while conserving Zeeman energy is proportional to the normalized overlap function $\Phi(G_{zz})$ [26],

$$\Phi(G_{zz}) = \frac{\int f(B')f(B' - \overline{z}G_{zz})dB'}{\int f^2(B')dB'}, \qquad (1)$$

where $f(B)$ represents the shape of the inhomogeneous spectrum. The solid line in Fig. 4 is a plot of Eq. (1) calculated using the $f(B)$ shown in Fig. 2, which at 2.96 GHz has a width $\sim 0.1 \text{ mT}$. Excellent agreement with the measured data is obtained for $\overline{z} \simeq 5 \text{ nm}$. This value for $\overline{z}$ is in reasonable agreement with that estimated from the spin concentration ($\overline{z} \simeq 4 \text{ nm}$).

An estimate for the fraction of fast relaxing spins n_I/n_S needed to account for the observed decrease in T_1 in the presence of spin diffusion can be derived from the work of Vugmeister [25]. Within this model, the slow relaxing spins are coupled to the lattice only through cross relaxation with the fast relaxing spins. In the limit $\tau_{IL} \ll \tau_{IS}$, where τ_{IL} is the spin-lattice relaxation time for the fast relaxing spins and τ_{IS} is the cross-relaxation time between fast and slow relaxing spins,

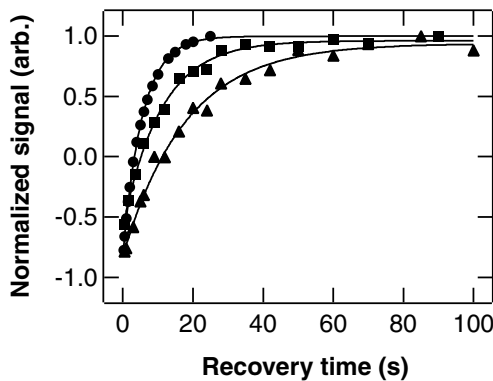$$\frac{n_I}{n_S} \simeq \frac{2\delta}{9T_1 n_S^2 \gamma^4 \hbar^2}. \qquad (2)$$

FIG. 3. Polarization as a function of recovery time for three different field gradients: ●, $G_{zz} \simeq 0.9 \text{ mT}/\mu\text{m}$, $T_1 = 5.6 \pm 0.1 \text{ s}$; ■, $G_{zz} \simeq 9 \text{ mT}/\mu\text{m}$, $T_1 = 11 \pm 0.5 \text{ s}$; ▲, $G_{zz} \simeq 27 \text{ mT}/\mu\text{m}$, $T_1 = 17.8 \pm 1.2 \text{ s}$. The lines show exponential recovery curves fit to the data.

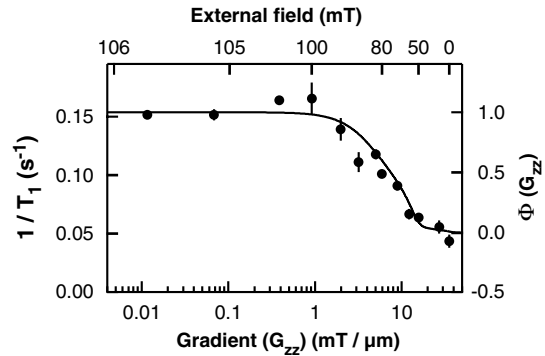FIG. 4. Spin-lattice relaxation rate T_1^{-1} versus gradient. The measured data (●) is plotted as a function of external field (top axis). Values for the tip gradient (bottom axis) for a given external field are calculated numerically using a model for the tip. The overlap function $\Phi(G_{zz})$ (solid curve) is calculated assuming an average axial separation $\overline{z} = 5 \text{ nm}$ between spins.
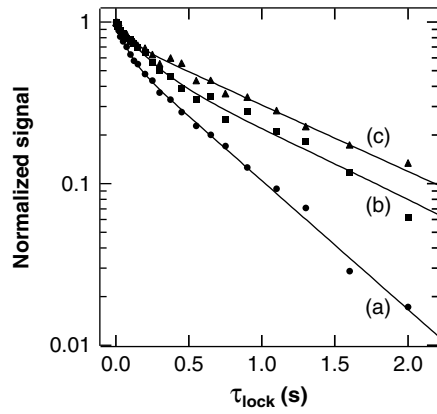
FIG. 5. Decay of magnetization in the rotating frame as a function of the spin-lock time τ_{lock}. The solid curves are double exponential fits to the data that serve as visual guides. (a) $G_{zz} \simeq 2$ mT$/\mu$m, $T_{1\rho} \simeq 0.33$ s. (b) $G_{zz} \simeq 6$ mT$/\mu$m, $T_{1\rho} \simeq 0.53$ s. (c) $G_{zz} \simeq 12$ mT$/\mu$m, $T_{1\rho} \simeq 0.80$ s.

If we take $\delta/\gamma \simeq 0.1$ mT for the width of the inhomogeneously broadened spectrum and $T_1 \simeq 6$ s for the relaxation time in the presence of spin diffusion, we find $n_I/n_S \sim 10^{-6}$. Thus, our results are consistent with a spin population where only a very small fraction of the total spins have fast intrinsic relaxation rates. When the spin diffusion process is suppressed, the slower intrinsic relaxation rate of the vast majority of spins is revealed.

Flip-flop interactions in the rotating frame can also give rise to spin diffusion and enhance the rotating frame spin-lattice relaxation rate $T_{1\rho}^{-1}$ [27]. In the presence of the field gradient from the tip, one might expect such interactions to be suppressed when the variation in the magnitude of the effective field $|\mathbf{B}_{\text{eff}}|$ between adjacent spins becomes comparable to the dipolar linewidth, where $\mathbf{B}_{\text{eff}} = B_1\hat{\mathbf{x}} + zG_{zz}\hat{\mathbf{z}}$ and z is the distance from the center of the resonant slice. For an average nearest neighbor spacing $\bar{z} = 5$ nm and a dipolar linewidth of $\Delta B_h \simeq 0.014$ mT, we would expect $T_{1\rho}^{-1}$ to be affected for $G_{zz} \gtrsim 13$ mT$/\mu$m.

To measure $T_{1\rho}$, the polarized spins within the resonant slice were first spin locked to the effective field $\mathbf{B}_{\text{eff}}$ by turning on the microwave field 20 MHz above resonance and then adiabatically sweeping the microwave frequency onto resonance. After waiting a variable time τ_{lock} with the microwave field turned on, the resulting magnetization was read out.

Figure 5 shows the magnetization as a function of spin-lock time τ_{lock}. The nonexponential decay curves can be characterized with two time constants. For $\tau_{\text{lock}} < 0.2$ s, the decay rate was found to be $\sim 2.5\times$ faster than for subsequent times. As the gradient from the tip was raised from 2 to 12 mT$/\mu$m, the time for the magnetiza-

tion to decay to e^{-1} of its initial value increased from 0.33 to 0.80 s.

In summary, we have used MRFM to investigate and control the spin-lattice relaxation rate of E' centers in SiO$_2$. We find that T_1^{-1} and $T_{1\rho}^{-1}$ are significantly reduced in the presence of large gradients that suppress the dipolar coupling between adjacent spins. The ability to quench spin-spin interactions by using large gradients is not only relevant for MRFM detection, but may also be of interest for the design of solid-state quantum devices.

[1] B. E. Kane, Nature (London) **393**, 133 (1998).
[2] D. P. DiVincenzo, Science **270**, 255 (1995).
[3] S. Lloyd, Science **261**, 1569 (1993).
[4] S. A. Wolf et al., Science **294**, 1488 (2001).
[5] S. Das Sarma et al., Solid State Commun. **119**, 207 (2001).
[6] G. Burkard, D. Loss, and D. DiVincenzo, Phys. Rev. B **59**, 2070 (1999).
[7] J. A. Sidles, Phys. Rev. Lett. **68**, 1124 (1992).
[8] N. Bloembergen, Physica (Utrecht) **15**, 386 (1949).
[9] W.-K. Rhim, A. Pines, and J. S. Waugh, Phys. Rev. B **3**, 684 (1971).
[10] W. Zhang and D. Cory, Phys. Rev. Lett. **80**, 1324 (1998).
[11] A. Andrieux, D. Jerome, and K. Bechgaard, J. Phys. Lett. (Paris) **42**, L87 (1981).
[12] D. Tse and I. Lowe, Phys. Rev. **166**, 292 (1968).
[13] W. Blumberg, Phys. Rev. **119**, 79 (1960).
[14] B. C. Stipe et al., Phys. Rev. Lett. **87**, 277602 (2001).
[15] Z. Zhang, P. C. Hammel, and P. E. Wigen, Appl. Phys. Lett. **68**, 2005 (1996).
[16] K. J. Bruland et al., J. Appl. Phys. **83**, 3972 (1998).
[17] B. C. Stipe et al., Phys. Rev. Lett. **86**, 2874 (2001).
[18] R. A. Weeks and C. M. Nelson, J. Appl. Phys. **31**, 1555 (1960).
[19] H. Mamin, R. Budakian, and D. Rugar, Rev. Sci. Instrum. **74**, 2749 (2003).
[20] K. Wago et al., Phys. Rev. B **57**, 1108 (1998).
[21] R. W. Warren, D. W. Feldman, and J. G. Castle, Phys. Rev. **136**, A1347 (1964).
[22] J. G. Castle and D. W. Feldman, J. Appl. Phys. **36**, 124 (1965).
[23] A. Kiel, Phys. Rev. **125**, 1451 (1962).
[24] N. Bloembergen et al., Phys. Rev. **114**, 445 (1959).
[25] B. E. Vugmeister, Phys. Status Solidi B **90**, 711 (1978); see especially Eqs. (17b) and (29).
[26] A. Abragam, The Principles of Nuclear Magnetism (Oxford University, London, 1961), pp. 128, 155.
[27] I. J. Lowe and D. Tse, Phys. Rev. **166**, 279 (1968).

Near optimal signal detection for finite state Markov signals with application to magnetic resonance force microscopy

Michael Ting*, *Student Member, IEEE,* Alfred O. Hero, *Fellow, IEEE,* Daniel Rugar[†], *Member, IEEE,* Chun-yu Yip, *Student Member, IEEE,* and Jeffrey A. Fessler, *Senior Member, IEEE*

Abstract— **Detection of a finite state Markov signal in additive white Gaussian noise (AWGN) can be done in an intuitive manner by applying an appropriate filter and using an energy detector. One might not expect this heuristic approach to signal detection to be optimal. However, in this paper, we show that for a certain type of finite state Markov signal, namely the discrete-time (d-t) random telegraph, this filtered energy detector is approximately optimal under the following conditions of: symmetric transition probabilities, low signal-to-noise ratio (SNR), long observation time, and small probability of transition between two consecutive time instances. When these last three conditions hold, but the transition probabilities are not symmetric, we show that a variant of the filtered energy detector is approximately optimal. It is also shown, under low SNR conditions, that the Likelihood Ratio Test for a d-t finite state Markov signal in AWGN reduces to the matched filter statistic with the Minimum Mean-Squared Error predictor used in place of the "known" signal values. This estimator-correlator receiver structure is well known in signal processing literature. This work is relevant to magnetic resonance force microscopy, an emerging technology that uses ultrasensitive force sensing to detect magnetic resonance. Sensitivity down to the single spin level was demonstrated in a recent experiment.**

I. INTRODUCTION

Detection of a discrete-time (d-t) finite state Markov signal in additive white Gaussian noise (AWGN) is widespread in many different fields. Detection of a random telegraph signal is used in the study of particle tunnelling [1], and in the study of low-frequency noise characteristics of light-emitting diodes [2]. In [3], statistical network anomaly detection based on Markov chains is presented, and in [4], land mine detection. The focus application of this paper is magnetic resonance force microscopy (MRFM), which is a promising technique for three-dimensional imaging on the nanometer scale. Recent experiments at IBM have shown that MRFM is capable of detecting and localizing individual electron spins associated with sub-surface atomic defects in silicon dioxide [5]. This single-spin detection milestone represents a factor of 10^7 improvement over conventional electron spin resonance detection and

was achieved using energy detection methods similar to those described in this paper. Other recent MRFM experiments have demonstrated the ability to detect and manipulate naturally occurring statistical fluctuations in small spin ensembles [6]. With further development, single-spin MRFM may eventually lead to atomic-resolution magnetic resonance imaging and find application in quantum computing experiments [7].

There are two main results of this paper. Firstly, when used to detect the d-t random telegraph in AWGN, the filtered energy (f-e) detector is approximately optimal under the following four conditions: symmetric transition probabilities, low signal-to-noise ratio (SNR), long observation time, and a small probability of transition between two consecutive instances. The f-e detector is no longer approximately optimal when the transition probabilities are asymmetric. We extend the f-e detector to a hybrid second-order detector which combines the filtered energy, amplitude, and energy statistics. It is shown that the hybrid detector is approximately optimal for the d-t random telegraph model under only the last three conditions. The second result of this paper is a new interpretation of the optimal Likelihood Ratio Test (LRT) for a d-t finite state Markov signal under low SNR conditions. It is shown that, under low SNR, the LRT reduces to the matched filter statistic with the Minimum Mean-Squared Error (MMSE) predictor used in place of the "known" values. Current single spin experiments operate under conditions of very low SNR; consequently, we are interested in the performance of detectors in the regime of low SNR and long observation time. Our results are therefore applicable to [1], [2], [3], [4] under conditions of low SNR.

Equations for the recursive implementation of the LRT can be found in [8]. The recursive form of the LRT is used to derive the two reported results. The first result is intuitively pleasing: the idea of performing detection of a finite state Markov signal by filtering the noisy observations and applying an energy detector is one that comes naturally. Moreover, we present simulations that suggest the optimality of a similar approximation for the d-t random walk process. A similar simplification effect has been observed in the linear vs. nonlinear estimation of a noisy continuous-time (c-t) random telegraph process. See Remark 1 in [9]. The second result has a c-t analog: in c-t, the LRT for detecting a random signal in AWGN has the form of the matched filter statistic with the MMSE predictor used in place of the "known" signal. It is exact under all SNR conditions [10], [11]. In d-t, this estimator-

correlator receiver structure appears in the LRT of problems whose probability density functions (pdfs) have an exponential form [12]. In particular, it applies when wanting to detect a Gaussian signal in AWGN.

The outline of this paper is as follows. In Section II, we briefly review the basic principles of MRFM. This is followed by a discussion in Section III of two d-t signal models: the random telegraph and random walk models. In Section IV, we describe existing detectors that are commonly used, namely the amplitude and filtered energy detectors, and compare them to the optimal detectors. We derive a new interpretation of the LRT under low SNR conditions. As well, the f-e detector is extended to a hybrid version. Simulation results are presented in Section V.

II. Basic Principles of MRFM spin detection

MRFM experiments, in general, involve the measurement of magnetic force between a submicron-size magnetic tip and spins in a sample. The details of spin manipulation and signal detection depend on the exact MRFM protocol used. One particularly successful protocol is called OSCAR, which stands for OScillating Cantilever-driven Adiabatic Reversal [13], [14]. A variation of this protocol, "interrupted OSCAR", was used in recent single spin experiments [5].

A schematic diagram of an OSCAR-type MRFM experiment is shown in Fig. 1. As shown in the figure, a submicron ferromagnet is placed on the tip of a cantilever and positioned close to an unpaired electron spin contained within the sample. An applied radio-frequency (rf) field serves to induce magnetic resonance of the spin when the condition $B_0 = \omega_{RF}/\gamma$ is met. Here, B_0 is the magnitude of the magnetic field from the tip, plus any externally applied static field that may be present. Because the magnetic field emanating from the tip is highly inhomogeneous, magnetic resonance is confined spatially to a thin bowl-shaped region called the "resonant slice".
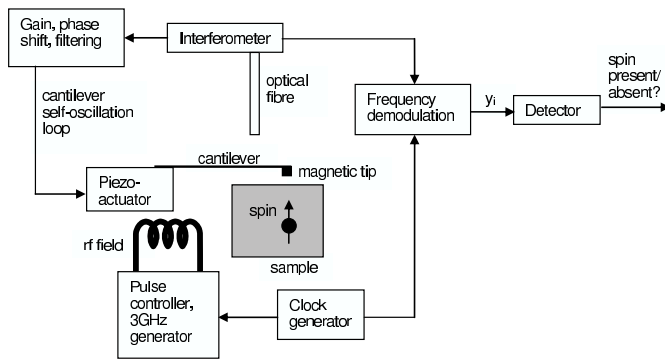

Fig. 1.   Schematic of the iOSCAR experiment.

In an OSCAR experiment, a gain-controlled positive feedback loop is used to oscillate the cantilever with a preset amplitude (typically 10-20 nm). The cantilever oscillation frequency is determined by the cantilever itself (specifically, by the fundamental flexural mode eigenfrequency), as well as by tip-sample interactions. As the tip of the cantilever vibrates, the resonant slice passes back and forth through the spin and,

as a result, the spin direction is cyclically inverted due to an effect called adiabatic rapid passage [13], [15], [16]. The cyclic inversion is synchronous with the cantilever motion and affects the cantilever dynamics by slightly shifting the cantilever resonance frequency. The frequency shift depends on the angle θ of the spin with respect to a vector called the "effective field in the rotating frame". See [14], [15] for further details. The frequency shift can be written as

$$\Delta\omega = \Delta\omega_{max} \cos\theta, \qquad (1)$$

where $\Delta\omega_{max} = 2\omega_0 G\mu/\pi k x_{pk}$ [14]. Here ω_0 is the unperturbed cantilever frequency, G is the field gradient from the tip, μ is the magnetic moment of the spin, k is the cantilever spring constant and x_{pk} is the peak amplitude of the cantilever vibration. The factor $\cos\theta$ represents the normalized projection of the spin in the direction of the effective field.

There are several impediments to single spin detection. Firstly, because the force from a single spin is so tiny (a few attonewtons), the maximum cantilever frequency shift is only about one part per million for typical experimental parameters. This small frequency shift must be detected in the presence of the cantilever phase (or frequency) noise that originates from cantilever thermal vibrations and sample-induced force fluctuations. The resulting low SNR necessitates long integration times for signal detection. Secondly, the detection is complicated by environmental disturbance to the spin (i.e., relaxation effects) that can randomly flip the spin orientation and reverse the signal polarity during the signal integration time. A low operating temperature, on the order of 1K, can help reduce both the cantilever thermal excitations and the random spin flip rate. Nevertheless, the signal processing methodology must take these effects into account.

We consider two models for the spin behaviour in the presence of environmental disturbances. In a quantum mechanical measurement model, the spin is always found to be either aligned or anti-aligned with the effective field, so that $\cos\theta = \pm 1$. Thus the frequency shift signal has only two levels: $\Delta\omega = \pm\Delta\omega_{max}$, and the time sequence of the frequency shift is a random telegraph signal with a transition rate that depends on the spin relaxation rate. In a classical measurement model (which we consider for the sake of completeness), $\cos\theta$ can take arbitrary values between +1 and -1. As a result of environmental disturbance, $\Delta\omega$ will be uniformly distributed between $-\Delta\omega_{max}$ and $+\Delta\omega_{max}$. For this case, a bounded random walk model is appropriate.

III. MRFM signal models

A. Model 1: Discrete-time Random Telegraph model

In the quantum measurement model, the frequency shift is characterized by random jumps between two discrete levels. The jumps are taken to be Poisson distributed. Denote the d-t random telegraph signal by ζ_i, where $t_i = iT_s$ are the sampling times, and T_s is the sampling time interval. In this paper, a Markovian process with a finite number of states will have a state space denoted by $\Psi = \{\psi_1, \ldots, \psi_r\}$, where r is the number of states. Let the state space of the d-t random telegraph be Ψ_{rt}; it has $r = 2$ states and we shall

take $\psi_1 = -A$, $\psi_2 = A$, where A is the amplitude of the random telegraph (A corresponds to $\Delta\omega_{\max}$ for the case of a MRFM signal). As an initial condition, ζ_0 is equally likely to be either $\pm A$. Then, a probability transition matrix $\mathbf{P}_{\mathrm{rt}}$ can be associated with ζ_i such that the (j,k)-th value of $\mathbf{P}_{\mathrm{rt}}$ equals $P(\zeta_i = \psi_k | \zeta_{i-1} = \psi_j)$ for $1 \le j,k \le 2$ and $i \ge 1$. Assume that $\mathbf{P}_{\mathrm{rt}}$ has the form:

$$\mathbf{P}_{\mathrm{rt}} = \begin{pmatrix} q & 1-q \\ 1-p & p \end{pmatrix}, \tag{2}$$

where $0 < p,q < 1$. If $p = q$, we say that the transition probabilities are *symmetric*, whereas if $p \ne q$, we shall say that they are *asymmetric*. Define the signal vector $\underline{\zeta} = [\zeta_0, \ldots, \zeta_{N-1}]^T$, the noise vector $\underline{w} = [w_0, \ldots, w_{N-1}]^T$, and the observation vector $\underline{y} = [y_0, \ldots, y_{N-1}]^T$, where the superscript $(\cdot)^T$ denotes the transpose operator. The w_i's are modelled as independent and identically distributed (i.i.d.) Gaussian random variables (r.v.s) with zero mean and variance σ^2. The detection problem is then to decide between:

$$\begin{aligned} H_0 \text{ (spin absent)} &: \quad \underline{y} = \underline{w} \\ H_1 \text{ (spin present)} &: \quad \underline{y} = \underline{\zeta} + \underline{w} \end{aligned} \tag{3}$$

Examples of noiseless and noisy random telegraph signals are given in Fig. 2. For the random telegraph signal, the SNR is defined to be $\mathrm{SNR} \triangleq A^2/\sigma^2$. The SNR in dB is defined in the usual way as $\mathrm{SNR}_{\mathrm{dB}} \triangleq 10 \log_{10} \mathrm{SNR}$.
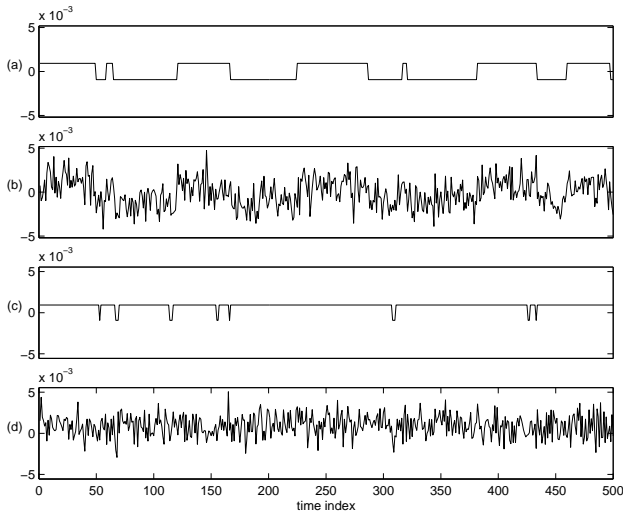

Fig. 2. a: Noiseless random telegraph signal with symmetric transition probabilities $p = q = 0.98$; b: Noisy version of (a) at SNR = -3 dB; c: Noiseless random telegraph signal with asymmetric transition probabilities $p = 0.98, q = 0.6$; d: Noisy version of (c) at SNR = -3 dB

B. Model 2: Discrete-time Random Walk model

In the classical spin detection model, the frequency shift signal is well approximated by a one dimensional random walk confined to the interval $I = [-A, A]$, where $A = \Delta\omega_{\max}$ for the case of a MRFM signal. We discretize I into $(2M + 1)$ states using a step size of s, where $M \in \mathbb{Z}$ and $M, s > 0$ and define ζ_i to be the random walk restricted to the discretized

I; we shall refer to this model as the d-t random walk model. The state space Ψ_{rw} of the d-t random walk will then have $r = 2M + 1$ states, where $\psi_j = (j - M - 1)s$ for $j = 1, \ldots, (2M + 1)$. Associate with ζ_i the probability transition matrix $\mathbf{P}_{\mathrm{rw}}$, so that, as before, the (j, k)-th element of $\mathbf{P}_{\mathrm{rw}}$ is $P(\zeta_i = \psi_k | \zeta_{i-1} = \psi_j)$ for $1 \le j, k \le (2M + 1)$ and $i \ge 1$. $\mathbf{P}_{\mathrm{rw}}$ is defined such that, at each time step, ζ_i changes by either $\pm s$. We assume reflecting boundary conditions, and ζ_0 is equally likely to be either $\pm s$. These conditions imply that $\mathbf{P}_{\mathrm{rw}}$ is a tridiagonal matrix.

The detection problem is now to test (3) when $\underline{\zeta}$ is modelled by a random walk. Note that the d-t random walk model can be regarded as a multi-state generalization of the d-t random telegraph model. In the limit as $s \to 0, M \to \infty$, the random walk converges to Brownian Motion over the interval I [17].

Examples of noiseless and noisy random walk signals are given in Figs. 3 and 4, where, at each state, a change of $\pm s$ is equally likely. Here, we shall define the SNR as $\mathrm{SNR} \triangleq (\lim_{i \to \infty} E[\zeta_i^2])/\sigma^2$, where ζ_i is the d-t random walk process. In other words, the SNR is the ratio of the steady-state expected energy of ζ_i to the noise variance. Note that this definition is consistent with that provided for the random telegraph signal. If ζ_i represented the d-t random telegraph signal, then $\zeta_i^2 = A^2$ at all time instances, leading to $\mathrm{SNR} = A^2/\sigma^2$.
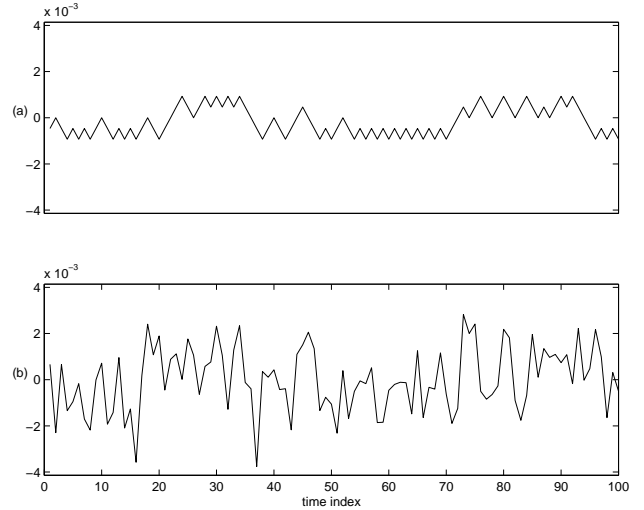
Fig. 3. a: Noiseless random walk signal with 5 levels; b: Noisy version of (a) at SNR = -7.3 dB

IV. DETECTION STRATEGIES

The detectors considered here can be placed into three categories: versions of existing detectors that are currently in use for MRFM; LRTs; and approximations to the LRT for the d-t random telegraph model. The LRT is a most powerful test that satisfies the Neyman-Pearson criterion: it maximizes the probability of detection (P_D) subject to a constraint on the probability of false alarm (P_F) [18], which is set by the user. Consequently, it can be used as a benchmark with which to compare the other detectors. When the random transition
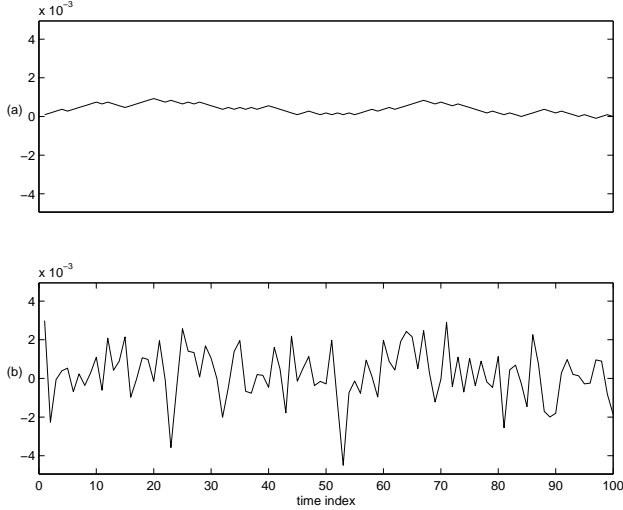
Fig. 4.   a: Noiseless random walk signal with 21 levels; b: Noisy version of (a) at SNR = -7.8 dB

times are known, the optimal LRT is the matched filter, called the omniscient matched filter (MF) in this paper. Although unimplementable, the MF detector provides an absolute upper bound when comparing the various detectors' Receiver Operating Characteristic (ROC) curves.

A. Amplitude, energy, filtered energy detectors

The d-t amplitude detector is

$$\left| \frac{1}{N} \sum_{i=0}^{N-1} y_i \right| \begin{array}{c} H_1 \\ \gtrless \\ H_0 \end{array} \eta \tag{4}$$

where η is set to satisfy the constraint on P_F. This is the optimal test under the assumption that y_i is the sum of an unknown constant and AWGN. This assumption would be true if there were no random spin flips. In this case, the amplitude detector is simply a MF detector. However, as the number of random transitions in y_i increases, the performance of the amplitude detector degrades. An alternative test statistic is the d-t signal energy, i.e. the sum of the squares of the y_i instead of the magnitude of the sum in (4). As the signal and noise are assumed to be independent, under hypothesis H_1, one would expect $\underline{y}$ to have a higher energy on average than under hypothesis $\bar{H}_0$. This can be reliably detected under a sufficiently high SNR. A natural improvement to the energy detector is to reject out-of-band noise by prefiltering $\underline{y}$ over the signal passband. As the signal ζ_i is baseband, a lowpass filter (LPF) is appropriate. In particular, one might use a simple first-order, single-pole filter given by

$$H_{\mathrm{LP}}(z) = \frac{1-\alpha}{2} \frac{1+z^{-1}}{1-\alpha z^{-1}} \tag{5}$$

where we require $|\alpha| < 1$ for stability [19]. The time constant α should be chosen based on the bandwidth of the signal; if ω_c is the desired -3dB bandwidth of the filter, one should set $\alpha = (1 - \sin \omega_c)/\cos \omega_c$. The -3dB bandwidth depends on the mean number of transitions, i.e. $(1 - p)/T_s$ for the

d-t random telegraph model. When the transition probabilities are symmetric, this figure corresponds to the mean number of transitions per second λ of the c-t random telegraph model. Given a value $p = q = p_0$, one can equate the expected number of transitions in both d-t and c-t models to obtain $\lambda = (1 - p_0)/T_s$. In practice, since the mean number of transitions is only approximately known to the experimenter, a bank of LPFs with different α's are used to perform detection [5]. The energy and filtered energy detector can then be expressed as

$$\sum_{i=0}^{N-1} (y_i * h_i)^2 \begin{array}{c} H_1 \\ \gtrless \\ H_0 \end{array} \eta \tag{6}$$

where "$*$" represents the convolution operator. For the energy detector, h_i is taken to be the unit impulse function $\delta[i]$, while for the filtered energy detector, $h_i = h_{\mathrm{LP}}[i]$, the impulse response of $H_{\mathrm{LP}}(z)$ in (5).

Note that the computational complexity for the amplitude, filtered energy, and energy detectors is $\mathcal{O}(N)$.

B. Optimal LRT detectors and their approximations

A recursive form of the LRT for a d-t finite state Markov signal in AWGN is derived in [8]. As well, it is possible to obtain a closed-form expression for the LRT: the LRT can be expressed as a product of matrices pre-multiplied by a row vector of the initial state probabilities and post-multiplied by a column vector of all ones [20]. Here, we focus on recursive implementations of the LRT for the d-t random telegraph and random walk process. See [8], [20] for more details.

Define $y^i \triangleq [y_0, \ldots, y_i]^T$ for $i \geq 0$. Let $E_0[\cdot]$ denote the expectation under the H_0 (spin absent) hypothesis, and $E_1[\cdot]$ the expectation under the H_1 (spin present) hypothesis. Consider first the d-t random telegraph model: define $R_i(u) \triangleq P(\zeta_i = u | y^{i-1})$, where $u \in \Psi_{\mathrm{rt}}$ and $i \geq 1$. There exists a recursive formula for $R_i(A)$ and $R_i(-A)$:

$$\begin{pmatrix} R_i(-A) \\ R_i(A) \end{pmatrix} = \mathbf{P}_{\mathrm{rt}}^T \begin{pmatrix} 1 - \natural \\ \natural \end{pmatrix} \quad \text{where}$$

$$\natural = \frac{e^{\frac{A}{\sigma^2} y_{i-1}} R_{i-1}(A)}{e^{\frac{A}{\sigma^2} y_{i-1}} R_{i-1}(A) + e^{-\frac{A}{\sigma^2} y_{i-1}} R_{i-1}(-A)} \tag{7}$$

for $i \geq 1$ and with initial conditions $R_0(A) = R_0(-A) = 1/2$. Let $f_1(\underline{y})$ be the pdf of $\underline{y}$ under hypothesis H_1 and $f_0(\underline{y})$ be the pdf of $\underline{y}$ under hypothesis H_0. The LRT is $\Lambda_{\mathrm{rt}}(\underline{y}) \triangleq f_1(\underline{y})/f_0(\underline{y})$. Define $\varphi(x; \mu, \sigma^2) \triangleq \exp[-(x - \mu)^2/2\sigma^2]/\sqrt{2\pi}\sigma$. Applying (7),

$$f_1(y^{N-1}) = f_1(y_{N-1}|y^{N-2}) \cdots f_1(y_1|y_0) f_1(y_0)$$
$$= \prod_{i=0}^{N-1} \left[R_i(A)\varphi(y_i; A, \sigma^2) + R_i(-A)\varphi(y_i; -A, \sigma^2) \right]$$

Using this, the LRT for the d-t random telegraph can be expressed as:

$$\Lambda_{\mathrm{rt}}(\underline{y}) = \prod_{i=0}^{N-1} \left[R_i(A) e^{\frac{A}{\sigma^2} y_i} + R_i(-A) e^{-\frac{A}{\sigma^2} y_i} \right] \begin{array}{c} H_1 \\ \gtrless \\ H_0 \end{array} \eta \tag{8}$$

Note that the running time of (8) is $\mathcal{O}(N)$, where N is the number of observations. Under low SNR conditions ($|A/\sigma| \ll 1$), the log LRT becomes

$$\log \Lambda_{\mathrm{rt}}(\underline{y}) \simeq \sum_{i=0}^{N-1} \log \left[R_i(A)(1 + \frac{A}{\sigma^2} y_i) + R_i(-A)(1 - \frac{A}{\sigma^2} y_i) \right]$$
$$= \sum_{i=0}^{N-1} \log \left[1 + \frac{1}{\sigma^2} y_i (A R_i(A) - A R_i(-A)) \right]$$

where we use the approximation $e^{\delta} \simeq 1 + \delta$ for small δ. Now, $A R_0(A) - A R_0(-A) = E_1[\zeta_0] = \hat{\zeta}_0$ and $A R_i(A) - A R_i(-A) = E_1[\zeta_i | y^{i-1}] = \hat{\zeta}_i$ for $i \geq 1$, i.e. it is the MMSE predictor of ζ_i given the past observations y^{i-1}.

$$\therefore \log \Lambda_{\mathrm{rt}}(\underline{y}) \simeq \sum_{i=0}^{N-1} \log \left(1 + \frac{1}{\sigma^2} y_i \hat{\zeta}_i \right) \simeq \frac{1}{\sigma^2} \sum_{i=0}^{N-1} y_i \hat{\zeta}_i \quad (9)$$

where the approximation $\log(1 + \delta) \simeq \delta$ for small δ was used. Under low SNR, the LRT is effectively correlating the observations y_i with the MMSE predictor of ζ_i. This is the matched filter statistic with the MMSE predictor substituted in place of the "known" values of ζ_i, and is known as the estimator-correlator detector. In particular, the estimator-correlator structure is known to be optimal for Gaussian signals in AWGN [12].

Under the regime of low SNR, long observation times ($N \gg 1$), and $p + q - 1 \simeq 1$ (the probability of transition between consecutive samples is small), the second-order expansion of $\log \Lambda_{\mathrm{rt}}(\underline{y})$ is approximately equal to the hybrid detector with the test statistic

$$\sum_i (y_i * h_{\mathrm{LP}}[i])^2 + \frac{1 - \alpha^2}{2\alpha} C_a \sum_i y_i + \frac{1 - \alpha^2}{2\alpha} C_e \sum_i y_i^2, \quad (10)$$

where the constants C_a, C_e are given in the appendix, and $\alpha = p + q - 1$. Therefore, in the aforementioned regime, one expects the hybrid detector to have performance similar to the optimal LRT. When $p = q$, the second-order expansion of the LRT is approximately equal to the filtered energy detector. See the appendix for more details. In light of the computational complexities for the filtered energy, energy, and amplitude detectors, the complexity of (10) is also $\mathcal{O}(N)$.

Next, consider the d-t random walk. Define the vectors:

$$\underline{R}_i \triangleq \begin{pmatrix} R_i(-Ms) \\ \vdots \\ R_i(0) \\ \vdots \\ R_i(Ms) \end{pmatrix}, \underline{W}_i \triangleq \begin{pmatrix} f_w(y_i + Ms) \\ \vdots \\ f_w(y_i) \\ \vdots \\ f_w(y_i - Ms) \end{pmatrix}$$

for $i \geq 0$. Here, $R_i(u) \triangleq P(\zeta_i = u | y^{i-1}), u \in \Psi_{\mathrm{rw}}$ and $f_w(\cdot) \triangleq \varphi(\cdot; 0, \sigma^2)$. If $\underline{a} = (a_1, \ldots, a_n)^T$ and $\underline{b} = (b_1, \ldots, b_n)^T$, define the operation $\underline{a} \odot \underline{b} \triangleq (a_1 b_1, \ldots, a_n b_n)^T$. There exists a recursive formula for $\underline{R}_i$ that is similar to that for the d-t random telegraph process, cf. (7):

$$\underline{R}_i = \mathbf{P}_{\mathrm{rw}}^T \frac{\underline{W}_{i-1} \odot \underline{R}_{i-1}}{\underline{W}_{i-1}^T \underline{R}_{i-1}} \quad (11)$$

for $i \geq 1$ and with the initial condition $\underline{R}_0 = \frac{1}{2}(\underline{e}_{M-1} + \underline{e}_{M+1})$, where $\{\underline{e}_i\}_{i=0}^{2M}$ are the standard basis vectors for $\mathbb{R}^{2M+1}$. The LRT for the d-t random walk can then be expressed as

$$\Lambda_{\mathrm{rw}}(\underline{y}) \triangleq \prod_{i=0}^{N-1} \frac{\underline{R}_i^T \underline{W}_i}{\underline{e}_M^T \underline{W}_i} \underset{H_0}{\overset{H_1}{\gtrless}} \eta \quad (12)$$

The running time of the LRT for the d-t random walk is $\mathcal{O}(MN)$, as $\mathbf{P}_{\mathrm{rw}}$ is a tridiagonal matrix. As with the d-t random telegraph model, an insightful understanding of $\Lambda_{\mathrm{rw}}(\underline{y})$ can be gained by considering the regime of low SNR. Following the same steps that were used to obtain (9):

$$\log \Lambda_{\mathrm{rw}}(\underline{y}) \simeq \sum_{i=0}^{N-1} \log \left[\sum_{j=1}^{r} R_i(\psi_j)(1 - \frac{1}{2\sigma^2} \psi_j^2 - \frac{1}{\sigma^2} y_i \psi_j) \right]$$
$$\simeq \frac{1}{\sigma^2} \sum_{i=0}^{N-1} y_i E_1[\zeta_i | y^{i-1}] - \frac{1}{2\sigma^2} \sum_{i=0}^{N-1} E_1[\zeta_i^2 | y^{i-1}] \quad (13)$$

We see that (13) is the matched filter statistic, but with the MMSE predictor of ζ_i and ζ_i^2 used instead of the "known" values. Since (11), (12), and (13) are independent of the structure of $\mathbf{P}_{\mathrm{rw}}$, this result applies to all finite state Markov processes under low SNR conditions. It is interesting to note that the c-t analog is given in [10], [11]. In the c-t case, however, the result is exact, while in the d-t case, we have shown the result approximately holds under low SNR conditions.

This result is consistent with the approximation that was earlier derived for the d-t random telegraph LRT in (9). Since $(-A)^2 = A^2$, $E_1[\zeta_i^2 | y^{i-1}] = A^2$ for the d-t random telegraph. So the second term in (13) will become a constant independent of the observations $\underline{y}$ and can be omitted.

V. SIMULATION RESULTS

The objective in this section is to compare the detection methods discussed in the previous section. The class of LRT detectors is optimal for their respective signal models, and provides a good comparison benchmark. Comparison of the various detectors is done using: (1) ROC curves, each of which is a plot of probability of detection (P_D) vs. probability of false alarm (P_F), and (2) power curves, each of which is a plot of P_D vs. SNR at a fixed P_F. Some of the parameters used in the simulation of the d-t random telegraph and random walk models are as follows: $k = 10^{-3}$ N m^{-1}, $\omega_0 = 2\pi \cdot 10^4$ rad s^{-1}, $B_1 = 0.2$ mT, $G = 2 \cdot 10^6$ T m^{-1}. The sampling period was $T_s = 1$ ms, and signal durations of $T = 60$ s and $T = 150$ s were used. The performance of the detectors varies as a function of T; in general, a larger T results in better performance. Values of T used in iOSCAR MRFM experiments are on the order of tens of hours [5]. Nevertheless, the comparative results obtained from using the two values of T above are representative of larger values. Indeed, our approximations to the optimal detectors improve with increased T.

A. Discrete-time random telegraph model

First, consider the d-t random telegraph. Fig. 5 depicts the simulated ROC curves at SNR = -35 dB, $\lambda = 0.5$ s^{-1}, and with symmetric transition probabilities ($p = q$). With $T_s = 1$ ms, this results in $p = q = 0.9995$. We examine the matched filter, d-t random telegraph LRT (RT-LRT), filtered energy, hybrid, amplitude, and unfiltered energy detectors. The RT-LRT, filtered energy, and hybrid detector curves are virtually identical, which is consistent with our analysis. The unfiltered energy and amplitude detectors have performance that is poorer than the RT-LRT, as it should be since the RT-LRT is the optimal detector. The unfiltered energy detector has the worst performance out of the five detector methods considered. Lastly, the omniscient MF detector has the best performance.

A power curve was generated over a range of SNRs under the same conditions as before with a fixed $P_F = 0.1$; it is illustrated in Fig. 6. For spin detection, an acceptable range for P_F is on the order of 0.05 to 0.1. The RT-LRT, filtered energy, and hybrid detector have similar performance from -30 dB to -45 dB. With this particular value of P_F and λ, the RT-LRT, filtered energy, and hybrid detector perform from 5 dB to 10 dB worse than the MF detector. Although the amplitude detector has worse performance than the RT-LRT and filtered energy detector, all three have comparable performance at -45 dB.
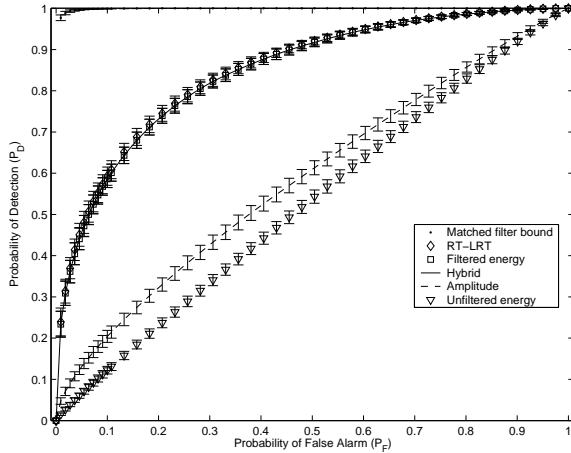

Fig. 5. Simulated ROC curves for the d-t random telegraph model with symmetric transition probabilities at SNR = -35 dB, $T = 60$ s, and $\lambda = 0.5$ s^{-1} for the omniscient matched filter, d-t random telegraph LRT (RT-LRT), filtered energy, hybrid, amplitude, and unfiltered energy detectors. The RT-LRT is theoretically optimal.

Fig. 7 shows the power curves generated using the bigger value of $T = 150$ s. Again, the RT-LRT, filtered energy, and hybrid detectors have the same performance from -30 dB to -45 dB. Note that the values of P_D have increased as compared to Fig. 6.

The ROC and power curve simulations were repeated with different values of λ, and the same relative performance was observed. In the interest of space, however, they will not be shown. Note that performance degrades as λ increases while T_s is held constant.
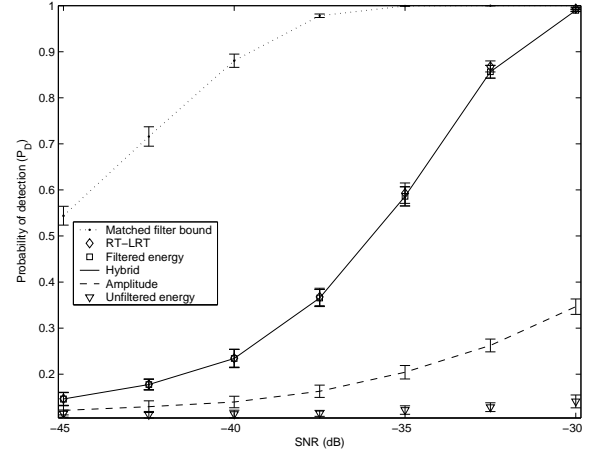

Fig. 6. Simulated power curves (P_D vs. SNR) for the d-t random telegraph model with P_F fixed at 0.1 and $\lambda = 0.5$ s^{-1}, $T = 60$ s. The RT-LRT is theoretically optimal.
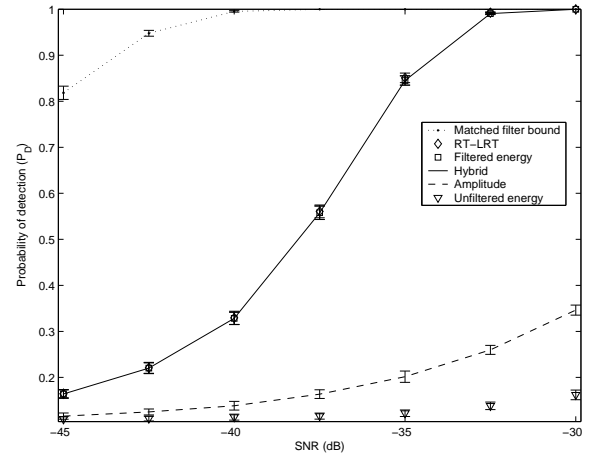

Fig. 7. Simulated power curves (P_D vs. SNR) for the d-t random telegraph model with P_F fixed at 0.1 and $\lambda = 0.5$ s^{-1}, $T = 150$ s. The RT-LRT is theoretically optimal.

In the second set of simulations, we investigate the case in which the transition probabilities are asymmetric, i.e. $p \neq q$. Consider the scenario where $p = 0.9998$, $q = 0.9992$, and all of the other parameters values are unchanged. The ROC curves for these parameter values are presented in Fig. 8. There are noticeable differences between the curves of the RT-LRT and filtered energy detectors. The hybrid detector's curve is slightly below that of the LRT, and it is better than that of the filtered energy detector. In fact, the filtered energy detector has worse performance than the amplitude detector. An asymmetry in p, q leads to a non-zero mean signal, which is probably why the amplitude detector's performance improves. Indeed, for the d-t random telegraph model, $\lim_{i \to \infty} E[\zeta_i] = A\frac{p-q}{2-p-q} = 0.6A$ for the values of p and q used here. Asymmetric transition probabilities can arise in some situations, e.g. the feedback-cooling-of-spins MRFM protocol proposed by Budakian [6].

Power curves from SNR = -55 dB to -35 dB were generated for the asymmetric case in Fig. 9. A larger value of T is
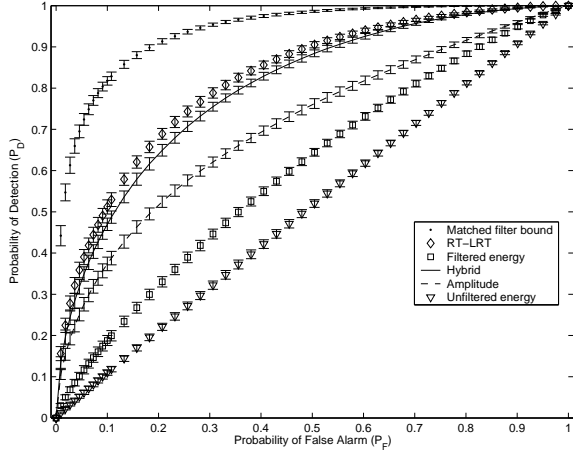
Fig. 8. Simulated ROC curves for the d-t random telegraph model with asymmetric transition probabilities ($p = 0.9998, q = 0.9992$) at SNR = -45 dB, $T = 150$ s. The RT-LRT is theoretically optimal.

required when $p \neq q$ for the hybrid detector to be a good approximation to the optimal LRT; hence, $T = 150$ s was used for simulations of the asymmetric random telegraph model. The hybrid detector has better performance than the amplitude and filtered energy detectors. It has performance that is comparable to the RT-LRT for lower SNR values.
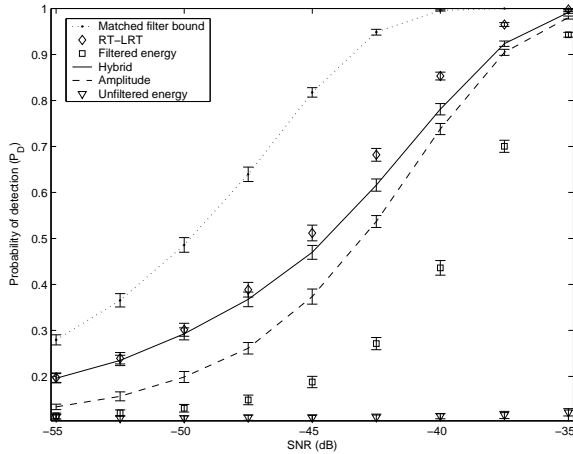

Fig. 9. Simulated power curves (P_D vs. SNR) for the d-t random telegraph model with P_F fixed at 0.1, $p = 0.9998, q = 0.9992$, and $T = 150$ s. The RT-LRT is theoretically optimal.

B. Discrete-time random walk model

Recall that for the d-t random walk model, $\mathbf{P}_{\mathrm{rw}}$ is tridiagonal. For the simulations, a particular subset of tridiagonal matrices was studied. Suppose for the moment that M is even. Recall that the random walk ζ_i is confined to the interval $[-Ms, Ms]$. Define the lower-quartile transition probabilities as $p_{l,1}, p_{l,2}$ and the upper-quartile transition probabilities as $p_{u,1}, p_{u,2}$. Let $\mathbf{P}_{\mathrm{rw}}^{(j,k)}$ be the (j,k)-th element of $\mathbf{P}_{\mathrm{rw}}$. Here, we examine the performance of the detectors assuming the following reflecting boundary conditions: $\mathbf{P}_{\mathrm{rw}}^{(1,2)} = 1, \mathbf{P}_{\mathrm{rw}}^{(1,i)} =$

0 for $i \neq 2$ and $\mathbf{P}_{\mathrm{rw}}^{(2M+1,2M)} = 1, \mathbf{P}_{\mathrm{rw}}^{(2M+1,i)} = 0$ for $i \neq 2M$. The rest of $\mathbf{P}_{\mathrm{rw}}$ is

$$\mathbf{P}_{\mathrm{rw}}^{(j,k)} = \begin{cases} p_{l,1} & 2 \leq j < M/2+1, k = j-1 \\ p_{l,2} & 2 \leq j < M/2+1, k = j+1 \\ 0.5 & M/2+1 \leq j \leq 3M/2+1, k = j \pm 1 \\ p_{u,1} & 3M/2+1 < j \leq 2M, k = j-1 \\ p_{u,2} & 3M/2+1 < j \leq 2M, k = j+1 \end{cases}$$

(14)

Let $\mathbf{A}_n(p_1, p_2)$ be a $n \times (n+2)$ matrix that looks like:

$$\mathbf{A}_n(p_1, p_2) = \begin{pmatrix} p_1 & 0 & p_2 & & & \\ & p_1 & 0 & p_2 & & \\ & & \ddots & \ddots & \ddots & \\ & & & p_1 & 0 & p_2 \end{pmatrix}$$

where the unspecified parts of the matrix are taken to be all zeros. In this section, the following subset of transition matrices for the d-t random walk was studied:

$$\mathbf{P}_{\mathrm{rw}} = \begin{pmatrix} 0 & & 1 & & \\ \mathbf{A}_{\frac{M}{2}-1}(p_{l,1}, p_{l,2}) & & & \\ & & \mathbf{F} & & \\ & & & \mathbf{A}_{\frac{M}{2}-1}(p_{u,1}, p_{u,2}) & \\ & & 1 & & 0 \end{pmatrix},$$

where $\mathbf{F} = \mathbf{A}_{M+1}(0.5, 0.5)$. Note that since each row of a probability transition matrix must sum to 1, one has $p_{l,1} + p_{l,2} = 1$ and $p_{u,1} + p_{u,2} = 1$.

In the case of M odd, the ranges for the indices j, k would change in an obvious way. When $p_{l,1} = p_{u,2} \iff p_{l,2} = p_{u,1}$, we say that the transition probabilities are *symmetric*, and if not, that they are *asymmetric*. The matched filter, d-t random walk LRT (RW-LRT), d-t random telegraph LRT (RT-LRT), filtered energy, amplitude, and unfiltered energy detectors are compared. In order to run the RT-LRT in the case of the symmetric d-t random walk, an average autocorrelation function of the random walk was empirically generated; then p was selected (and one used $q = p$) so that the autocorrelation function of the symmetric d-t random telegraph matched the empirical result. From this, the optimal α for the LPF of the filtered energy detector was also obtained.

The ROC curves for two symmetric cases are illustrated in Figs. 10 and 11. In the former, $p_{l,1} = p_{l,2} = p_{u,1} = p_{u,2} = 0.5$, while in the latter, $p_{l,1} = p_{u,2} = 0.52$ and $p_{l,2} = p_{u,1} = 0.48$. In both cases, the performance of the RW-LRT, RT-LRT, and filtered energy detector are all approximately the same, i.e. the latter two detectors are nearly optimal. When the transition probabilities of the d-t random walk are asymmetric however, as in the case of Fig. 12, the d-t random walk LRT is noticeably better than the filtered energy detector.

VI. CONCLUSION AND DISCUSSION

We have developed and compared optimal and non-optimal detectors under two single spin MRFM signal models. Recent experiments using the approximately optimal filtered energy detector have resulted in the successful detection of a single electron spin. This is strong evidence that the random telegraph signal model accurately describes the cantilever-single spin
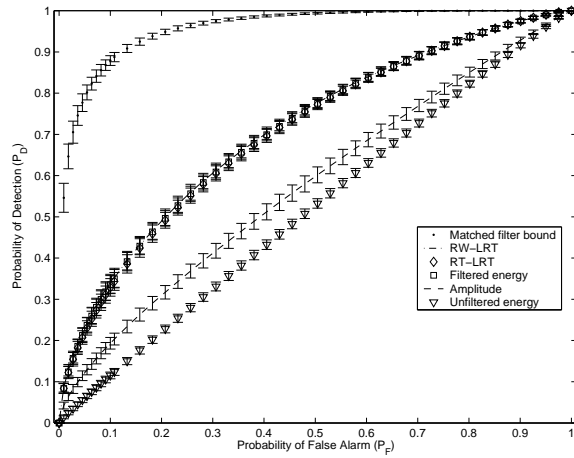
Fig. 10. Simulated ROC curves for the d-t symmetric random walk $p_{l,1} = p_{l,2} = p_{u,1} = p_{u,2} = 0.5$ at SNR = -39.9 dB, $T = 60$ s for the matched filter, RW-LRT, RT-LRT, filtered energy, amplitude, and unfiltered energy detector. The RW-LRT is theoretically optimal.
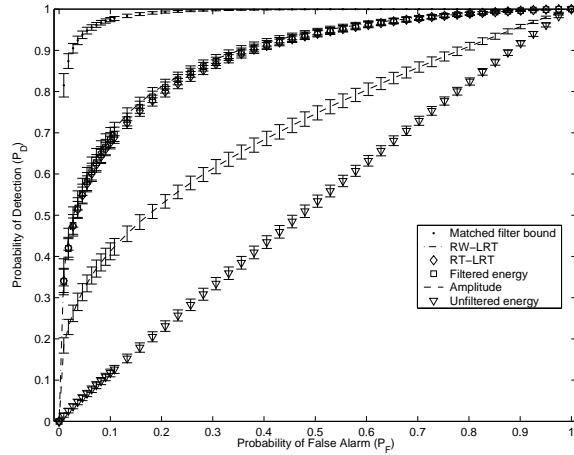

Fig. 12. Simulated ROC curves for the d-t asymmetric random walk $p_{l,1} = p_{u,1} = 0.45$, $p_{l,2} = p_{u,2} = 0.55$ at SNR = -41.0 dB, $T = 60$ s. The RW-LRT is theoretically optimal.

Fig. 11. Simulated ROC curves for the d-t symmetric random walk $p_{l,1} = p_{u,2} = 0.52, p_{l,2} = p_{u,1} = 0.48$ at SNR = -37.4 dB, $T = 60$ s. The RW-LRT is theoretically optimal.

interaction. Indeed, recent theoretical results have surfaced that rigorously justifies this model [21].

The results of this paper lend strong theoretical and practical support to the use of the simple filtered energy detector for the current MRFM single spin research community. It has been shown that the existing baseband filtered energy detector that is in current use is approximately optimal in the case of the symmetric d-t random telegraph model under the regime of low SNR, long observation times, and p close to 1. The last condition can be achieved by sampling at a sufficiently fast rate as compared to the rate of random transitions. This result has been extended to the case of the asymmetric d-t random telegraph by using a hybrid filtered energy/amplitude/energy detector. Simulations were presented showing that the near optimality of the baseband filtered energy detector extends to the case of the symmetric d-t random walk model. In the case of the asymmetric d-t random walk, the filtered energy detector does not perform as well as the optimal LRT. We expect that
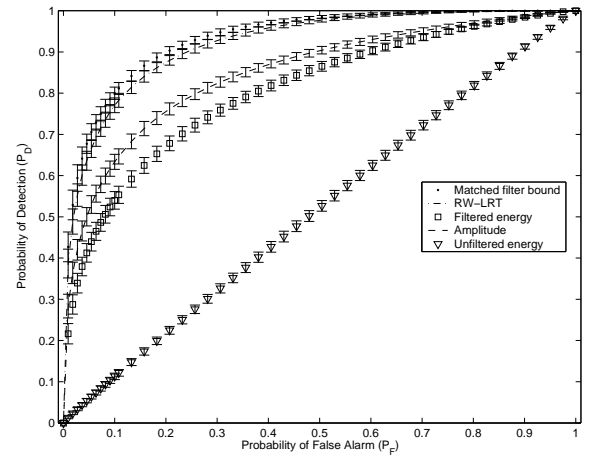
a hybrid detector along the lines of that formulated for the d-t random telegraph will perform close to the optimal for the asymmetric d-t random walk. Mathematical analysis of the d-t random walk model will be presented in a future paper.

A new interpretation of the LRT for a d-t finite state Markov signal in AWGN under low SNR conditions was presented. Specifically, the LRT is approximately the matched filter statistic with the MMSE predictor used in place of the "known" signal values.

REFERENCES

[1] K. Chun and N. O. Birge, "Dissipative quantum tunneling of a single defect in a disordered metal," *Physical Review B*, vol. 54, no. 7, pp. 4629–4637, 1996.
[2] L. J. Vandamme, A. V. Belyakov, M. Y. Perov, A. V. Yakimov, "Difference in dependence of 1/f and RTS noise on current in quantum dots light emitting diodes," in *Noise in Devices and Circuits*, ser. Proceedings of the SPIE, vol. 5113, 2003, pp. 368–378.
[3] S. Jha, K. Tan, R. A. Maxion, "Markov chains, classifiers, and intrusion detection," in *Proceedings of the 14th IEEE Computer Security Foundations Workshop*, 2001, pp. 206–219.
[4] P. D. Gader, M. Mystkowski, Y. Zhao, "Landmine Detection with Ground Penetrating Radar Using Hidden Markov Models," *IEEE Trans. Geosci. Remote Sensing*, vol. 39, no. 6, pp. 1231–1244, 2001.
[5] D. Rugar, R. Budakian, H. J. Mamin, B. W. Chui, "Single spin detection by magnetic resonance force microscopy," *Nature*, vol. 430, no. 6997, pp. 329–332, 2004.
[6] R. Budakian, H. J. Mamin, B. W. Chui, D. Rugar, "Creating Order from Random Fluctuations in Small Spin Ensembles," *Science*, vol. 307, no. 5708, pp. 408–411, 2005.
[7] G. P. Berman, G. D. Doolen, P. C. Hammel, V. I. Tsifrinovich, "Solid-state nuclear-spin quantum computer based on magnetic resonance force microscopy," *Physical Review B*, vol. 61, no. 21, pp. 14 694–14 699, 2000.
[8] L. L. Scharf and L. W. Nolte, "Likelihood Ratios for Sequential Hypothesis Testing on Markov Sequences," *IEEE Trans. Inform. Theory*, vol. IT-23, no. 1, pp. 101–109, 1977.
[9] Y.-C. Yao, "Estimation of Noisy Telegraph Processes: Nonlinear Filtering Versus Nonlinear Smoothing," *IEEE Trans. Inform. Theory*, vol. IT-31, no. 3, pp. 444–446, 1985.
[10] T. Kailath, "A General Likelihood-Ratio Formula for Random Signals in Gaussian Noise," *IEEE Trans. Inform. Theory*, vol. IT-15, no. 3, pp. 350–361, 1969.
[11] T. Kailath and M. Zakai, "Absolute continuity and Radon-Nikodym derivatives for certain measures relative to Wiener measure," *The Annals of Mathematical Statistics*, vol. 42, no. 1, pp. 130–140, 1971.

[12] S. C. Schwartz, "The Estimator-Correlator for Discrete-Time Problems," *IEEE Trans. Inform. Theory*, vol. IT-23, no. 1, pp. 93–100, 1977.

[13] B. C. Stipe, H. J. Mamin, C. S. Yannoni, T. D. Stowe, T. W. Kenny, D. Rugar, "Electron spin relaxation near a micron-size ferromagnet," *Physical Review Letters*, vol. 87, no. 27, pp. 277 602/1–4, 2001.

[14] H. J. Mamin, R. Budakian, B. W. Chui, D. Rugar, "Detection and manipulation of statistical polarization in small spin ensembles," *Physical Review Letters*, vol. 91, no. 20, pp. 207 604/1–4, 2003.

[15] C. P. Slichter, *Principles of Magnetic Resonance*, 3rd ed. Springer-Verlag, Berlin, 1989.

[16] K. Wago, D. Botkin, C. S. Yannoni, D. Rugar, "Force-detected electron-spin resonance: Adiabatic inversion, nutation, and spin echo," *Physical Review B*, vol. 57, no. 2, pp. 1108–1114, 1998.

[17] H. Stark and J. W. Woods, *Probability, Random Processes, and Estimation Theory for Engineers*, 2nd ed. Prentice-Hall, New Jersey, 1994.

[18] H. L. Van Trees, *Detection, Estimation, and Modulation Theory*. Wiley, New York, 1968, vol. 1.

[19] S. K. Mitra, *Digital Signal Processing: A Computer-Based Approach*, 2nd ed. McGraw-Hill, New York, 2001.

[20] M. Ting, "Analysis and comparison of detectors for several discrete-time Gauss-Markov signal models," University of Michigan, Tech. Rep., 2004.

[21] J. A. Sidles, 2004, private correspondence.

APPENDIX

Let $f(y_0, \ldots, y_{N-1})$ denote the log LRT function of the d-t random telegraph; this is obtained by taking the log of the left-hand side of (8). Let $g(y_0, \ldots, y_{N-1})$ be the filtered energy detector function in (6). Let us analyze the two functions f and g under the regime of low SNR ($|A/\sigma| \ll 1$) and long observation time ($N \gg 1$).

We want to obtain the approximate Taylor series expansion of f about $\underline{y} = \underline{0}$ and compare that with g. Define:

$$\theta_i \triangleq \frac{R_i(A) e^{\frac{A}{\sigma^2} y_i}}{R_i(A) e^{\frac{A}{\sigma^2} y_i} + R_i(-A) e^{-\frac{A}{\sigma^2} y_i}}$$

for $i \geq 0$. From (7), a recursive equation for θ_i can be derived. Its approximate solution is

$$\theta_i = \beta_i + \frac{qA}{\sigma^2} \sum_{j=0}^{i} \xi_{ij} y_j, i \geq 0 \text{ where}$$

$$\beta_i = \frac{1-q}{1-r} + \left(\frac{1}{2} - \frac{1-q}{1-r} \right) r^i, \ i \geq 0$$

$$\xi_{ij} = \frac{2(1-q)r^{i-j} + (2q-r-1)r^i}{1-r}, \ 0 \leq j \leq i-1$$

$$\xi_{ii} = \frac{2(1-q)}{1-r} + \frac{r^i(2q-r-1)}{1-r} = 2\beta_i, \ i \geq 0 \quad (15)$$

and $r = p + q - 1$. Note that $p, q \in (0,1) \Rightarrow |r| < 1$. Define $s_i \triangleq \frac{A}{\sigma^2} y_i$. Then,

$$f \simeq \sum_i \left\{ \left[s_i(2R_i(A) - 1) + \frac{1}{2} s_i^2 \right] \right.$$
$$\left. - \frac{1}{2} \left[s_i(2R_i(A) - 1) + \frac{1}{2} s_i^2 \right]^2 \right\} \quad (16)$$

By solving for $R_i(A)$ in terms of θ_i and using (15), one obtains

the approximate Taylor series expansion of f as

$$f \simeq L_1 + L_{2a} + L_{2b} + \text{h.o.t.}, \quad \text{with} \quad (17)$$

$$L_1 = \frac{A}{\sigma^2} C_m \sum_i (1 - r^i) y_i \quad (18)$$

$$L_{2a} = 2q \left(\frac{A}{\sigma^2} \right)^2 \sum_i \sum_{j=0}^{i-1} \left[\frac{2(1-q)}{1-r} r^{i-j} - r^i C_m \right] y_i y_j \quad (19)$$

$$L_{2b} = \left(\frac{A}{\sigma^2} \right)^2 \sum_i \left\{ 4r \left(\frac{1-q}{1-r} \right)^2 + 2 \frac{(q-r)(1-q)}{(1-r)^2} \right.$$
$$\left. - C_m(2q + C_m)r^i + \frac{1}{2} C_m^2 r^{2i} \right\} y_i^2 \quad (20)$$

$$C_m = \frac{p-q}{2-p-q}$$

In (17), "h.o.t." denotes the higher-order terms; specifically, terms of degree three of higher. C_m is a parameter that indicates the mismatch between the transition probabilities p and q. In the symmetric case, $p = q \Rightarrow C_m = 0$, and one obtains a simpler expression for f. Let f_{sym} be the function f under symmetric transition probabilities, i.e. $p = q$. Then,

$$f_{\text{sym}} \simeq 2p \left(\frac{A}{\sigma^2} \right)^2 \left\{ \sum_{i=1}^{N-1} \sum_{j=0}^{i-1} (2p-1)^{i-j} y_i y_j \right.$$
$$\left. + \sum_{i=0}^{N-1} \left(1 - \frac{1}{4p} \right) y_i^2 \right\} \quad (21)$$

For sufficiently large N, it can be shown that

$$g \simeq D \left\{ \sum_{i=1}^{N-1} \sum_{j=0}^{i-1} \alpha^{i-j} y_i y_j + \frac{\alpha}{1+\alpha} \sum_{i=0}^{N-1} y_i^2 \right\} \quad (22)$$

where $D = \frac{1-\alpha^2}{2\alpha}$ is a constant; note that D plays no role in the performance of the test statistic. Comparing (21) and (22), we see that they are nearly identical in form if $\alpha = 2p - 1$. If $\alpha = 2p - 1 \Rightarrow |f_{\text{sym}} - g| \simeq \frac{1}{4p} \sum_i y_i^2$. Now, $E_1[\sum_{i=0}^{N-1} y_i^2] - E_0[\sum_{i=0}^{N-1} y_i^2] = A^2 N$. On the other hand, for large N,

$$E_1 \left[\sum_{i=1}^{N-1} \sum_{j=0}^{i-1} \alpha^{i-j} y_i y_j \right] - E_0 \left[\sum_{i=1}^{N-1} \sum_{j=0}^{i-1} \alpha^{i-j} y_i y_j \right]$$
$$\simeq G A^2 N \quad (23)$$

where $G = \frac{\alpha(2p-1)}{1-\alpha(2p-1)}$. When $\alpha = 2p - 1$, $G = \frac{(2p-1)^2}{1-(2p-1)^2} = \frac{1}{4(1-p)} + \frac{1}{4p} - 1$. For p close to 1, $G \gg \frac{1}{4p}$, and $GA^2 N \gg \frac{1}{4p} A^2 N$. So to the first moment, the difference of $\frac{1}{4p} \sum_i y_i^2$ between f_{sym} and g does not represent a significant difference when $p \simeq 1$. Under these conditions, we expect that the performance of the filtered energy detector and the d-t random telegraph LRT to be similar.

It is possible to obtain an approximation to the d-t random telegraph LRT that holds when we make no assumption about p being equal to q. When $p \neq q$, $C_m \neq 0$, and there are terms of the form $r^i C_m$ and $r^{2i} C_m^2$ in (18)-(20). Since $|r| < 1$,

$r^i \to 0$ in the limit as $i \to \infty$. So drop these terms to get:

$$f \simeq C \left\{ \frac{(p-q)\sigma^2}{4q(1-r)A} \sum_i y_i + \sum_i \sum_{j<i} r^{i-j} y_i y_j \right.$$
$$\left. + \left[\frac{1}{2} + \frac{r(1-q)}{2q(1-r)} \right] \sum_i y_i^2 \right\} \qquad (24)$$

where $C = 4q \frac{1-q}{1-r} \left(\frac{A}{\sigma^2} \right)^2$ is a constant. Define $C_a \triangleq \frac{(p-q)\sigma^2}{4q(1-r)A}$ and $C_e \triangleq \frac{r(1-q)}{2q(1-r)}$. In order to equate the coefficients of the cross-terms $y_i y_j$ between (24) and g in (22), we require $\alpha = r = p + q - 1$. In g, the ratio of the energy terms to the cross-terms is $\frac{\alpha}{1+\alpha}$. For $r = \alpha \simeq 1 \Rightarrow \frac{\alpha}{1+\alpha} \simeq 1/2$. The idea is to add the energy and amplitude statistics to g so that all three statistics are in the same ratio as in (24). Let g_{hyb} be the "extended" version of g, which we shall call the hybrid filtered energy/amplitude/energy detector:

$$g_{\text{hyb}} \triangleq g + \frac{1-\alpha^2}{2\alpha} \left[C_a \sum_i y_i + C_e \sum_i y_i^2 \right]$$
$$= g + \frac{1-\alpha^2}{2\alpha} C_a \sum_i y_i + \frac{1-\alpha^2}{2\alpha} C_e \sum_i y_i^2 \qquad (25)$$

We expect g_{hyb} to have performance that is similar to f under the conditions of large N, low SNR, and $r \simeq 1$.

Magnetic resonance force microscopy of nuclear spins: Detection and manipulation of statistical polarization

H. J. Mamin, R. Budakian, B. W. Chui, and D. Rugar

IBM Research Division, Almaden Research Center, 650 Harry Road, San Jose, California 95120, USA

(Received 7 January 2005; published 5 July 2005)

We have detected and manipulated the naturally occurring $\sqrt{N}$ statistical polarization in nuclear spin ensembles using magnetic resonance force microscopy. Using protocols previously developed for detecting single electron spins, we have measured signals from ensembles of nuclear spins in a volume of roughly (150 nm)^3 with a sensitivity of roughly 2000 net spins in a 2.5 h averaging window. Three systems have been studied, ^{19}F nuclei in CaF$_2$, and ^{1}H nuclei (protons) in both polymethylmethacrylate and collagen, a naturally occurring protein. By detecting the statistical polarization, we not only can work with relatively small ensembles, but we eliminate any need to wait a longitudinal relaxation time T_1 to polarize the spins. We have also made use of the fact that the statistical polarization, which can be considered a form of spin noise, has a finite correlation time. A method similar to one previously proposed by Carlson *et al.* [Bull. Am. Phys. Soc. **44**, 541 (1999)] has been used to suppress the effect of the statistical uncertainty and extract meaningful information from time-averaged measurements. By implementing this method, we have successfully made nutation and transverse spin relaxation time measurements in CaF$_2$ at low temperatures.

I. INTRODUCTION

Magnetic resonance force microscopy (MRFM) combines ultrasensitive force detection with the principles of magnetic resonance to probe small volumes of electron and nuclear spins.[1–6] If the goal of single nuclear spin sensitivity can be reached, the technique may ultimately allow for three-dimensional molecular imaging with atomic resolution.[2] It might also function as a readout scheme for quantum computation.[7,8] While the technique is still far from achieving these challenging goals, steady progress has been made, as evidenced by the recent demonstration of detection of a single electron spin with a spatial resolution of 25 nm.[9]

The measurement protocols previously developed for small ensembles of electron spins did not require a mean spin polarization, but rather took advantage of the naturally occurring statistical polarization. For an ensemble of N spins, this polarization is of order $\sqrt{N}$, and can actually exceed the thermal (Boltzmann) polarization for small N. One of the purposes of the current work is to demonstrate that these protocols are applicable to detecting the statistical polarization of nuclear spins as well as electron spins. This approach is particularly valuable for nuclear spins, since the time required to polarize a nuclear spin ensemble can be exceedingly long at low temperatures. In this work, we verify the technique by studying ensembles of order $N = 10^8$ nuclear spins in a volume of roughly (150 nm),[3] where we detect and manipulate the statistical polarization of order $\sqrt{N} = 10^4$ net spins.

A second purpose of this work is to demonstrate a scheme to extract meaningful information in the presence of the spin noise[10–13] associated with the statistical polarization. It has recently been proposed that manipulation of such fluctuating statistical ensembles should be possible by making use of the finite correlation time of the fluctuations.[14,15] We have implemented a version of this scheme using MRFM, and have

performed spin manipulations on statistical ensembles of ^{19}F and ^{1}H nuclei. Despite the fact that the magnitude and even the sign of the polarization fluctuates over time, this approach has allowed us to perform nutations and transverse spin relaxation measurements.

II. EXPERIMENTAL DETAILS AND PROTOCOLS

Two species of nuclear spins were studied in three different samples. First, we studied ^{19}F in a polished single crystal of CaF$_2$ (99.99% pure).[16] We also studied protons in two different systems, the polymer polymethylmethacrylate (PMMA), and the triple-helix protein collagen. PMMA has previously been studied with MRFM using the Boltzmann polarization.[17] The collagen was chosen to demonstrate the applicability of MRFM to the study of biomolecules. The PMMA sample was a 200 nm thick film that was spun onto a silicon wafer and baked at 175 °C. It was then metal coated with 75 Å Cr/200 Å Au to reduce charging effects. The collagen sample was prepared from a commercially available solution of rat-tail collagen in acetic acid (Type 1, BD Biosciences). A small drop of the solution was placed onto a silica substrate and allowed to air dry. The sample was further dried in vacuum at room temperature for 4 days before use, but otherwise no special preparations were made. All three systems have expected spin densities in the range of $4–6 \times 10^{22}$ spins/cm^3.

As shown in Fig. 1 and described in Ref. 12, our MRFM technique uses a magnetic tip mounted on the end of a vertically oriented ultrasensitive cantilever. The tip generates a strong magnetic field gradient (∼1 G/nm). A rf field B_1 at frequency ω_{rf} is used to excite magnetic resonance within a thin resonant slice where the condition $B_0(x,y,z) = \omega_{rf}/\gamma$ is met. Here B_0 is due to the tip field plus an optional external field B_{ext}, and γ is the gyromagnetic ratio (4.2 kHz/G for
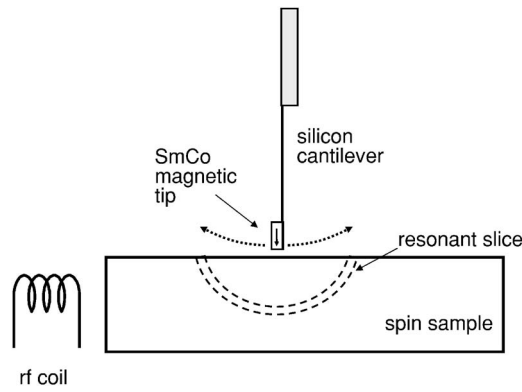
FIG. 1. Schematic of the MRFM experiment. Left-right statistical imbalance of the spin polarization within the resonant slice gives rise to forces on the magnetic tip.

protons and 4.0 kHz/G for ^{19}F). In the experiment on CaF_2, for example, the rf frequency was 50.8 MHz, so that the resonance condition was $B_0(x,y,z) = 12\,680$ G. The rf field $B_1 \sim 15$ G was generated using a 300 μm diameter coil that was part of an *LC* resonant circuit. The microscope was operated in a small vacuum chamber within the bore of a superconducting magnet. The temperature of the microscope with the rf coil energized was roughly 7 K.

The same single-crystal silicon cantilever was used for all three samples. It consisted of a roughly 100 nm thick, 90 μm long shaft, with a 1 μm × 10 μm × 4 μm silicon mass on the end to suppress the motion of the higher order modes.[18] The cantilever spring constant k was roughly 8.6×10^{-5} N/m. In zero magnetic field, the cantilever resonant frequency f_c was 3830, and the quality factor Q was roughly 60 000 at 4.2 K. A SmCo particle was attached to the end of the cantilever with its magnetic axis carefully oriented in a magnetic field to within 5° of the cantilever axis, and then shaped with a focused ion beam to submicron dimensions to reduce its total moment. This preparation was necessary to prevent excessive cantilever bending in the applied magnetic field. The tip of the particle was further shaped to a roughly 250 nm wide apex, resulting in field gradients in the range of 1 G/nm. In a field of 12 000 G, the cantilever frequency increased to about 4200 Hz due to field-induced restoring torque, and the Q was reduced to approximately 5000 due to various magnetic loss mechanisms.[19,20] This undesirable effect, while not a major problem, can be eliminated through the use of an alternative cantilever orientation.[21]

The spin-manipulation and detection scheme is based on the OSCAR protocol used previously for electron spins,[9,12,22] where OSCAR stands for oscillating cantilever-driven adiabatic reversals. The cantilever is self-oscillated at its natural resonant frequency using a positive feedback loop. As the cantilever position oscillates according to $x_c(t) = x_{pk}\cos(\omega_c t)$, the field B_0 at a given sample location is modulated because of the field gradient $G = \partial B_0/\partial x$ from the tip. In the language of magnetic resonance, the effective field $\mathbf{B}_{eff}$ in the rotating frame is given by[12,23]

$$\mathbf{B}_{\text{eff}} = B_1\hat{\mathbf{x}} + Gx_c(t)\hat{\mathbf{z}}. \tag{1}$$

For $Gx_{pk} \gg B_1$, $\mathbf{B}_{eff}$ will change from the $+\hat{z}$ to $-\hat{z}$ direction as the cantilever oscillates. As long as the adiabatic condition is
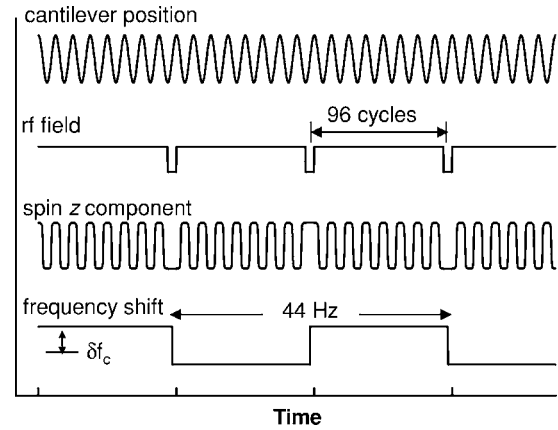

FIG. 2. Timing diagram for conventional iOSCAR protocol. As the cantilever oscillates, the z component of spin is modulated in response to the cantilever motion, except when the rf field is interrupted. These interruptions last for precisely one-half an oscillation period and occur every 96 cantilever cycles, leading to a modulation in the cantilever frequency.

met, the spins will be locked (or antilocked) to the effective field, and will thereby be synchronously inverted with each cantilever oscillation.[23] The backaction force of the spins on the cantilever gives rise to a slight cantilever frequency shift δf_c, whose sign depends on whether the spins are locked or antilocked to the effective field.

Rather than measure a dc frequency shift, we impose a modulation on the signal using an "interrupted" version of the protocol referred to as iOSCAR. As shown in Fig. 2, we turn off the rf power for one-half of a cantilever cycle every 96 cycles, which skips one adiabatic reversal, which, in turn, results in a change in the sign of the frequency shift δf_c. This imposes a modulation on the frequency shift at one-half the rf interrupt frequency, giving the signal a very distinctive signature. The frequency shift signal is analyzed using either a Fourier power spectrum or lock-in detector implemented in software. For statistical polarization, the mean lock-in signal is zero, so we detect the variance, or signal "energy." A zero-base line signal is constructed by subtracting the in-phase and quadrature variances. The optimal signal-to-noise ratio will be obtained when the lock-in time constant is properly matched to the spin-lock correlation time τ_m.[24] We use a bank of filters to obtain the signal as a function of measurement bandwidth, which is used to deduce τ_m.[9]

In the limit of $Gx_{pk} \gg B_1$, the cantilever frequency shift due to the spins is given by[25]

$$\delta f_c = (2f_c/\pi k x_{pk})m_{\text{eff}}G \tag{2a}$$

$$= (2f_c/\pi k x_{pk})F_s, \tag{2b}$$

where m_{eff} is the component of magnetic moment along the effective field, and $F_s \equiv m_{eff}G$ represents the peak force exerted by the spins on the cantilever. Equation (2a) can be used to extract the effective number of spins contributing to the signal. Alternatively, Eq. (2b) can be used to convert the signal to a net force, which is useful when comparing signals at different cantilever amplitudes x_{pk}, for example.
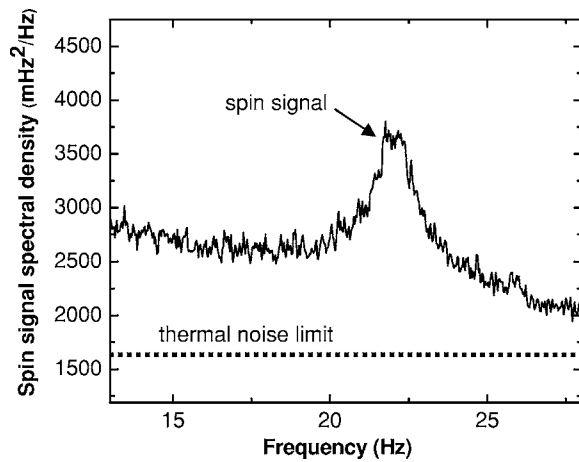
FIG. 3. Power spectral density of the frequency shift signal for the CaF_2 sample. An external field of 12 600 G was used to bring the sample into resonance, resulting in the statistical spin signal, seen as the peak at 22 Hz. The peak width of 1.9 Hz indicates a correlation time of roughly 170 ms. The estimated tip-sample separation was $\sim$150 nm. The thermal noise limit for our cantilever with Q=5000 is indicated by the dotted line. The background noise level is higher than this level because of sample-induced excess frequency noise, which has a $1/f$-like spectrum.

III. MEASUREMENTS OF NUCLEAR STATISTICAL POLARIZATION

The power spectral density of the iOSCAR signal for the CaF_2 sample is shown in Fig. 3. The rf field was turned off every 96 cantilever cycles ($f_{int}=f_c/96 \simeq 44$ Hz), resulting in a signal peak at 22 Hz. The spectral width of the peak is about 1.9 Hz, indicating a spin-lock correlation time τ_m of 0.17 s. This time is closely related to $T_{1\rho}$, the spin-lattice relaxation time in the rotating frame.[12,23] It can be affected by numerous parameters, such as the strength of the rf field, magnetic noise at the Rabi frequency due to higher order cantilever modes,[26,27] violation of the adiabatic condition, and the OSCAR protocol itself.[12,22] The latter two effects will be discussed later in the paper.

Scanning the external magnetic field B_{ext} moves the resonant slice relative to the tip, resulting in a signal when the slice penetrates into the sample. We plot the signal as a function of external field in Fig. 4(a), where the data represent the signal power from the lock-in detector in mHz^2. A zero base line signal is observed (within experimental error), with a large peak present in the range of $\sim$12 000–13 000 G, where the width of the peak is inhomogeneously broadened due to the field gradient from the tip. Assuming an estimated field gradient of 1 G/nm, the maximum signal power of 1100 mHz^2 corresponds to $m_{eff}=1.7\times10^{-19}$ emu, or of order 10 000 net nuclear spins. The noise level obtained with an averaging time of 2.5 h was $\sim$25 mHz^2, corresponding to roughly 2000 net nuclear spins. From Fig. 3, the integrated base line noise in the natural 1.9 Hz bandwidth was $\sim$5000 mHz^2, corresponding to roughly 30 000 net spins.

Since we are not measuring the Boltzmann polarization, there is no need to wait a longitudinal relaxation time T_1 between measurements. For our CaF_2 sample, the measured
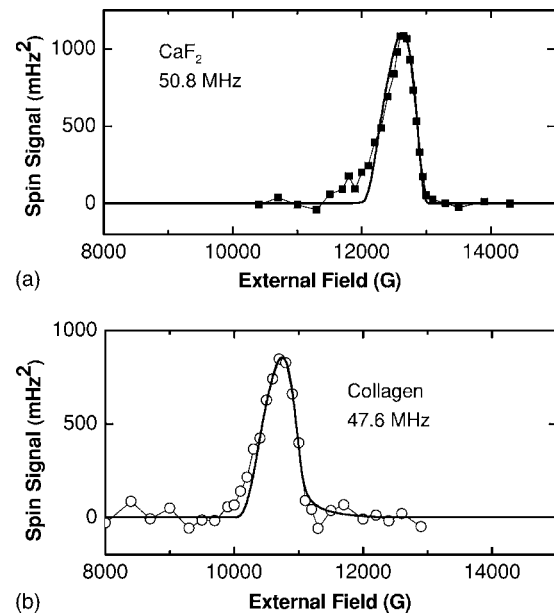

FIG. 4. MRFM signal vs externally applied magnetic field. (a) ^{19}F in CaF_2. The cantilever oscillation amplitude was 16 nm, and the applied rf frequency was 50.8 MHz, resulting in magnetic resonance when the total field is equal to 12 680 G. The continuous curve is calculated from a model based on a spherical tip with a diameter of 440 nm. In order to fit the model to the data, we had to assume a shift of +250 G in the field value at the location of the spins. This could be due to remanent magnetization in the body of our microscope, or a slight (2%) error in our field measurement. (b) Protons in collagen. The lower rf frequency, along with the higher gyromagnetic ratio for protons, result in a shift in the resonant field condition compared to ^{19}F.

T_1 was over 800 s at room temperature, and can be hours, days or longer in pure samples at low temperatures.[28,29] This consideration illustrates the significant advantage that can potentially be derived by working with the statistical polarization.

The MRFM signals from ^{1}H nuclei in PMMA and collagen were also readily detected. We plot the iOSCAR signal power as a function of B_{ext} for collagen in Fig. 4(b). The signal is seen in the range of $B_{ext} \sim$ 10 000–11 000 G. As expected, the field range is lower than in the case of the CaF_2, partly because of the 5% higher gyromagnetic ratio in compared to ^{19}F, and partly because the rf frequency was slightly lower. In addition, the exact shape and position of the peak will depend on the distance between the tip and sample, which may have been somewhat less in the collagen sample.

The τ_m correlation times extracted from the lock-in detector data were disappointingly short, with $\tau_m \sim$ 200 ms for CaF_2 and $\tau_m \sim$ 100 ms for collagen. In the case of PMMA, the correlation times were less than 50 ms, and it was not possible to make an accurate measurement. In comparison, values of τ_m up to several seconds have been measured for E' centers (electron spins).[9,12] The shorter times observed here may be at least partly due to issues with these particular materials: CaF_2 requires a large field B_1 to overcome the local fields,[30] for example, while in PMMA, it is known that
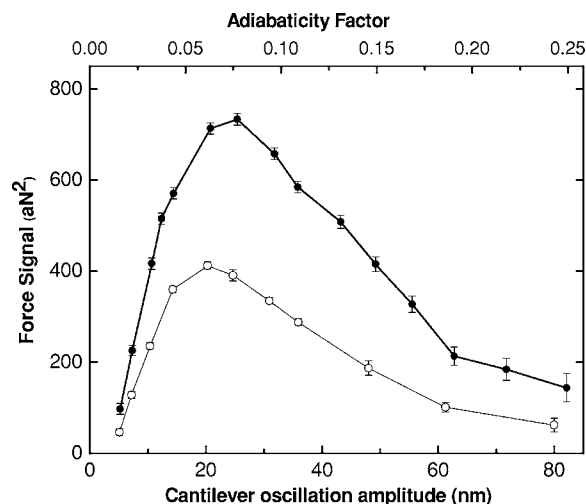
FIG. 5. Signal power vs cantilever oscillation amplitude for CaF$_2$. The open circles are for lower rf power ($B_1 = 15.5$ G) and the filled circles are for higher rf power ($B_1 = 18.1$ G). If the adiabatic reversals were equally effective under all conditions, the signal power would rise linearly from zero as a function of oscillation amplitude. In the case shown, the signal is diminished at the lowest amplitudes by the fact that the reversals are incomplete. At the higher amplitudes, the adiabatic condition is no longer met, which also reduces the signal.

tunneling of the methyl groups can occur over a wide frequency range and can affect the spin relaxation behavior.[31] At the same time, it is also likely that the iOSCAR protocol itself played a role.

For the iOSCAR protocol to work effectively, two conditions must be met. First, the field B_0 must be swept well off resonance; i.e., $Gx_{pk} \gg B_1$. As seen by Eq. (1), this ensures that the effective field, and thus the spins, are very nearly in the **z** direction when the cantilever reaches its extremum. Otherwise, each time the rf field is interrupted, the projected spin component along the effective field will be reduced. Second, the adiabatic condition $dB_0/dt \ll \gamma B_1^2$ must be satisfied.[23] A large value of x_{pk}, which drives the field B_0 farther off resonance, helps to satisfy the first condition. However, it hurts the second condition, since $dB_0/dt \propto x_{pk}$.

We observed that there was a fairly restricted range of cantilever oscillation amplitudes for which the iOSCAR protocol worked well. This is illustrated in Fig. 5, where the signal power vs oscillation amplitude x_{pk} is plotted for two different values of the rf field. For low oscillation amplitudes, the signal increased as x_{pk} was increased. This is partly because of the larger volume of spins being swept through by the resonant slice, but also because the field B_0 was being swept farther off resonance, leading to more complete adiabatic inversions. As x_{pk} was further increased, the signal reached a peak and then diminished, presumably due to violation of the adiabatic condition. We see that this decrease occurred for adiabaticity values, defined as $(dB_0/dt)/\gamma B_1^2$, greater than ~8%. With a larger value of B_1 (upper curve), the signal was greater, and the optimum value for x_{pk} was somewhat larger as well.

The conflicting requirements of iOSCAR and the adiabatic condition can be eased in at least two ways. First, the
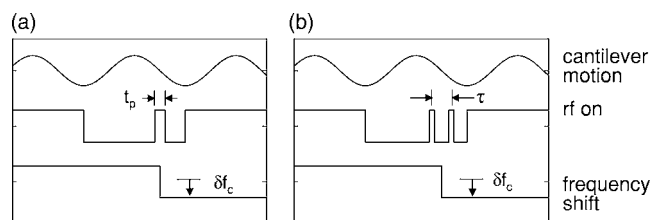

FIG. 6. Pulse sequences for use with modified iOSCAR that allow for manipulation of the statistical polarization. (a) Nutations. The rf field is interrupted for one full cantilever cycle every 96 cycles. Within the interruptions, the rf field is pulsed at the zero crossings. Those spins that are precisely on resonance will be begin to precess at the Rabi frequency about the effective field, which is in the x direction. Thus the z component will be a sinusoidal function of the pulse width T. (b) Transverse relaxation. Two $\pi/2$ pulses are inserted a time τ apart. For short τ, the effect is identical to a single π pulse. For long τ, the spins are left in a random direction in the x-z plane, and the spins are equally likely to be in the $+z$ and $-z$ directions when the field is turned back on.

condition $Gx_{pk} \gg B_1$ can be satisfied by reducing B_1 as the cantilever reaches its extremum. This type of rf pulse shaping was in fact performed in these measurements, and increased the signal by up to nearly a factor of 2. Second, decreasing the cantilever resonant frequency would allow for greater values of x_{pk} without violating the adiabatic limit. There may be lower practical limits on cantilever frequency, however, due to factors such as environmental vibrational noise.

IV. NUCLEAR SPIN MANIPULATION VIA MODIFIED iOSCAR

The above results verify that the protocols developed for detecting statistically polarized ensembles of electron spins are also applicable to nuclear spins. In addition to detection, the statistical polarization can also be manipulated into desired states through proper modification of the protocol. For example, we have previously demonstrated manipulation of the statistical polarization of electron spin ensembles using iOSCAR with extra rf interrupts in order to the rectify the spin fluctuations.[32]

In this section, we describe additional manipulation schemes that essentially compare the net polarization before and after a series of rf pulses. Because of its statistical nature, the initial state may be different each time the measurement is performed. Nevertheless, the pulses will affect the net polarization in some deterministic way that can be detected due to the finite correlation time of the polarization. The scheme is functionally very similar to a previously proposed scheme called CONQUEST (correlated observations narrow quantum uncertainty, enhancing spectroscopic transients), which is based on a second order correlation function of the signal before and after the pulse sequence.[14,15,33]

Our version of the detection protocol, illustrated in Fig. 6, is based on the iOSCAR protocol, with one key difference. The periodic interruptions in the rf field are now for one *full* cantilever cycle, rather than one half cycle. When the rf field is interrupted for one full cantilever cycle, a spin is left in
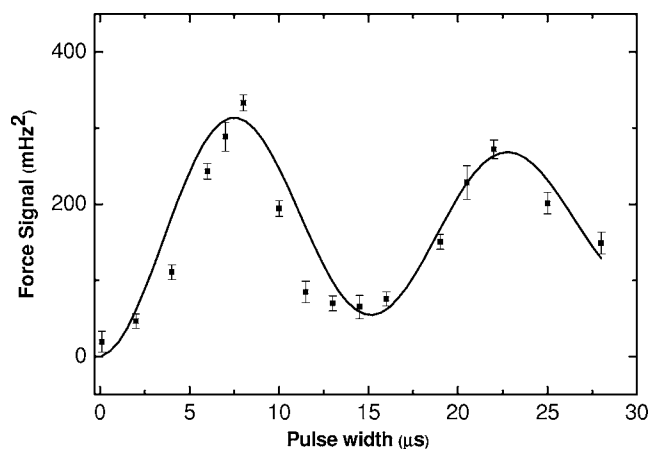
FIG. 7. Nutations of the statistical polarization in CaF_2. The modified iOSCAR signal is shown as a function of the pulse width t_p. The oscillatory nature of the signal is due to the precession of the spins about the effective field at the Rabi frequency. The period of the oscillations indicates a field strength $B_1 = 17$ G.

FIG. 8. Modified iOSCAR signal versus pulse delay τ. An exponential decay to the baseline is observed, indicating a transverse relaxation time $T_2^* = 4$ μs.

exactly the same phase relative to the cantilever motion as when it started. Therefore no modulation of the frequency shift should occur. However, suppose that at every full-cycle rf interrupt, a rf pulse is inserted precisely on resonance, as shown in Fig. 6(a). The spins will nutate around the effective field, which in this case is in the **x** direction. If the pulse width t_p corresponds to a π pulse, the spins will end up inverted, and the situation will be equivalent to normal iOSCAR: A modulated frequency shift will be observed at half the interrupt frequency, which can be synchronously detected using a lockin amplifier. If the pulse width is 2π, then spins are left noninverted, and the modulation should again disappear. Thus the signal should show oscillatory behavior, with a period given by $2\pi/\gamma B_1$.

This protocol has allowed us to make our detection of nutations using a statistically polarized ensemble. The results for CaF_2 are shown in Fig. 7. For the case in which no nutation pulse is inserted during the rf interrupt ($t_p = 0$), the signal is nearly zero, as expected. With a pulse inserted, the signal shows clear oscillatory behavior as a function of pulse width, with a period of roughly 15 μs. The measurement of the period allows for an absolute determination of the rf field strength, in this case $B_1 = 17$ G.

There is a close connection between this detection scheme and the CONQUEST scheme, as suggested by the following argument: Consider a model for the synchronous lock-in detection in which the basic signal $\delta f_c(t)$ is multiplied by a square wave of period $2T$ and then averaged. The resulting output signal then is made up of terms of the form $\delta f_c(t) - \delta f_c(t+T)$. (Here we have assumed that the square wave has no dc component. We also ignore correlations for times $\gtrsim T$, so that we can break up the time record into individual records of length $2T$, each of which is equivalent.) In this model, the mean square signal is simply the time average of $[\delta f_c(t) - \delta f_c(t+T)]^2$, or $2\langle \delta f_c(t)^2 \rangle - 2\langle \delta f_c(t) \delta f_c(t+T) \rangle$, where $\langle \cdots \rangle$ denotes the time average. In normalized form, this is simply 1-A, where A is the same correlation function $\langle I_z(t) I_z(t+T) \rangle$ measured by
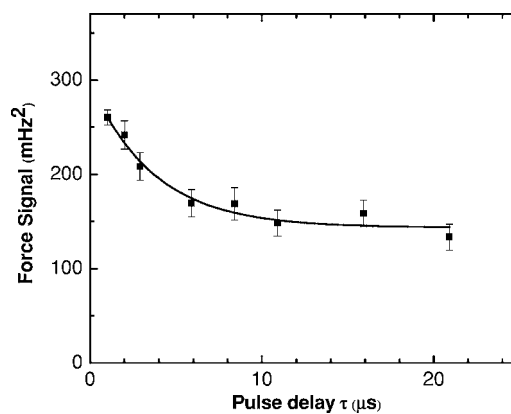
CONQUEST in its most straightforward version.[33] In either case, the technique relies upon the systematic effect on the signal (such as inversion) caused by the inserted pulses. This results in a time-averaged correlation function $\langle \delta f_c(t) \delta f_c(t+T) \rangle$ that has a nonzero value, even if the initial values of $\delta f_c(t)$ are completely random. Note that since the modified iOSCAR scheme imposes a modulation on the signal, it has the added benefit of reducing the influence of low frequency noise.

A slightly different pulse sequence, illustrated in Fig. 6(b), has been used to measure the inhomogeneous transverse relaxation time T_2^*. Two $\pi/2$ pulses are inserted with variable spacing τ between them. The signal as a function of τ for CaF_2 is shown in Fig. 8. As expected, the signal is a maximum for small τ. This situation is equivalent to inserting a single π pulse, causing the spin polarization after the pulse sequence to be anticorrelated to the signal before the sequence. As seen with the nutation pulses, the result is a maximum in the iOSCAR signal. For large τ, the polarization after the pulse sequence is completely uncorrelated to that before, due to transverse relaxation, and one should get a signal that is one-half the maximum signal. (Alternatively, for small τ, the final polarization is the negative of the initial polarization, so the difference is twice the initial polarization. For large τ, the final polarization has decayed to zero, so the difference is half the difference in the short τ case.) This behavior is seen in Fig. 8, with a maximum signal for short τ, and an exponential decay to a base line that is roughly half the initial value. From the exponential decay, we find that that the transverse relaxation time $T_2^* = 4$ μs. This short time is a reflection of the highly inhomogeneous field from the tip, which leads to a loss of phase coherence of the spins in physically different locations.

V. CONCLUSIONS

In summary, we have successfully applied the protocols developed for MRFM of electron spins to the case of nuclear spins. By performing iOSCAR to detect the statistical polarization in ensembles of nuclear spins, we have demonstrated

detection with sensitivity on the order of 2000 net nuclear spins in our 2.5 h averaging window. The statistical detection avoids the problem of the long T_1 times that exists for many nuclear spin systems at low temperatures. We have applied the technique to the system CaF_2, and have demonstrated our use of MRFM on a biomolecule. We have also demonstrated the ability to manipulate the naturally occurring statistical polarization in order to make nonequilibrium measurements, such as relaxation times and nutation measurements. Given a roughly $1000\times$ improvement in signal-to-noise ratio, which remains a considerable challenge, these techniques should in principle be extendible to individual nuclear spins.

[1] J. A. Sidles, Phys. Rev. Lett. **68**, 1124 (1992).

[2] J. A. Sidles, J. L. Garbini, K. J. Bruland, D. Rugar, O. Zueger, S. Hoen, and C. S. Yannoni, Rev. Mod. Phys. **67**, 249 (1995).

[3] D. Rugar, O. Zuger, S. Hoen, C. S. Yannoni, H. M. Vieth, and R. D. Kendrick, Science **264**, 1560 (1994).

[4] Z. Zhang, P. C. Hammel, and P. E. Wigen, Appl. Phys. Lett. **68**, 2005 (1996).

[5] K. R. Thurber, L. E. Harrell, R. Fainchtein, and D. D. Smith, Appl. Phys. Lett. **80**, 1794 (2002).

[6] S. R. Garner, S. Kuehn, J. M. Dawlaty, N. E. Jenkins, and J. A. Marohn, Appl. Phys. Lett. **84**, 5091 (2004).

[7] D. P. DiVincenzo, Phys. Rev. A **51**, 1015 (1995).

[8] G. P. Berman, G. D. Doolen, P. C. Hammel, and V. I. Tsifrinovich, Phys. Rev. B **61**, 14694 (2000).

[9] D. Rugar, R. Budakian, H. J. Mamin, and B. W. Chui, Nature (London) **430**, 329 (2004).

[10] F. Bloch, Phys. Rev. **70**, 460 (1946).

[11] T. Sleator, E. L. Hahn, C. Hilbert, and J. Clarke, Phys. Rev. Lett. **55**, 1742 (1985).

[12] H. J. Mamin, R. Budakian, B. W. Chui, and D. Rugar, Phys. Rev. Lett. **91**, 207604 (2003).

[13] S. A. Crooker, D. G. Rickel, A. V. Balatsky, and D. L. Smith, Nature (London) **431**, 49 (2004).

[14] P. L. Carlson, L. Madsen, G. M. Leskowitz, and D. Weitekamp, Bull. Am. Phys. Soc. **44**, 541 (1999).

[15] P. L. Carlson, L. A. Madsen, G. M. Leskowitz, and D. P. Weitekamp, U.S. Patent Nos. 6,078,082 and 6,081,119 (2000).

[16] Corning (formerly Optovac), North Brookfield MA.

[17] J. H. Choi, U. M. Mirsaidov, C. W. Miller, Y. J. Lee, S. Guchhait, M. D. Chabot, W. Lu, and J. T. Markert, Proc. SPIE **5389**, 399 (2004).

[18] B. W. Chui, Y. Hishinuma, R. Budakian, H. J. Mamin, T. W. Kenny, and D. Rugar, *Technical Digest of the 12th International Conference on Solid-State Sensors and Actuators (Transducers'03)*, (IEEE, Boston, MA, 2003), p. 1120.

[19] B. C. Stipe, H. J. Mamin, T. D. Stowe, T. W. Kenny, and D. Rugar, Phys. Rev. Lett. **86**, 2874 (2001).

[20] T. N. Ng., N. E. Jenkins, and J. A. Marohn (private communication).

[21] J. A. Marohn, R. Fainchtein, and D. D. Smith, Appl. Phys. Lett. **73**, 3778 (1998).

[22] B. C. Stipe, H. J. Mamin, C. S. Yannoni, T. D. Stowe, T. W. Kenny, and D. Rugar, Phys. Rev. Lett. **87**, 277602 (2001).

[23] C. P. Slichter, *Principles of Magnetic Resonance* (Springer, Heidelberg, 1996).

[24] M. Ting, A. O. Hero, D. Rugar, C.-Y. Yip, J. A. Fessler, preprint at http://xxx.lanl.gov/abs/quant-ph/0312139 (2003).

[25] G. P. Berman, D. I. Kamenev, and V. I. Tsifrinovich, Phys. Rev. A **66**, 023405 (2002).

[26] D. Mozyrsky, I. Martin, D. Pelekhov, and P. C. Hammel, Appl. Phys. Lett. **82**, 1278 (2003).

[27] G. P. Berman, V. N. Gorshkov, D. Rugar, and V. I. Tsifrinovich, Phys. Rev. B **68**, 094402 (2003).

[28] B. T. Beal and J. Hatton, Phys. Lett. **15**, 210 (1965).

[29] P. L. Kuhns, P. C. Hammel, O. Gonen, and J. S. Waugh, Phys. Rev. B **35**, 4591 (1987).

[30] K. Wago, O. Zuger, R. D. Kendrick, C. S. Yannoni, and D. Rugar, J. Vac. Sci. Technol. B **14**, 1197 (1996).

[31] A. J. Horsewill, Prog. Nucl. Magn. Reson. Spectrosc. **35**, 359 (1999).

[32] R. Budakian, H. J. Mamin, B. W. Chui, and D. Rugar (unpublished).

[33] L. A. Madsen, Ph.D. thesis, Caltech, 2002.